LIQUID PLUG DYNAMICS IN PULMONARY AIRWAYS

by

Ying Zheng

A dissertation submitted in partial fulfillment
of the requirements for the degree of
Doctor of philosophy
(Biomedical Engineering)
in The University of Michigan
2008

Doctoral Committee:

Professor James B. Grotberg, Chair
Associate Professor Shuichi Takayama
Associate Professor Joseph L. Bull
Research Assistant Professor Keith E. Cook

To my Mom, Dad, Sister
and my dear husband, Xiaodong

ACKNOWLEDGEMENTS

First of all, I would like to thank James B. Grotberg, my advisor, for his guidance and support during my Ph.D. study in The University of Michigan. I thank him being a knowledgeable advisor, who guided me to the world of biofluid dynamics; an encouragable father, who helped to build up my confidence in both research and life; and a conscientious researcher, who influenced me significantly with his enthusiasm on the research and a great sense of humor. I learned a lot from him and his guidance motivated me to be an independent thinker and researcher. It is one of my greatest assets to be a student in his lab and this experience will benefit me for the rest of my life.

Specially, I would like to thank Dr. Fujioka, who was very influential on my Ph.D. researches. I was really touched and encouraged by his devotion and enthusiasm to the research of biofluid mechanics. He is very knowledgeable and has always been there to help me when I had hardships in the research. He has been like a mentor and a big brother to me. My research cannot go so smoothly without him.

I would also like to thank Dr. Takayama for leading me to the microfluidic world and teaching me to view things from different perspectives and to think broadly and innovatively. Also, the Shu lab is full of brilliant and nice people and they have been extremely helpful. I would especially like to thank Yusuke, “Dan” Dongeun Huh, Yi-Chung Tung, “Albert” Bor-han Chueh, Yoko, Amy, Geeta, Jon, Nobu for their help and suggestions.

I would like to thank Dr. Bull and all the people in biotransport lab; Dr. Bull inspired me greatly with his kindness and guidance and he is very helpful in my research, coursework and life with his broad knowledge, modest and generous personality. I am also very grateful to Dr. Cook, who helped me better understand the application of engineering on medicine and inspired me to think from a different point of view and find motivations before doing any research.

I am very lucky to work with smart and friendly people in biofluids lab, and grateful for all the help and support from them. I want to thank Vinod Suresh for his assistance in revising my first paper in Chapter 3. I thank Joseph Anderson for his kindness to help me start my research when I joined this group. I thank David Halpern for his suggestions and insights in fluid mechanics. I am also thankful for the company and help from Kit Yan Chan, H.H. Wei, and Shiyao Bian. I would like to thank the people in biotransport lab, especially Yu-Chun Lin, Andres Calderon and Zhengzheng Wong for their friendship and helpful discussions. My graduate studies have been brightened and exciting with their company.

I would like to thank my parents and my sister who love and support me oversea. They taught me to be dedicated and responsible and inspired me to be the person that I am now. In their own way, they taught me to be persistent and warm-hearted. I know you are always there for me no matter what happens. I owe a great deal to you and I love you.

Lastly I would like to thank Xiaodong Xu, my husband. He is the reason that I came to Michigan and he is the biggest motivator for my years in Michigan. His optimistic attitude always inspires me and he always believes in me. He makes my life meaningful and exciting.

PREFACE

The second and third chapters of this dissertation are mostly based on the following publications;

1. Zheng, Y., Fujioka H., Grotberg, J.B., 2007, “Effects of gravity, inertia and surfactant on steady plug propagation in a two-dimensional channel”, Physics of Fluids 19 (8), 082107.
2. Zheng, Y., Fujioka H., Grotberg, J.C., Grotberg J.B., 2006, “Effects of inertia and gravity on liquid plug splitting at a bifurcation”, Transactions of The ASME, Journal of Biomechanical Engineering, 128 (5), pp707-716.
3. Zheng, Y., Anderson, J.C., Suresh V., Grotberg J.B., 2005, “Effect of gravity on liquid plug transport through and airway bifurcation model”, Transactions of The ASME, Journal of Biomechanical Engineering, 127 (5), pp798-806.

The forth, and fifth chapters of this dissertation will be submitted as separated papers with some modifications.

TABLE OF CONTENTS

LIST OF FIGURES

CHAPTER 1

CHAPTER 2

CHAPTER 3

CHAPTER 4

CHAPTER 5

LIST OF TABLES

CHAPTER 3

CHAPTER 4

ABSTRACT

LIQUID PLUG DYNAMICS IN PULMONARY AIRWAYS

by

Ying Zheng

Chair: James B. Grotberg

This dissertation investigates liquid plug transport through the pulmonary airways. It includes three aspects: liquid delivery into the lungs, mucus clearance from the lungs, and plug dynamics in flexible small airways.

Liquid plugs form in pulmonary airways during the process of liquid instillation in many clinical treatments. Studies have shown that treatment efficiencies may depend on how liquids distribute in the lung. Better understanding the fundamentals of liquid plug transport will reveal important system parameters governing the liquid distribution and facilitate treatment strategies. The plug propagation before reaching a bifurcation is studied computationally with the effects of gravity, plug speed and surfactant. Then the plug splitting through a symmetric bifurcation is studied experimentally and theoretically with different gravitational orientations, plug speeds, and downstream plug blockages. The liquid distribution is shown to be more homogeneous at larger volume, faster speed and lower gravitational effects.

In diseases such as asthma and pulmonary emphysema, thickening of the liquid lining and lack of surfactant may cause mucus plugs to form and block the breathing pathway. Removing mucus from the lung is very essential to reduce threaten on patients' life. Mucus plug propagation is studied computationally with various plug speed and

different shear thinning properties. Larger pressure is found to be required to drive the mucus plug at larger plug speed and in greater shear thinning effect. The surfactant effect is then investigated and found helpful on the mucus removal.

The plug propagation is studied in a microfluidic flexible channel experimentally, as a small airway model. Wall deformation is observed from the high negative pressure when plug propagates. The maximum wall deformation is found to increase with plug speed and plug length. Computations agree with the experiments and predict the higher stress and stress gradients on the flexible wall than the rigid one, which increase the potential risk on the cell damages.

The results presented in this dissertation provide new insights into the physical mechanisms on liquid plug dynamics in pulmonary airways during liquid instillation and removal. Further investigation in both experiments and computations can be used to mimic the specific in-vivo situations.

CHAPTER 1

INTRODUCTION

1.1 Lung Physiology

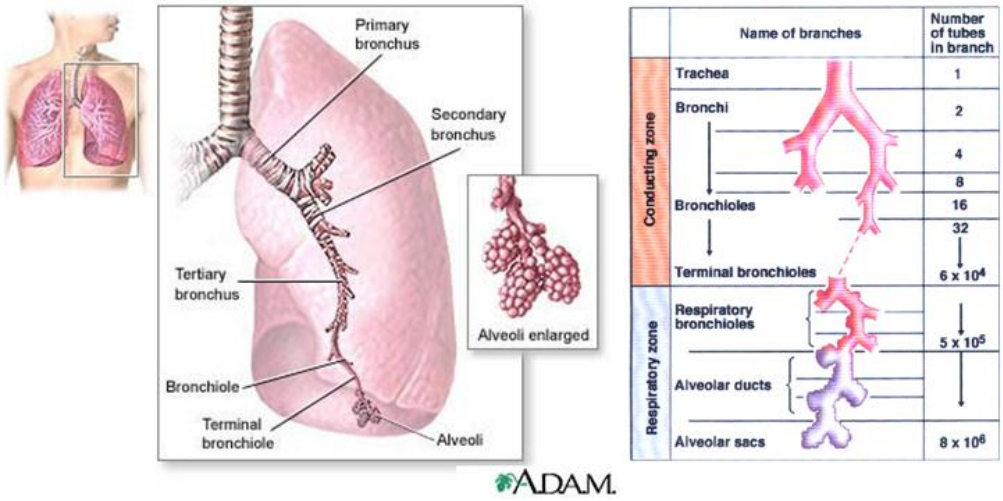

Figure 1.1 The lung anatomy and the generations of airway bifurcation trees[1].

The lungs, as portions of respiratory systems, are an organ for gas exchange. Oxygen is inhaled and carbon dioxide is exhaled. The air flow through the lungs is a pressure-driven cyclic flow during inspiration and expiration. As the air is inspired from the nose or mouth, it enters trachea, flows into the bronchi, and further down to the distal airways. There are more than 20 generations of branching in the lungs, each resulting in narrower, shorter and more tubes, as shown in Fig. 1.1. This extensive branching from the trachea resembles an inverted tree and is commonly called as bronchial tree. The trachea and bronchi contains cartilage on the walls while the walls no longer contain cartilage but smooth muscles from bronchioles to the terminals ones. From trachea to the terminal bronchioles are called conducting zone, which is to conduct the gas flow with low work. Alveoli start to appear in respiratory bronchioles and the number of alveoli increases as it goes further down to the lungs. The end section of airways is grapelike

clusters, entirely of alveoli. From the respiratory bronchioles to the end alveolar sacs are called respiratory zone, which is the region gas exchange occurs with the blood vessels surrounding the alveoli clusters.

The airway wall is flexible and attached to elastic connective tissues. The airway surfaces contain cilia that constantly beat toward the pharynx from the end of the respiratory bronchioles. Glands and epithelial cells along the airway walls secrete mucus. Mucus, which contains dust from inspired air, is then moved by ciliary activity to pharynx and then swallowed. The airway epithelium also secretes a watery fluid upon which the mucus can ride freely. The liquid lining in the lung is a protective coating, which prevents the tissue drying and is the first defense against the inhaled pathogens. Typically, from the trachea to terminal bronchioles, the liquid coating thickness is on the order of 5-10 microns; while in the small airways, the liquid lining is approximately 2-4% of the airway radius [2, 3].

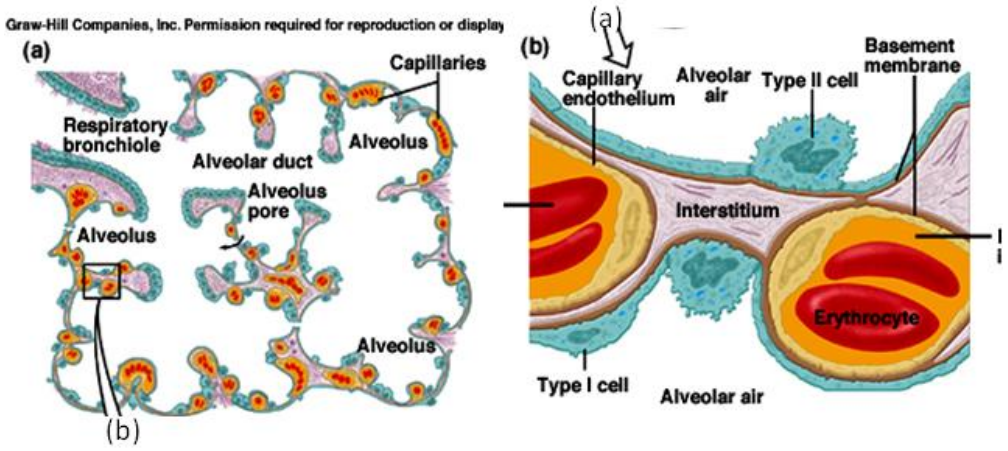

Figure 1.2 The respiratory zone and alveoli sacs [1].

The alveoli are balloon-like sacs with very thin walls, which consist of two types of alveolar epithelial cells along air-facing surfaces. One is continuous lining layer of thick and flat epithelial cells called type I alveolar cells. Interspersed between types I cells are thicker specialized cells called types II alveolar cells. Associated with the alveolar wall are alveolar macrophages, which is to remove debris in the alveolar spaces. The alveolar walls also contain capillaries and a very small interstitial space as shown in Fig. 1.2. Type I cells are the main sites of gas exchange and they control the fluid balance across the alveoli walls. Type II cells are rounded epithelial cells, which secrete alveolar

fluid to keep the alveoli surfaces and air moist. Included in alveolar fluid is surfactant, a detergent-like mixture of phospholipids and lipoproteins. It forms a monomolecular layer between the air and water at alveolar surfaces. The existence of surfactant markedly reduces the surface tension of alveolar fluid, which reduces the tendency of alveoli to collapse. Underlying the layer of type I alveolar cells is an elastic basement membrane, which support the alveoli structures.

1.2 Lung Pathophysiology

When surfactant is not sufficiently secreted, high surface tension is developed in the air-liquid interfaces in the lungs, which increases breathing difficulty and decreases the lung compliance. A striking example is known as respiratory distress syndrome (RDS) of the newborn, which is the second leading cause of death in premature infants. The type II alveolar cells may be too immature to secrete surfactant adequately. The infants have to inspire by the most strenuous efforts because of low lung compliance, which ultimately cause lung collapse and death. Adults can also develop RDS during respiratory failure. In these cases, therapy is assisted with a mechanical ventilator for breathing and the administration of natural or synthetic surfactant delivered via the adults' trachea [4-8].

Airway resistance is one important character of the lung physiology during the inspiration and expiration. For normal lungs, the airway resistance due to the air flow is very small. The airway radii are one important factor on the resistance since the resistance is inversely proportional to the fourth power of the airway radii. Another physical factor may be the stiffness of elastic connective tissue fibers that link the outside of the airways. The lungs may also develop abnormally large airway resistance due to the collapsing small airway. This may due to two reasons: lack of surfactant or airway wall collapse from wall elasticity and flexibility. Asthma and Chronic Obstructive Pulmonary Disease (COPD) are example diseases. Asthma is characterized by intermittent attacks in which airway smooth muscle contracts strongly to increase the resistance with chronic inflammation and excessive mucus secretion into the airway ducts [9]. COPD refers to emphysema or / and chronic bronchitis. The destruction and collapse of the small airways or alveoli are the major cause of emphysema, while chronic bronchitis is characterized by excessive mucus production in bronchi and thickening of the inflamed airways [10, 11].

In the United States lung cancer is the leading cause of cancer death in males and females, about 85% of which roughly are related to smoking [12]. Smoking may decreases respiratory efficiency by constricting the terminal bronchioles, reducing oxygen-binding capability, increasing mucus secretion, inhibiting the ciliary activities, and destroying the elastic fibers in the lung [13]. These changes cause collapse of small bronchioles and air trapping in alveoli sacs thus less efficient gas exchange.

1.3. Current Research

Liquid delivery

Liquid is delivered into the lungs in many clinical therapies. For example, surfactant instillation into the lung has been a standard treatment, known as Surfactant Replacement Therapy (SRT) [4-8], for premature neonates with Respiratory Distress Symptoms (RDS) due to undeveloped lungs and a deficiency of natural surfactant; or adults with acute RDS from lung injures which occurs with sepsis [14], smoke inhalation [15], multiple trauma, severe pneumonia, and near drowning. Perfluorcarbon, which has low surface tension and high O2/CO2 solubility, can be instilled into the lung during partial / total liquid ventilation [16-20] for treating RDS either in place of or in conjunction with SRT. Liquid bolus with drugs, genes or stem cells [21-24] can be instilled onto the airway epithelial cells in the lung with surfactant as transport vehicles to treat some genetic disease, such as cystic fibrosis. In addition, introduction of liquids into the lung or removal of liquids out of the lung also occurs in therapeutic or diagnostic bronchial alveolar lavage [25, 26]. Liquid delivery into the lung can be optimized depending on the specific applications, the efficiency of which may depend on where the liquid goes and how liquid distributes through the branching airway networks.

Many factors affect the liquid distribution, which makes the analysis complex: the liquid instillation method [27, 28], liquid propagation speed [29], gravity [30, 31], liquid properties , liquid volume [32], and presence of downstream plugs [27] from previous treatments in nearby airways, airway geometry, and interfacial activity [33, 34]. Previously, animal experiments have been performed on liquid distributions in the excised rat lungs for different instillation method, instillation rate and animal postures. Cassidy et al. [27] found that the initial plug formation in the trachea followed by an air inspiration cause more uniform distribution than those without a plug formation. Slow

administration through a catheter inserted in the endotracheal tube tended to be a trickling stream whose path is governed by gravity, leading to relatively inhomogeneous delivery. Faster injection promoted the liquid plug formation in the trachea or large airways that could be propelled distally by forced inspiration, introducing more homogeneous patterns. Anderson et al. [29] and Bull et al. [30] found that faster ventilation rate caused more homogenous liquid distribution in the animal lungs. Bull et al. suggested that the supine posture helped to develop more homogenous liquid distribution than the upright posture, in which liquid predominantly filled the inferior (gravitational favored) regions of the lungs.

Previous bench top experiments [35] have studied the plug splitting across a symmetric bifurcation isogravitationally. It was shown that the plug split evenly across the symmetric bifurcation model, while more liquid entered the unblocked daughter tube when a secondary liquid plug was introduced as a downstream blockage to simulate the effects of the previous treatments on the liquid distribution.

Theoretically, liquid/surfactant delivery to the lung has been studied to understand the physics behind the plug propagation/splitting. Halpern et al. [34] numerically studied liquid/surfactant delivery to the lung with considering four distinct transport regimes, which included the plug formation and transport in large or central pulmonary airways. They found that both transit and delivery time were strongly influenced by the strength of the preexisting surfactant and the geometric properties of the airway network. When the plug is long enough, the physical phenomena of the plug propagation is very similar to the propagation of semi-infinite bubbles. Several theoretical [36-38], experimental [39-41] and numerical [42-44] studies were performed to study the propagation of semi-infinite bubbles. However, when the plug was short, there was evidence [45] that the flow and transport might be affected by the interactions between two menisci, which is quite different with the semi-infinite bubble propagation. Previous studies in our group [45-48] numerically or theoretically investigated plug propagation in liquid-lined channels or tubes and the effects of speed, surfactant and their combination effects, without considering the effect of gravity. Effect of gravity has been examined through the Bond number, Bo, in finite-length bubbles [49], droplets [50] as well as the semi-infinite

bubble propagations both experimentally [51, 52] and theoretically [53, 54], and in static plugs [55].

Mucus clearance

The respiratory mucus has non-Newtonian properties. Mucus clearance were studied extensively in mucocilliary clearance (MCC) [56] and cough clearance [57, 58]. In diseases like asthma and emphysema, large amount of mucous plugs were observed in airways [9], which contribute to the morbidity and mortality. The removal of mucus plugs is then very essential to reduce the life threatens for asthmatic patients. However, no study has been found on the mechanisms of mucus plug clearance and how the surfactant acts on the mucus clearance. Functionally the surface active layer (surfactant layer) in the airways is responsible for maintenance of patency of airways [59]. Therefore, the surfactant therapy benefits the treatment of obstructive airway diseases like asthma and chronic bronchitis. Rubin et al. [60] described the efficacy of Exosurf (a therateutic non-protein surfactant) in decreasing the viscoelasticity of mucus in RDS. De Sanctis et al. [61] studied the effect of Curosurf (a natural surfactant from minced pig lungs) on mucus viscosity and mucociliary clearance in dogs suffering from RDS. The tracheal mucus velocity was found to increase significantly with surfactant but no changes were observed in viscoelastic parameters of mucus. The role of surfactants in alteration of viscosity of respiratory mucus was not well established.

Mucus flow in the respiratory airways is studied as two phase film flow by Clark et al. and Kim et al. [62, 63], and the role of surfactant in the mucus film flow was studied [64] using Hershel-Burkeley model, which includes the properties of shear-thinning properties and yield stress. The surfactant has shown to help increase the mucus flow velocities. However, the mucus plug propagation remains to be investigated and more insight needs to be shed into surfactant effect on mucus plugs.

Microfluidic Application and Cellular studies.

Pulmonary epithelial cells may be damaged by mechanical stresses associated with two-phase flow. Gaver's group [65-67] investigated the surface tension induced epithelial cell damage during airway reopening. They found cell damage increased with decreasing the re-opening velocity and concluded the pressure gradient near the finger tip of the semi-infinite bubbles was the most likely cause of the cell damage within the

different types of stresses. As plugs propagate along the airways, the capillary wave induced by the front interface of the plug may cause additional stress on the cell lining of the wall, i.e. more potentials on cell damage. Huh et al. [68]recently investigated the plug propagation and rupture on human small airway epithelial cells. They found cell damage increased with exposure frequency and decreasing plug length, especially when plug was near/during rupture. This indicated that the pressure and shear stress induced by the plug propagation and rupture may play an important role on the cell damage lining along the airway walls. All the above studies were performed in rigid channels. However, in reality, the airway walls are flexible. The plug propagation and resulting cell damages on flexible walls need to be examined to understand the in-vivo situations.

The effect of flexible channels/ tubes has been investigated theoretically on the plug formation [69] and propagation [47, 70] and semi-infinite bubbles [71-75] during airway reopening process. The channel wall has shown to deform during the bubble propagation or plug formations. Detailed flow pattern and wall stress changes due to the deformation of the flexible wall are still needed to reveal the causes of the cell injuries.

1.4. Motivation

Liquid plugs in the pulmonary airways can be formed in two different ways: extrinsically and intrinsically. Extrinsically, liquid plugs are instilled and transported through pulmonary airways in medical treatments and the delivery can be optimized in the specific applications. It is desirable to transport the liquid to the alveoli in some cases, while in others it is more effective to coat the liquid along the airway walls. It may also be important to spread the liquid homogenously or preferably to specific lobes or generations depending on the applications. In clinical studies, liquid instillation tends to be performed on the patients in different orientations with gravity to improve the response rate in the clinical treatments, For example, in SRT, though it has reduced infant mortality by half [76], the non response rate in some studies is still 15-35% depending on the patient group. This response rate may depend on the liquid distribution. Consider the delivery process of the liquid: the liquid starts as a liquid plug in the trachea, the plug propagates along the airways and splits across the airway bifurcations, and it deposits the film lining on the airway walls and finally reaches the alveoli compartments. The

effectiveness of these treatments may depend on where the liquid goes or how the liquid distributes through the branching airway networks.

Fig.1.3 shows a sample result of our experiments of liquid instillation in the rat lungs taken in collaboration with colleagues at the Medical College of Wisconsin. As different postures were chosen for the rat, i.e. supine and upright postures, the different distributions were achieved. With supine posture, the liquid tended to distribute uniformly into the rat lungs; while with upright posture, the liquid was prone to enter the gravity-dependent region as well as the side left lobe with shorter airway branches. These experiments indicate the mechanisms of plug propagations and splitting: how the gravity, liquid dose, instillation speed, and surfactant affect the plug propagation and distributions. It is well known that the pulmonary airway network has a three-dimensional nature [77-79], in which different airway branches have different dimensions and orientations. Thus the parameters such as the velocity, gravity effect and airway diameters vary in a wide range. Research is in need on the effects of gravity, inertia and presence of surfactant on steady plug propagation and transport, as well as the liquid plug splitting.

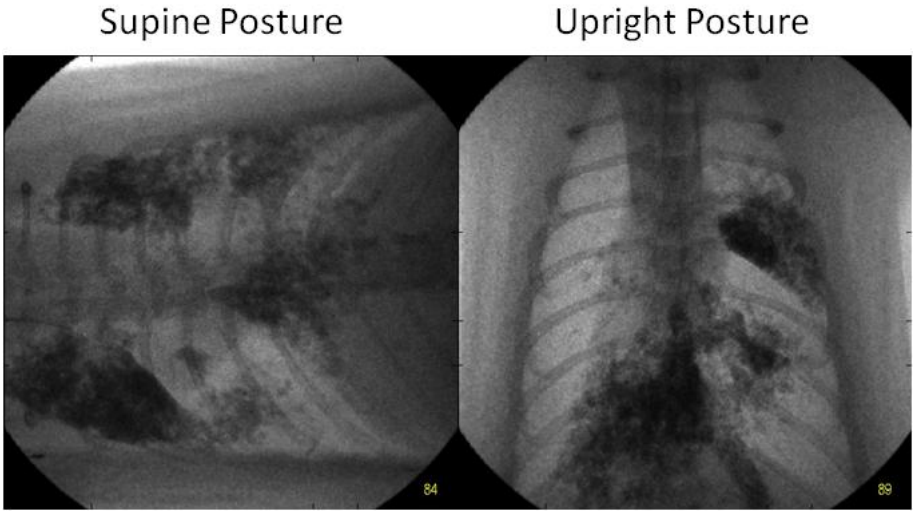

Figure 1.3 The liquid distribution of PFC in rat lungs with different postures after 20 breath numbers of the liquid instillation from the trachea.

Intrinsically, excessive mucus can be secreted into airways and mucus plug can form in some diseases like asthma [9] and emphysema [10, 11]. The air-liquid interfacial instabilities increase [80-82], mucous plugs may form and contribute to the airway obstruction, airway morbidity and mortality. Studies have reported that asthmatic patients

who died suddenly and unexpectedly showed occlusion of the lumen by mucous plugs [83-85]. These mucus plugs may be formed from the accumulated mucus film to occluding liquid bridges which fill the whole tube cross-section. Once the mucus plugs form, the airway closure occurs and airflow is blocked, which threaten the patients' lives. The mucus plugs need to be cleared from the airway to enhance gas exchange. This can be realized by forcing the mucus plug to propagate, and then either rupture downstream or be cleared out from the mouth. It is then beneficial to study the non-Newtonian behavior of the mucus during the mucus plug propagation as well as whether and how the surfactant improves the mucus removal.

Real lung airways are flexible, especially in small airways. It is well recognized that the liquid lining of the lung can close off a small airway, either by the formation of a meniscus (plug) or / and by provoking the sudden collapse of the flexible airway wall to a small cross section area [82, 86], especially during diseases like asthma and Chronic obstructive pulmonary disease (COPD). While several experiments [65-68] have been conducted to show the local tissue/cell damages due to the mechanical stresses during airway reopening, none considered effect of wall flexibility on the plug dynamics. Therefore, it is interesting to study how the wall flexibility affects the scenarios of the cell injury during the plug propagations.

In general, the fundamental fluid mechanics and transport behind the liquid plug propagation and splitting will help us to understand the lung physiology and pathophysiology, optimize the process of liquid delivery and mucus clearance thus achieve better treatment outcomes and reveal the potential lung injuries from high wall stresses by liquid plug propagations. It is also very beneficial to study the plug propagation on the flexible channels, which mimic the in-vivo situations of flexible lung and airways. The investigation of the plug dynamics is also very important for oil recovery and other multiphase flow applications.

1.5. Dissertation Overview

This dissertation aims to develop detailed models experimentally, theoretically and computationally for plug propagation and splitting with combined effects in the pulmonary airway, in order to understand the fundamental mechanisms in plug evolution, and provide guidance to the clinical treatments for the liquid delivery and mucus

clearance, and assess the potential cell damages in the presence of plugs in the real lung airways.

Chapter 2 and 3 are focused on the liquid delivery. Chapter 2 studies the steady liquid plug propagation at the stage of prebifurcation in the pulmonary airways with a two-dimensional channel model and numerically study the effects of gravity, inertia and surfactant. The local flow patterns are presented as well as liquid deposition in trailing films, pressure drop across the liquid plugs, volume ratio and the wall stresses with those individual effects. Chapter 3 investigates the liquid plug splitting across an airway bifurcation model. The splitting ratio is experimentally studied for various plug speed, at two different flow regimes, Stokes flow and finite Reynolds number flow with various gravitational effects, and theoretical models are used to compare with the experimental results.

Chapter 4 investigates the mucus clearance by characterizing the non-Newtonian steady plug propagation in a 2-D channel. The shear-thinning properties of the mucus are investigated based on the mucus viscosity, driven pressure drop, plug shear stress and wall stresses at various propagation speed. The effect of surfactant is studied on the mucus clearance as well.

Chapter 5 explores the microfluidic applications of the plug propagation in the flexible microchannels. Experiments were conducted on the plug propagation in microchannels with a flexible wall. The wall deformation is investigated from the plug propagations due to the high wall stresses on the flexible channel wall. Then numerical simulations are performed to compare with the experiments with the same channel design and geometry.

Chapter 6 summarizes the dissertation with major findings and conclusions.

References

1. Widmaier, E.P., H. Raff, and K.T. Strang, *Human physiology: the mechanisms of body function*. 10th ed. 2006, Boston: McGraw-Hill.
2. Codd, S.L., et al., *Tensile stiffness of ovine tracheal wall.* Journal of Applied Physiology, 1994. **76**(6): p. 2627-2635.
3. Yager, D., et al., *Airway surface liquid thickness as a function of lung volume in small airways of the guinea pig.* Journal of Applied Physiology, 1994. **77**(5): p. 2333-40.
4. Corbet, A., et al., *Decreased mortality rate among small premature infants treated at birth with a single dose of synthetic surfactant: a multicenter controlled trial.* Journal of Pediatrics, 1991. **118**(2): p. 277-284.
5. Jobe, A.H., *Pulmonary surfactant therapy.* New England Journal of Medicine, 1993. **328**(12): p. 861-868.
6. Long, W., et al., *A controlled trial of synthetic surfactant in infants weighing 1250 g or more with respiratory distress syndrome. The American Exosurf Neonatal Study Group I, and the Canadian Exosurf Neonatal Study Group.* New England Journal of Medicine, 1991. **325**(24): p. 1696-703.
7. Salvia-Roiges, M.D., et al., *Efficacy of three treatment schedules in severe meconium aspiration syndrome.* Acta Paediatrica, 2004. **93**(1): p. 60-65.
8. Yapicioglu, H., et al., *The use of surfactant in children with acute respiratory distress syndrome: efficacy in terms of oxygenation, ventilation and mortality.* Pulmonary Pharmacology & Therapeutics, 2003. **16**(6): p. 327-333.
9. Shimura, S., et al., *Continuity of airway goblet cells and intraluminal mucus in the airways of patients with bronchial asthma.* European Respiratory Journal, 1996. **9**(7): p. 1395-1401.
10. Matthay, M.A. and J.A. Clements, *Coagulation-dependent mechanisms and asthma.* Journal of Clinical Investigation, 2004. **114**(1): p. 20-23.
11. Mauad, T., et al., *Abnormal alveolar attachments with decreased elastic fiber content in distal lung in fatal asthma.* American Journal of Respiratory and Critical Care Medicine, 2004. **170**(8): p. 857-862.
12. Ries, L.A.G., et al., *SEER Cancer Statistics Review, 1975-2001*. National Cancer Institute, Bethesda, MD, 2004.
13. U.S. Department of Health and Human Services, *The Health Consequences of Smoking: A Report of the Surgeon General*, in 2004, US Department of Health and Human Services Center for Disease Control and Prevention National Center for Chronic Disease Prevention and Health Promotion Office on Smoking and Health: Rockville MD.
14. Nieman, G.F., et al., *Surfactant replacement in the treatment of sepsis-induced adult respiratory distress syndrome in pigs.* Critical Care Medicine, 1996. **24**(6): p. 1025-33.
15. Nieman, G.F., et al., *Comparison of exogenous surfactants in the treatment of wood smoke inhalation.* American Journal of Respiratory & Critical Care Medicine, 1995. **152**(2): p. 597-602.
16. Cox, P.N., et al., *Fluorocarbons facilitate lung recruitment.* Intensive Care Medicine, 2003. **29**(12): p. 2297-2302.

17. Hirschl, R.B., et al., *Partial liquid ventilation in adult patients with ARDS: a multicenter phase I-II trial. Adult PLV Study Group.* Annals of Surgery, 1998. **228**(5): p. 692-700.
18. Hirschl, R.B., et al., *Prospective, randomized, controlled pilot study of partial liquid ventilation in adult acute respiratory distress syndrome.* American Journal of Respiratory and Critical Care Medicine, 2002. **165**(6): p. 781-787.
19. Leach, C.L., et al., *Partial liquid ventilation with perflubron in premature infants with severe respiratory distress syndrome. The LiquiVent Study Group.* New England Journal of Medicine, 1996. **335**(11): p. 761-7.
20. Mikawa, K., et al., *Efficacy of partial liquid ventilation in improving acute lung injury induced by intratracheal acidified infant formula: Determination of optimal dose and positive end-expiratory pressure level.* Critical Care Medicine, 2004. **32**(1): p. 209-216.
21. Iqbal, S., et al., *Drug delivery and adherence in young children.* Pediatric Pulmonology, 2004. **37**(4): p. 311-317.
22. Myrdal, P.B., et al., *Optimized dose delivery of the peptide cyclosporine using hydrofluoroalkane-based metered dose inhalers.* Journal of Pharmaceutical Sciences, 2004. **93**(4): p. 1054-1061.
23. Yu, J. and Y.W. Chien, *Pulmonary drug delivery: physiologic and mechanistic aspects.* Critical Reviews in Therapeutic Drug Carrier Systems, 1997. **14**(4): p. 395-453.
24. Kharasch, V.S., et al., *Pulmonary surfactant as a vehicle for intratracheal delivery of Technetium Sulfur Colloid and Pentamidine in hamster lungs.* American Review of Respiratory Disease, 1991. **144**: p. 909-913.
25. Alberti, A., et al., *Bronchoalveolar lavage fluid composition in alveolar proteinosis - Early changes after therapeutic lavage.* American Journal of Respiratory and Critical Care Medicine, 1996. **154**(3): p. 817-820.
26. Moore, B.R. and J.H. Cox, *Diagnostic use of bronchoalveolar lavage in horses.* Equine Practice, 1996. **18**(5): p. 7-15.
27. Cassidy, K.J., et al., *A rat lung model of instilled liquid transport in the pulmonary airways.* Journal of Applied Physiology, 2001. **90**: p. 1955-1967.
28. Espinosa, F.F. and R.D. Kamm, *Meniscus formation during tracheal instillation of surfactant.* Journal of Applied Physiology, 1998. **85**(1): p. 266-72.
29. Anderson, J.C., et al., *Effect of ventilation rate on instilled surfactant distribution in the pulmonary airways of rats.* Journal of Applied Physiology, 2004. **97**(1): p. 45-56.
30. Bull, J.L., et al., *Distribution dynamics of perfluorocarbon delivery to the lungs: an intact rabbit model.* Journal of Applied Physiology, 2004. **96**(5): p. 1633-1642.
31. Ueda, T., et al., *Distribution of surfactant and ventilation in surfactant-treated preterm lambs.* Journal of Applied Physiology, 1994. **76**(1): p. 45-55.
32. Gilliard, N., et al., *Effect of volume and dose on the pulmonary distribution of exogenous surfactant administered to normal rabbits or to rabbits with oleic acid lung injury.* American Review of Respiratory Disease, 1990. **141**(3): p. 743-7.
33. Davis, J.M., et al., *Short-term distribution kinetics of intratracheally administered exogenous lung surfactant.* Pediatric Research, 1992. **31**(5): p. 445-50.

34. Halpern, D., O.E. Jensen, and J.B. Grotberg, *A theoretical study of surfactant and liquid delivery into the lung.* Journal of Applied Physiology, 1998. **85**(1): p. 333-352.
35. Cassidy, K.J., N. Gavriely, and J.B. Grotberg, *Liquid plug flow in straight and bifurcating tubes.* J. Biomech. Eng., 2001. **123**(6): p. 580-589.
36. Bretherton, F.P., *The motion of long bubbles in tubes.* Journal of Fluid Mechanics, 1961. **10**: p. 166-188.
37. Park, C.-W. and G.M. Homsy, *Two-phase displacement in hele shaw cells: theory.* Journal of Fluid Mechanics, 1984. **139**(291-308).
38. Ratulowski, J. and H.-C. Chang, *Transport of gas bubbles in capillaries.* Phys. Fluids A, 1989. **1**(10): p. 1642-1655.
39. Cox, B.G., *On driving a viscous fluid out of a tube.* Journal of Fluid Mechanics, 1962. **14**: p. 81-96.
40. Goldsmith, H.L. and S.G. Mason, *The flow of suspensions through tubes II. Single large bubbles.* Journal of Colloid Science, 1963. **18**: p. 237-261.
41. Schwartz, L.W., H.M. Princen, and A.D. Kiss, *On the motion of bubbles in capillary tubes.* Journal of Fluid Mechanics, 1986. **172**: p. 259-275.
42. Giavedoni, M.D. and F.A. Saita, *The axisymmetric and plane cases of a gas phase steadily displacing a Newtonian liquid - A simultaneous solution of the governing equations.* Physics of Fluids, 1997. **9**(8): p. 2420-2428.
43. Halpern, D. and D.P. Gaver, *Boundary-element analysis of the time-dependent motion of a semi-infinite bubble in a channel.* Journal of Computational Physics, 1994. **115**(2): p. 366-375.
44. Heil, M., *Finite Reynolds number effects in the Bretherton problem.* Physics of Fluids, 2001. **13**(9): p. 2517-2521.
45. Fujioka, H. and J.B. Grotberg, *Steady Propagation of a Liquid Plug In a 2-dimensional Channel.* J. Biomech. Eng. Transaction of ASME, 2004. **126**(5): p. 567-577.
46. Fujioka, H. and J.B. Grotberg, *The steady propagation of a surfactant-laden liquid plug in a two-dimensional channel.* Physics of Fluids, 2005. **17**(8): p. 082102.
47. Howell, P.D., S.L. Waters, and J.B. Grotberg, *The propagation of a liquid bolus along a liquid-lined flexible tube.* Journal of Fluid Mechanics, 2000. **406**: p. 309-335.
48. Waters, S.L. and J.B. Grotberg, *The propagation of a surfactant laden liquid plug in a capillary tube.* Physics of Fluids, 2002. **14**(2): p. 471-480.
49. DeBisschop, K.M., M.J. Miksis, and D.M. Eckmann, *Bubble rising in an inclined channel.* Physics of Fluids, 2002. **14**(1): p. 93-106.
50. Hodges, S.R. and O.E. Jensen, *Spreading and peeling dynamics in a model of cell adhesion.* Journal of Fluid Mechanics, 2002. **460**: p. 381-409.
51. Jensen, M.H., et al., *Effect of Gravity on the Saffman-Taylor Meniscus: Theory and Experiment.* Physical Review A, 1987. **35**(5): p. 2221-2227.
52. Zukoski, E.E., *Influence of viscosity surface tension and Inclination Angle on Motion of Long Bubbles in Closed Tubes.* Journal of Fluid Mechanics, 1966. **25**: p. 821 & part 4.

53. Ha-Ngoc, H. and J. Fabre, *A boundary element method for calculating the shape and velocity of two-dimensional long bubble in stagnant and flowing liquid.* Engineering Analysis with Boundary Elements, 2006. **30**(7): p. 539-552.
54. Hazel, A.L. and M. Heil, *The steady propagation of a semi-infinite bubble into a tube of elliptical or rectangular cross-section.* Journal of Fluid Mechanics, 2002. **470**: p. 91-114.
55. Suresh, V. and J.B. Grotberg, *The effect of gravity on liquid plug propagation in a two-dimensional channel.* Physics of Fluids, 2005. **17**(3).
56. Houtmeyers, E., et al., *Regulation of mucociliary clearance in hearlth and disease.* European Respiratory Journal, 1999. **13**(5): p. 1177-1188.
57. Kim, C.S., et al., *Criteria for mucus Transport in the airways by 2-phase gas-liquid flow mechanism.* Journal of Applied Physiology, 1986. **60**(3): p. 901-907.
58. King, M., G. Brock, and C. Lundell, *Clearance of mucus by simulated cough.* Journal of Applied Physiology, 1985. **58**: p. 1776-82.
59. Banerjee, R. and R.R. Puniyani, *Exogenous surfactant therapy and mucus rheology in chronic obstructive airway diseases.* Journal of Biomaterials Applications, 2000. **14**(3): p. 243-272.
60. Rubin, B.K., O. Ramirez, and M. King, *Mucus rheology and transport in neonatal respiratory-distress syndrome and the effect of surfactant therapy.* Chest, 1992. **101**(4): p. 1080-1085.
61. De Sanctis, G.T., et al., *Exogenous surfactant enhances mucociliary clearance in the anaesthetized dog.* European Respiratory Journal, 1994. **7**(9): p. 1616-21.
62. Clarke, S.W., J.G. Jones, and D.R. Oliver, *Resistance to two-phase gas-liquid flow in airways.* Journal of Applied Physiology, 1970. **29**(4): p. 464-71.
63. Kim, C.S., A.J. Iglesias, and M.A. Sackner, *Mucus clearance by two-phase gas-liquid flow mechanism: asymmetric periodic flow model.* Journal of Applied Physiology, 1987. **62**(3): p. 959-71.
64. Craster, R.V. and O.K. Matar, *Surfactant transport on mucus films.* Journal of Fluid Mechanics, 2000. **425**: p. 235-258.
65. Bilek, A.M., K.C. Dee, and D.P. Gaver, *Mechanisms of surface-tension-induced epithelial cell damage in a model of pulmonary airway reopening.* Journal of Applied Physiology, 2003. **94**(2): p. 770-783.
66. Jacob, A.M. and D.P. Gaver, *An investigation of the influence of cell topography on epithelial mechanical stresses during pulmonary airway reopening.* Physics of Fluids, 2005. **17**(3).
67. Kay, S.S., et al., *Pressure gradient, not exposure duration, determines the extent of epithelial cell damage in a model of pulmonary airway reopening.* Journal of Applied Physiology, 2004. **97**(1): p. 269-276.
68. Huh, D., et al., *Acoustically detectable cellular-level lung injury induced by fluid mechanical stresses in microfluidic airway systems.* Proceedings of the National Academy of Sciences of the United States of America, 2007. **104**(48): p. 18886-18891.
69. Halpern, D. and J.B. Grotberg, *Fluid-elastic instabilities of liquid-lined flexible tubes.* Journal of Fluid Mechanics, 1992. **244**: p. 615-632.
70. Grotberg, J.B. and O.E. Jensen, *Biolfuid mechanics in flexible tubes.* Annual Review of Fluid Mechanics, 2004. **36**: p. 121-147.

71. Gaver, D.P., et al., *The steady motion of a semi-infinite bubble through a flexible-walled channel.* Journal of Fluid Mechanics, 1996. **319**: p. 25-65.
72. Halpern, D. and J.B. Grotberg, *Surfactant effects on fluid-elastic instabilities of liquid-lined flexible tubes: a model of airway closure.* J. Biomech. Eng. Trans. ASME, 1993. **115**(3): p. 271-277.
73. Halpern, D., et al., *Unsteady bubble propagation in a flexible channel: predictions of a viscous stick-slip instability.* Journal of Fluid Mechanics, 2005. **528**: p. 53-86.
74. Jensen, O.E., *Instabilities of Flow in a Collapsed Tube.* Journal of Fluid Mechanics, 1990. **220**: p. 623-659.
75. Jensen, O.E., et al., *The steady propagation of a bubble in a flexible-walled channel: Asymptotic and computational models.* Physics of Fluids, 2002. **14**(2): p. 443-457.
76. Long, W., et al., *Effects of two rescue doses of a synthetic surfactant on mortality rate and survival without bronchopulmonary dysplasia in 700- to 1350-gram infants with respiratory distress syndrome. The American Exosurf Neonatal Study Group I.* J. Pediatr., 1991. **118**(4 (Pt 1)): p. 595-605.
77. Fleming, J.S., et al., *Description of Pulmonary Deposition of Radiolabeled Aerosol by Airway Generation Using a Conceptual 3-Dimensional Model of Lung Morphology.* Journal of Aerosol Medicine-Deposition Clearance and Effects in the Lung, 1995. **8**(3): p. 297-300.
78. Sauret, V., et al., *Study of the three-dimensional geometry of the central conducting airways in man using computed tomographic (CT) images.* Journal of Anatomy, 2002. **200**(2): p. 123-134.
79. Weibel, E.R., *Morphometry of the human lung*. 1963, New York: Academic Press. 151.
80. Hughes, J.M.B., D.Y. Rosenzweig, and P.B. Kivitz, *Site of airway closure in excised dog lungs: histologic demonstration.* Journal of Applied Physiology, 1970. **29**: p. 340-344.
81. Kamm, R.D. and R.C. Schroter, *Is airway closure caused by a thin liquid instability?* Respiration Physiology, 1989. **75**: p. 141-156.
82. Macklem, P.T., D.F. Proctor, and J.C. Hogg, *The stability of peripheral airways.* Respiration Physiology, 1970. **8**: p. 191-203.
83. Carroll, N., et al., *Airway structure and inflammatory cells in fatal attacks of asthma.* European Respiratory Journal, 1996. **9**(4): p. 709-715.
84. James, A.L., et al., *Time to death, airway wall inflammation and remodelling in fatal asthma.* European Respiratory Journal, 2005. **26**(3): p. 429-434.
85. Jensen, H.H., et al., *Potential misclassification of causes of death from COPD.* European Respiratory Journal, 2006. **28**(4): p. 781-785.
86. Greaves, I.A., J. Hildebrandt, and J. F.G. Hoppin, *Micromechanics of the lung*, in *Handbook of Physiology*. 1986, American Physiological Society: Bethesda, MD.

CHAPTER 2

LIQUID DELIVERY AND DISTRIBUTION: PRE-BIFURCATION – EFFECTS OF GRAVITY, INERTIA AND SURFACTANT ON LIQUID PLUG PROPAGATION IN A 2-D CHANNEL

2.1 Introduction

The lung airways can be blocked by the liquid plug formation and affect the gas exchanges and lung functions. Research has been studied on the process of airway closure and airway reopening [1-8], but is still in need after the plug forms and when it is propagating on the view of fundamental fluid mechanics. The combined effects of gravity, inertia and presence of surfactant are still unknown on steady plug propagation. The detailed flow patterns have not been investigated as well as the pressure fields, surfactant transport, plug asymmetry and the induced wall stresses by these combined effects.

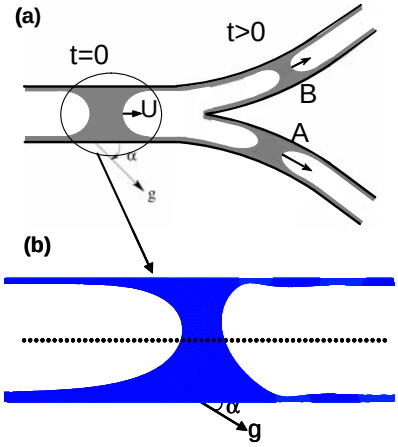

Figure 2.1 (a) An initial liquid plug instilled in the parent tube splits into two daughter tubes with pressure and gravity driven. (b) Pre-bifurcation asymmetry of liquid plug before reaching bifurcation with the gravity acting at an angle α to the flow direction

It is known that the lung is a 3-dimensional structure. Gravity may cause the plug to be asymmetric shaped so that different portions of liquid enters the daughter tubes after it passes a bifurcation and then reach different lung lobes. Prior to the plug splitting, it is

found that a large portion of plug volume resides below the centerline of parent airways due to the gravity (Fig.2.1b). This asymmetry may predetermine a large portion of plug to enter the lower branches (at t>0) as shown in Fig. 2.1a. The pre-bifurcation asymmetry is then important before the plug reaches the airway bifurcation for the overall liquid distribution. When surfactant is acting on the interface, the Marongoni stresses may have additional effects on the plug shapes and flow patterns.

Thus in this chapter, the steady plug propagation is numerically simulated in a two-dimensional channel lined by uniform, thin liquid films with gravity and the inspiration pressure as the driving forces. The aim is to investigate the combined effects of gravity, propagation speed, plug length, as well as the surfactant transport phenomena. A parameter $\lambda = \frac{\mathrm{Re}}{Ca} = \frac{\rho\sigma H^*}{\mu^2}$ exists, which is a constant determined by the channel geometry and fluid properties. The plug behavior is studied here in two regimes: the Stokes flow regime, i.e. Re=0; and finite Re regime, i.e. λ=1000. Section 2.2 describes the model and governing equations, Section 2.3 presents the grid generation and numerical method, Section 2.4 provides the results, Section 2.5 gives the discussion and finally Section 2.6 summarizes this chapter.

2.2 Problem Statement

2.2.1. Model Description

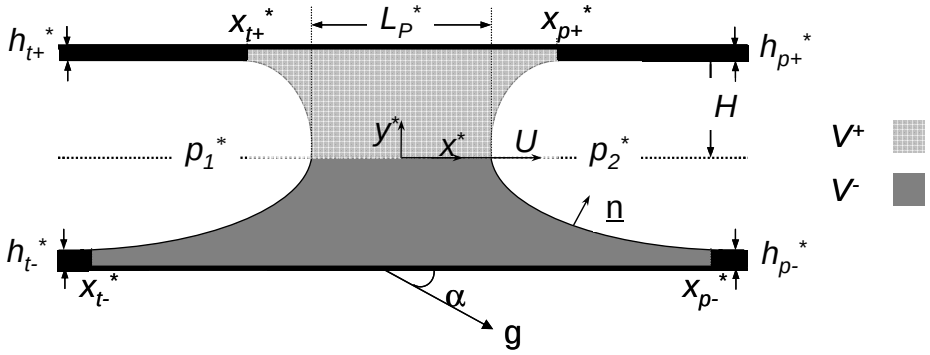

Figure 2.2 The schematic of the computational model for liquid plug propagation in a liquid-lined 2-D channel.

To simulate the plug transport in an airway branch, a computational model is developed on steady plug propagation in a 2-D channel with uniformly-coated liquid lining, the schematic diagram of which is shown in Fig. 2.2. The pressure drop, ΔP^* =

$P_1^* - P_2^*$, between the rear and front air phase, drives the motion of the liquid plug with a constant velocity U^* and plug length L_P^*, the length between two tips of the menisci. The liquid is composed of the incompressible and Newtonian fluid. H^* is the half channel width; h_{p+}^* and h_{p-}^* is the precursor film thickness while h_{t+}^* and h_{t-}^* is the trailing film thickness along the upper and lower wall respectively; α is the angle between the gravitational orientation to the x-axis; $\underline{n}$ is the unit normal vector on the interface. In our computational model, a moving frame is used on the plug with constant velocity U^*. The plug is assumed to be instilled into uniformly pre-coated lung airways, thus, $h_{p+}^* = h_{p-}^*$. At steady state, the mass leaving from the front is equal to that coming into the rear films. When the soluble surfactant is present, it can exist inside the plug bulk with concentration C^* or be absorbed on the interface with interfacial surfactant concentration Γ^*. The end precursor film in the front is assumed to have a constant surfactant concentration C_0^*. Equilibrium exists on the surfactant adsorption and desorption between the interface and the bulk. In the computation, the plug velocity U^* is specified and the pressure drop ΔP^* is the unknown to be solved.

2.2.2 Governing Equations

The steady flow inside the liquid plug is described by the dimensionless Navier-Stokes equation and the continuity equation as

$$\begin{gathered} \mathrm{Re}\ \underline{u}\cdot\underline{\nabla}\,\underline{u} = -\underline{\nabla}\,p + \nabla^2\underline{u} + \frac{Bo}{Ca}\,\underline{g} \\ \underline{\nabla}\cdot\underline{u} = 0 \end{gathered} \tag{2.1}$$

where $\underline{u} = (u, v)$ is the fluid velocity vector and the velocity components are scaled by U^*; the Cartesian coordinates (x, y) are scaled by H^*; p is the pressure scaled by the viscous force scale, $p = p^* \big/ \left(\mu U^* / H^*\right)$; the Reynolds number, $\mathrm{Re} = \rho U^* H^* / \mu$, represents the ratio of inertia to the viscous effect, in which ρ and μ are the fluid density and viscosity respectively; the capillary number, $Ca = \mu U^* / \sigma_M^*$, indicates the ratio of the viscous force to the surface tension (σ_M^* is the characteristic surface tension; for the constant surface tension cases, as shown in Section 2.4.1-4 and 2.4.6, σ_M^* is the constant surface tension at the interface; for Section 2.4.5 with surfactant condition, σ_M^* is the surface tension at surfactant-free condition, i.e. pure water condition); the Bond number,

$Bo = \rho g H^{*2} / \sigma_M^*$, represents the ratio of the gravity to the surface tension, where g is the gravity acceleration; and the gravitational unit vector, $\underline{g} = (\cos\alpha, -\sin\alpha)$.

When the surfactant is present, the surfactant transport is solved using the surfactant mass balance equation for the bulk concentration *C*:

$$Pe\ \underline{\nabla} \cdot (\underline{u}\, C) = \nabla^2 C \tag{2.2}$$

The surfactant transport along the interface can be solved using the following equation for the interfacial surfactant concentration Γ:

$$Pe_s \underline{\nabla}_s \cdot \left(\underline{u}_s \Gamma\right) = \nabla_s{}^2 \Gamma + J_n \tag{2.3}$$

where the bulk Peclet number, $Pe = U^* H^* / D^*$ and the interfacial Peclet number, $Pe_s = U^* H^* / D_s^*$, D^* and D_s^* are the diffusion coefficients of the surfactant in the plug bulk and along the interface respectively; $\underline{u}_s$ is the surface velocity. $\underline{\nabla}_s = (\underline{\underline{I}} - \underline{n}\,\underline{n}) \cdot \underline{\nabla}$. J_n is the kinetic flux of the surfactant from the bulk to the interface:

$$J_n = -\frac{1}{\beta} \frac{Pe}{Pe_s} \left[(\underline{n} \cdot \underline{\nabla}) C \right]_s \tag{2.4}$$

where $\beta = \Gamma_\infty^* / C_{cmc}^* H^*$ is the dimensionless adsorption depth, Γ_∞^* is the maximum equilibrium concentration of the interfacial surfactant. C_{cmc}^* is the critical micelle concentration in the bulk. Γ is scaled by Γ_∞^* and C is scaled by C_{cmc}^* in the transport equations.

To solve the surfactant transport equations, an equation of state is needed to relate the surface tension to the surface concentration of surfactant. For $\Gamma^* < \Gamma_\infty^*$, the surface tension σ^* vs. the interfacial concentration Γ^* is almost linear; while for $\Gamma_\infty^* \le \Gamma^* < \Gamma_{max}^*$, σ^*-Γ^* is nonlinear [9, 10], which is assumed to decay exponentially to a constant value at $\Gamma^* \to \Gamma_{max}^*$. Γ_{max}^* represent the dynamic maximum interfacial surfactant concentration. Thus, the dimensionless equation of state is approximated as

$$\sigma = \begin{cases} 1 - E\Gamma & (\Gamma < 1) \\ (1-E)\exp\left[\dfrac{E}{1-E}(1-\Gamma)\right] & (\Gamma \ge 1) \end{cases} \tag{2.5}$$

where E is the surface elasticity number $E = -\frac{\Gamma_\infty^*}{\sigma_M^*}\frac{\partial \sigma^*}{\partial \Gamma^*}\bigg|_{\Gamma^*<\Gamma_\infty^*}$ and indicates the ability of the surfactant to modify the surface tension.

To describe the transient period during which surfactant adsorbs from the bulk to the interface or desorbs from the surface monolayer to the bulk, linearized sorption kinetics will be used to determine the flux J_n [11, 12]. Both adsorption and desorption process will be involved when the interfacial surfactant concentration is smaller than the maximum equilibrium concentration ($\Gamma<1$) while only desorption is considered for $\Gamma\geq 1$. The equation is:

$$J_n = \begin{cases} K_a C_s (1-\Gamma) - K_d \Gamma & (\Gamma < 1) \\ -K_d \Gamma & (\Gamma \geq 1) \end{cases} \tag{2.6}$$

where $K_a = \frac{k_a^* C_{cmc}^* H^2}{D_s}$ represents the ratio of surfactant adsorption to surface diffusion, and $K_d = \frac{k_d^* H^2}{D_s}$ represents the ratio of the surfactant desorption to surface diffusion. k_a^* and k_d^* are the adsorption and desorption rate respectively. C_s is the dimensionless surfactant concentration on the sub-interface.

2.2.3 Boundary Conditions

A moving reference frame is chosen on the plug, thus, the no-slip and no penetration conditions at the wall are:

$$\underline{u} = (-1, 0), \quad \frac{\partial C}{\partial y} = 0 \text{ at } y = \pm 1 \tag{2.7}$$

For all the end films, the fully developed conditions are applied for the liquid velocity. At the precursor films, the bulk surfactant concentration is prescribed as $C=C_0$ and the pressure is equal to the front gas pressure ($P_2=0$) plus (minus) the hydrostatic pressure at the lower (upper) film, which is linear to the film height. At the trailing films, the axial gradient of the bulk surfactant concentration is zero, i.e. $\partial C/\partial x=0$; the film pressure is equal to the rear gas pressure P_1, as a part of solution, plus (minus) the hydrostatic pressure at the lower (upper) film. Assume that the plug is instilled into

uniformly pre-coated lung airways, thus, $h_{p+} = h_{p-}$, and at steady state, the mass leaving the front is the same as that coming into the rear: $\int_{p+} udy + \int_{p-} udy = \int_{t+} udy + \int_{t-} udy$, which is simplified as $h_{p+} + h_{p-} = h_{t+} + h_{t-}$ since $\underline{u} = (-1, 0)$, which is uniform in y at film regions.

At both air-liquid interfaces, the kinematic boundary conditions for the steady state are:

$$\underline{u} \cdot \underline{n} = 0 \tag{2.8}$$

A stress balance condition accounts for the stress jump due to the surface tension at the interface:

$$-p\,\underline{n} + (\underline{\nabla}\,\underline{u} + \underline{\nabla}\,\underline{u}^T) \cdot \underline{n} = Ca^{-1}(\kappa\sigma\,\underline{n} + \underline{\nabla}_s\sigma) - p_a\,\underline{n} \tag{2.9}$$

where p_a is the air pressure; $\kappa = \underline{\nabla} \cdot \underline{n}$ is the interface curvature; $\sigma = \sigma^* / \sigma_M{}^*$. The governing equations for the flow and transport will be solved using SIMPLER algorithm [13] with the boundary fitted coordinate transformation [14] as described in Section 2.3.

2.2.4 Parameter Estimation

The liquid plug propagation in the lung airways may depend on many parameters such as the breathing rate, gravity, tidal volume, airway geometry and liquid properties. For SRT, the typical properties of Survanta (Ross Laboratories, Columbus, OH) are ρ=0.94g/cm^3, μ=42cP, and $\sigma_M{}^*$ =25dynes/cm [15]. The airway reopening speed is estimated to be 0.5 ~ 30cm/s from generation 16 up to trachea in an adult human with breathing flow rate around 5L/min. Thus, for the airway generations 0 to 13 in an infant's lung or 7 to 16 in an adult, we have 0.1<Re<40, 0.1<Ca<2, 1<λ=Re/Ca<20, and 0.001<Bo<1. While for PLV, the typical values for perfluorocarbon liquid properties are ρ=1.93g/cm^3, μ=2.1cP, and $\sigma_M{}^*$=18 dynes/cm [15], which leads to the dimensionless parameters in the ranges of 10<Re<1000, 0.01<Ca<1, 10^3<λ<10^4, and 0.01<Bo<2.5. Thus Bo can be as high as O(1), which indicates that the gravity effect can be significant, and the range of Re shows that the effect of inertia may not be negligible.

When surfactant is present, it involves several dimensional and corresponding dimensionless parameters additionally. The surfactants are assumed to be soluble in this study. For typical pulmonary surfactants, the critical bulk concentration $C_{cmc}{}^*$ is 10^{-3}g/cm^3 [16], the maximum equilibrium surface concentration $\Gamma_\infty{}^*$ is 3.1x10^{-7}g/cm^2 [17] and the

elasticity number E is O(1) [10], which is assumed to be 0.7 in this study. In the infant airways the channel half width H^* is in the order of 10^{-1}cm, and the dimensionless adsorption depth $\beta \approx 10^{-2}$ though this β may not reflect true adsorption depth β_t, in which $\beta_t = \beta * \Gamma_{eq} / C_0$. The diffusivity of the typical pulmonary surfactant was found in the range of $10^{-7} < D_s^* < 7x10^{-5}$ cm^2/s at the interface [18] and $D^* \sim 5.4x10^{-8}$ cm^2/s in the bulk solution [19]. As the surfactant accumulates on the interface and its concentration Γ exceeds the maximum dynamic surfactant concentration Γ_{max}, the surfactant monolayer buckled and form micelles. The micelles detach from the interface and transport through the bulk as a particle without desorption. Due to the limitation of the present model, the simulation is only performed in the conditions that micelles are not created. Thus, to keep the bulk surfactant concentration smaller than the critical micelle concentration and the interfacial surfactant concentration smaller than the maximum surface concentration, larger surfactant diffusivities are imposed in both surface and the bulk and faster diffusion in the bulk than on the interfaces. Thus, the effect of soluble surfactant is investigated on steady plug propagation with Pe=500 in the bulk and Pe_s=5000 at the interface in Stokes flow regime, i.e. Re=0 with the presence of gravity.

2.3 Numerical Methods

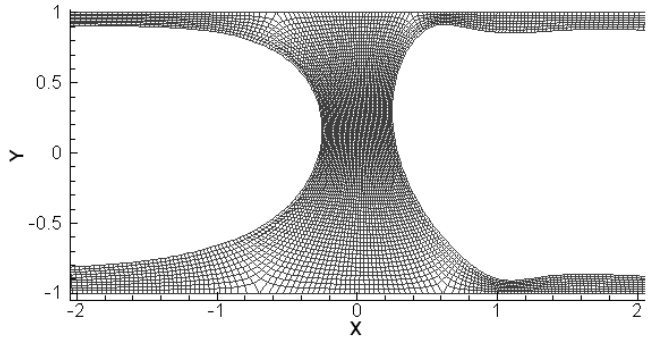

Figure 2.3 A sample computational grid around the plug core region for LP=0.5. The staggered grid is used. Pressure is stored at the center of the grid cells and the velocities are stored on the centers of the control surfaces.

The curvilinear computational grid was generated by solving the two-dimensional Poisson's equation [20] and the resulting grid lines are generated almost orthogonally. Fig. 2.3 shows a sample grid domain generated. A staggered grid is used for the variables where the scalar variables, p and C, are stored at the center of each control volume and

the velocity components are stored at the center of the control surfaces [21]. The physical domain (x,y) is mapped into the orthogonal computational domain (ξ,η) using the boundary fitted coordinate transformation [14]. In terms of the transformed variables, the governing equations are written as:

$$\frac{\partial}{\partial\xi}\left(\mathrm{Re}\,F^{\xi}\underline{u}-\frac{B_{11}}{J}\frac{\partial\underline{u}}{\partial\xi}\right)+\frac{\partial}{\partial\eta}\left(\mathrm{Re}\,F^{\eta}\underline{u}-\frac{B_{22}}{J}\frac{\partial\underline{u}}{\partial\eta}\right)$$
$$=-A^{T}\underline{\nabla}_{\xi}p+\frac{\partial}{\partial\xi}\left(\frac{B_{12}}{J}\frac{\partial\underline{u}}{\partial\eta}\right)+\frac{\partial}{\partial\eta}\left(\frac{B_{21}}{J}\frac{\partial\underline{u}}{\partial\xi}\right)+\frac{Bo}{Ca}\underline{g} \qquad (2.10)$$
$$\underline{\nabla}_{\xi}\cdot\underline{F}=0$$

where $\underline{\nabla}_{\xi}=\frac{\partial}{\partial\xi}\underline{e}_{\xi}+\frac{\partial}{\partial\eta}\underline{e}_{\eta}$, $\underline{\underline{A}}=\begin{bmatrix}\frac{\partial y}{\partial\eta} & -\frac{\partial x}{\partial\eta}\\ -\frac{\partial y}{\partial\xi} & \frac{\partial x}{\partial\xi}\end{bmatrix}$, $\underline{F}=\left(F^{\xi},F^{\eta}\right)=\underline{\underline{A}}\,\underline{u}$, $\underline{\underline{B}}=\underline{\underline{A}}\underline{\underline{A}}^{T}$. $\underline{\underline{A}}=A_{ij}$ is the transformation matrix and it represents the projected area of a control surface normal to the ith axis (ξ,η) onto jth plane (x,y). The control volume is the Jacobian of the transformation, $J=\left|\underline{\underline{A}}\right|$. The components of $\underline{F}$ are the mass flow rates through the control surface normal to the ξ and η axes, and are defined as the velocities in the computational domain. Terms including B_{ij} ($i=j$) are the primary diffusion terms, which represents the diffusive fluxes through control surfaces normal to the ξ (i=1) and η(i=2) axes. The secondary diffusion terms including B_{ij} ($i \neq j$), which are zero if the mesh lines are orthogonal; represent artifacts from the geometric transformation and are treated as sources term in the computational model.

When surfactant is present, the transformed equations for the surfactant transport along the interface and in the bulk. The interface in the computational domain corresponds to η grid lines and at the interface,

$$\frac{1}{\sqrt{B_{11}}}\frac{\partial}{\partial\eta}\left(Pe_{s}u_{s}\Gamma-\frac{1}{\sqrt{B_{11}}}\frac{\partial\Gamma}{\partial\eta}\right)=J_{n} \qquad (2.11)$$

in the bulk,

$$\frac{\partial}{\partial\xi}\left(PeF^{\xi}C-\frac{B_{11}}{J}\frac{\partial C}{\partial\xi}\right)+\frac{\partial}{\partial\eta}\left(PeF^{\xi}C-\frac{B_{22}}{J}\frac{\partial C}{\partial\eta}\right)=\frac{\partial}{\partial\xi}\left(\frac{B_{12}}{J}\frac{\partial C}{\partial\eta}\right)+\frac{\partial}{\partial\eta}\left(\frac{B_{12}}{J}\frac{\partial C}{\partial\xi}\right) \qquad (2.12)$$

The Semi-Implicit Method for Pressure-Linked Equation Revised (SIMPLER) [22] algorithm is employed to solve the momentum and mass conservation. Initially, an assumed velocity profile and interface shapes is used to start the computation, a sample grid of which is shown in Figure 2.3; The cubic splines [23] are applied to approximate the interface shapes as functions of their arc length; The new grid will be generated inside the plug domain after each iteration by solving Poisson's equation in successive over-relaxation method; The equation (2.10) is integrated over a control volume with the convective term written in a power-law hybrid differencing scheme [22], the mass fluxes and pressure are then solved iteratively using SIMPLER algorithm, which involves solving the momentum equation, the pressure equation, the pressure correction equation so that the calculated velocity field satisfies the momentum equations and continuity equation.

The stress balance across the air-liquid interfaces is defined by the dynamic boundary, Eqn.(2.9). The weak form of this boundary condition is obtained on the curved interfaces.

$$\int_{\Delta s}\left[-p\,\underline{n}+\mu(\underline{\nabla}\,\underline{u}+\underline{\nabla}\,\underline{u}^{T})\cdot\underline{n}\right]ds = Ca^{-1}\int_{\Delta s}(\kappa\sigma\,\underline{n}+\underline{\nabla}_{s}\sigma)ds-\int_{\Delta s}p_{a}\,\underline{n}ds \qquad (2.13)$$

where Δs is the area of a control surface. The pressure term on the interface is eliminated from the momentum equation along the interface by subtracting the transformed above equation in (ξ,η) from Eqn. (2.10). This new momentum equation is used to determine the pressure equations that involve the interface.

The following procedures describe the SIMPLER algorithms for momentum and pressure equations.

(1) By neglecting the pressure gradients in the momentum equations, the temporary mass fluxes, $\underline{\widehat{F}}$, are calculated:

$$\underline{\widehat{F}}_{P}=\frac{1}{a_{p}}\Sigma a_{i}A_{P}A_{i}^{-1}\underline{\widehat{F}}_{i}\ (i=E,W,N,S)+\frac{1}{a_{p}}A_{P}S_{V} \qquad (2.14)$$

where the coefficients a_i, representing convective and diffusive flux terms, are evaluated by the power-law hybrid differencing scheme [13]; $\underline{\widehat{F}}$ is at velocity node point P and E, W, N, S are four neighboring velocity node points around the point P; S_V is the source

term containing viscous terms and gravity (the right hand side of momentum Eqn. (2.10) excluding the pressure term).

(2) With the values of $\hat{\underline{u}}$ and $\widehat{\underline{F}}$, a tentative pressure is then estimated by solving a pressure equation derived by substituting $\underline{F}_P = \widehat{\underline{F}}_P - \frac{B_{11}}{a_P}\underline{\nabla}_\xi p$ into the continuity equation (2.10). The equation for solving the pressure field is written as:

$$b_p p_P = \Sigma b_i p_i \ (i = E, W, N, S, NE, SE, NW, SW) - \widehat{\underline{F}}_E^{\xi} + \widehat{\underline{F}}_W^{\xi} - \widehat{\underline{F}}_N^{\eta} + \widehat{\underline{F}}_S^{\eta} \qquad (2.15)$$

where E, W, N, S, NE, SE, NW and SW are the eight neighboring pressure grid points around point P.

(3) The momentum equation are solved next to obtain a velocity field using the calculated pressure field:

$$a_p \underline{F}_P^{\ *} = \Sigma a_i A_P A_i^{-1} \underline{F}_i^{\ *} \ (i = E, W, N, S) + A_p S_V - B\underline{\nabla}_\xi p\Big|_P \qquad (2.16)$$

(4) To account for the mass imbalance in a control volume caused by the generation of a velocity field that does not satisfy the continuity equation, the continuity is enforced again to obtain the pressure correction equation for *p'*. The equation for *p'* is similar to the pressure equation (2.15) by replacing p with correction *p'* and replacing the temporary mass flux rate $\hat{\underline{F}}$ with the tentative flux rate $\underline{F}^*$.

(5) Then, the mass flux $\underline{F}$ is calculated from $\underline{F}^*$ and the pressure corrections *p'* by:

$$\underline{F}_P = \underline{F}_P^{\ *} - \frac{1}{a_p} B\underline{\nabla}_\xi p'\Big|_P \qquad (2.17)$$

(6) When surfactant is present, the transport equation (2.12) in the bulk is then integrated in a control volume while the equation (2.11) at the interfaces is integrated along the interface arcs:

$$\begin{aligned} d_p C_p &= \Sigma d_i C_i \ (i = e, w, n, s) + S_c \\ f_p \Gamma_p &= \Sigma f_i \Gamma_i \ (i = e, w) + S_\Gamma \end{aligned} \qquad (2.18)$$

where the bulk concentration C is stored at the same point as pressure; the coefficients d_i, representing convective and diffusive fluxes, are evaluated by the power-law hybrid differencing scheme; S_c represents the secondary-diffusion term as known quantities

from the previous iteration. The interfacial concentration is stored along the interface arc; the coefficients f_i are evaluated by the up-wind scheme; e and w are the neighboring points along the arc; S_Γ is the flux term between the interface and bulk.

(7) Then, a kinematic update scheme [24] is employed to correct the interface shape. The current grid position $\underline{x}_P^N$ of the interface is updated from the previous position $\underline{x}_P^{N-1}$ according to:

$$\underline{x}_P^N = \underline{x}_P^{N-1} + \alpha\left[-\frac{\sqrt{B_{11}}}{a_p}\frac{\partial p'}{\partial \xi}\bigg|_P\right] \tag{2.19}$$

in which the air pressure near the rear meniscus is corrected by the pressure correction values at both interface tips while the air pressure at the front gas phase is reset to be zero.

$$P_1^N = P_1^{N-1} + \left(\frac{\partial p'}{\partial \xi}\Delta\xi\right)_{\text{Rear Tip}} + \left(\frac{\partial p'}{\partial \xi}\Delta\xi\right)_{\text{Front Tip}} \tag{2.20}$$

The origin of the axis is kept at the center point of the plug.

(8) Steps (2) to (9) are repeated until all equations and boundary conditions are satisfied, i.e. all corrections become negligible, which satisfy: $\max\left(\left\|\underline{u}^N - \underline{u}^{N-1}\right\|\right) < 10^{-6}$ and $\max\left(\left\|\underline{x}^N - \underline{x}^{N-1}\right\|\right) < 10^{-3}$ (N is the iteration step).

At far ends of the film regions, the fully developed conditions are applied and the flow rate going out from the precursor films is the same as that coming into the trailing films because of the steady state. This leads to $h_{p+} + h_{p-} = h_{t+} + h_{t-}$. Since the trailing film thickness h_{t+} and h_{t-} are unknown quantities and part of solutions, the precursor films are specified as $h_{p+} = h_{p-} = (h_{t+} + h_{t-})/2$ at each iterative step. The SuperLU solver [25] is used to solve the sparse linear system of the momentum, pressure, pressure correction and surfactant transport equations.

In the grid generation for the plug domain, the film length is 12 units to the right meniscus and 15 units to the left. When the surfactant is present, the film length is 18 units to the right and 27 units to the left. The grid convergence is verified by comparing the trailing film thickness and pressure drops across the plug in different mesh systems. Results with no gravity condition in this chapter agree well with previous studies [1, 3, 4].

2.4 Results

In this section, the effects of gravity (Bo and gravitational orientation α), plug speed, and surfactant are studied. In the plots, the pressure is rescaled with surface tension $P = p^* / \left(\frac{\sigma_M^*}{H} \right) = Ca \cdot p$ for convenience.

2.4.1 Effect of Bo

When there is no gravity, i.e. Bo=0, the plug is symmetric with respect to the channel middle line y=0 and the plug flow in the upper or lower half domain is independent, i.e. no flow interaction between the upper and lower regions. A moving reference frame is chosen with the plug front tip so that the wall velocity $\underline{u}_w = (-1, 0)$. Fig.2.4a shows the streamlines, pressure fields, the corresponding wall pressure $\Pi_w = p_W^* / \left(\frac{\sigma_M^*}{H} \right) = Ca \cdot p_W$ and wall shear stress $\tau_w = \tau_W^* / \left(\frac{\sigma_M^*}{H} \right) = Ca \cdot \left. \frac{\partial u}{\partial y} \right|_W$ of steady plug propagation in a 2-D channel for LP=0.5, Ca=0.05, Re=0 and Bo=0 without any surfactant. In the plug domain, the solid lines with arrows represent the streamlines and the dashed lines indicate the lines of constant pressure. It shows two major flow regions: one is the flow from the precursor film to the trailing film along the wall layer, while the other is the recirculation region in the plug core. The stagnation points, S2 and S5, occur on front and rear interfaces at the midline to separate the upper and lower recirculations. The stagnation points S1 and S3 exist on the front meniscus while S4 and S6 on the rear to separate the wall layer flow and the core recirculation. The front meniscus develops a capillary wave extending into the precursor film, where the film is thinnest and thus the magnitude and gradient of the wall shear stress τ_w is highest. The wall pressure, Π_w, achieves a local minimum and has the greatest slope in the front transition regions with $\Pi_{w\,min}$ = -1.51. The corresponding dimensional value of Π_w can be 300~1200 dyne/cm^2 for the adult human airway generations 7~16. The local maximal magnitude of τ_w in the front transition region $|\tau_w|_{max}$ = 0.193 at x = 0.99 is higher than that in the rear transition region $|\tau_w|_{max}$ = 0.14 at x = -0.79. The corresponding dimensional value of the maximal shear stress can be 40 ~ 160 dyne/cm^2. Higher risk exists due to the presence of the front

meniscus and small dimensions of the airway increases the dimensional values of the wall pressure and shear stresses, which may enhance the risk of the cell damage.

The shear stress due to airflow on the airway walls had been estimated by Nucci et al. [26] for different airway orders, with the maximal value to be 0.3 to 4 dyne/cm^2 during mechanical ventilation and may amplify 5-17 folds for heterogeneous constriction on the airways. Gaver's group [27, 28] studied the propagation of semi-infinite bubble on pulmonary epithelial cells and found $|\tau_w|_{max}$ to be 6~34 dyne/cm^2 and $|\Pi_w|_{max}$ ~ 700dyne/cm^2. Thus the presence of the second meniscus of a plug in the airways increases magnitude of the pressure and shear stress thus increases the risk of the cell damage or negative responses.

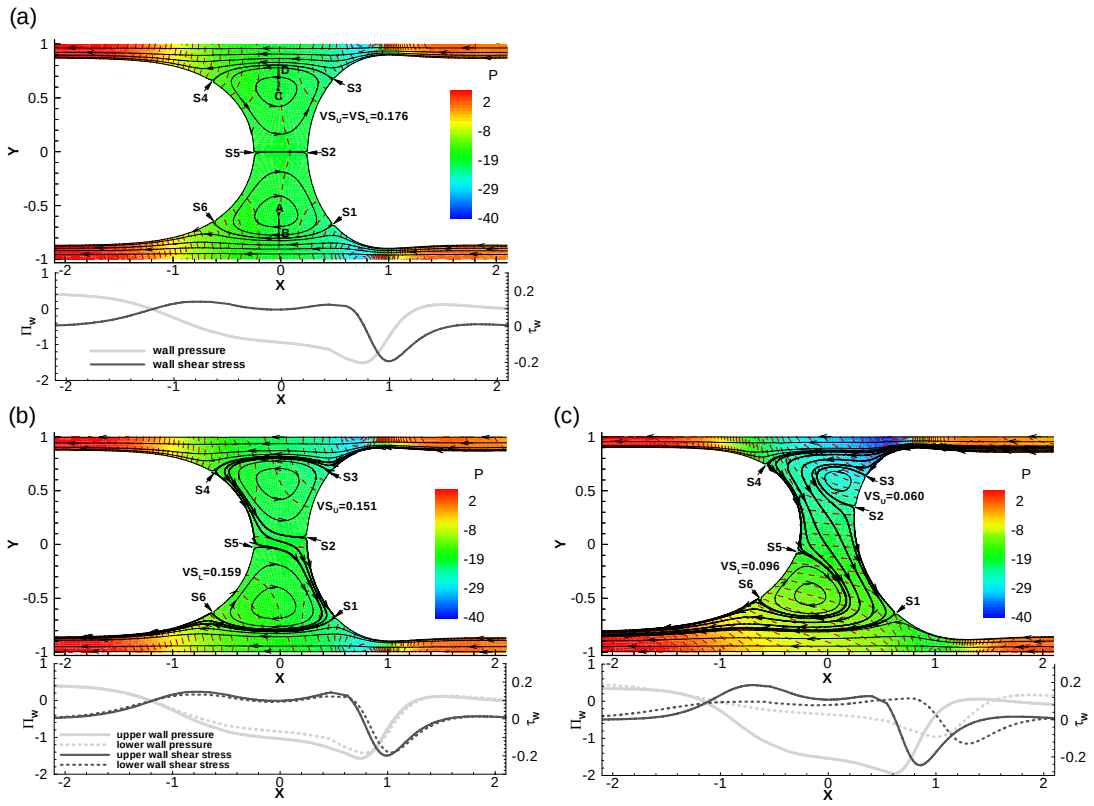

Figure 2.4 The streamlines, the pressure fields, the wall pressure Π_w and wall shear stress τ_w vs. x for LP=0.5, Ca=0.05, Re=0, $\alpha=\pi/2$: (a) with no gravity, Bo=0; (b) Bo=0.1; (c) Bo=0.6. The solid lines with arrows: streamlines, dashed lines: constant pressure. S1-S6: stagnation points. Points A and C are the recirculation centers; B and D are the vertical edges of the recirculations.

The vortex strength (VS) of the recirculations in the plug is examined, defined as the average speed from the center to the edge (A to B and C to D in Fig. 2.4a) of the

recirculations. It is calculated as the flow rate between the centers to the edges divided by the vertical distance. As shown in Fig. 2.4, VS for the upper recirculation is $VS_U = \left| \frac{\psi_D - \psi_C}{y_D - y_C} \right|$, and for the lower one is $VS_L = \left| \frac{\psi_B - \psi_A}{y_B - y_A} \right|$, where ψ is the stream function. For this case, $VS_U = VS_L = 0.176$. The results on the trailing film thickness for LP=2 agree well with numerical studies for the plug propagation [1] and other studies for a semi-infinite bubble propagation [3, 4] in Stokes flow regime with no gravity or surfactant, for example, at Ca=0.05, 0.1 and 0.3, h=0.130, 0.179 and 0.268 respectively in this paper; 0.130, 0.178, and 0.265[1]; and 0.130, 0.172, and 0.251 [4].

When Bo≠0 and $\alpha \neq 0$ or π, there is flow interactions between the upper and lower domains, and the plug becomes asymmetric. Fig. 2.4b & c show the streamlines, pressure fields, Π_w and τ_w for Bo=0.1 (2.4b) and 0.6 (2.4c) at $\alpha = \pi/2$ with the same values of other parameters as 2.4a. The plug is assumed to be instilled into a uniformly-coated lung, i.e. $h_{p+} = h_{p-}$. In the plug domain, it shows three major flows: (1) fluids flow from the upper precursor to upper trailing film and lower precursor to lower trailing film; (2) part of fluids flow from the upper precursor film, through the core region, and into the lower trailing film; (3) recirculations exist in the plug core and each one attach to one interface. The flow separating (1) and (2) leads to one stagnation point S4 on the upper rear meniscus and S1 on the lower front meniscus; each recirculation leads to two stagnation points on the interface, i.e. upper (lower) recirculation attaches the front (rear) meniscus at S2 and S3 (S5 and S6). As Bo increases, S2 and S5 shift further away from the midline, the recirculations are weaker, i.e. VS_U and VS_L decrease, and their centers shift further away from the center line. The upper trailing film becomes thinner while the lower one is thicker as Bo increases. The plug is more skewed to the lower half domain: the transition regions on the upper half domain move toward the centerline while those on the lower one shift further away from x=0. A capillary wave extends the front meniscus into the precursor film and creates the thinnest layer dimension, which decreases in the upper wall layer and leads to increased peak magnitudes and gradients of τ_w and Π_w on the upper wall: $|\tau_{TW}|_{max}$= 0.2 and 0.245 at x = 0.99 and 0.857; $|\Pi_w|_{max}$= 1.57 and 1.947 for Bo= 0.1 and 0.6 respectively. However, the thinnest layer dimension increases and the

peak magnitudes of τ_w and Π_w decrease on the lower wall. Thus, a higher risk of the epithelial cell damage exists on the top wall as Bo increases.

2.4.2 Effect of L_P with Bo≠0

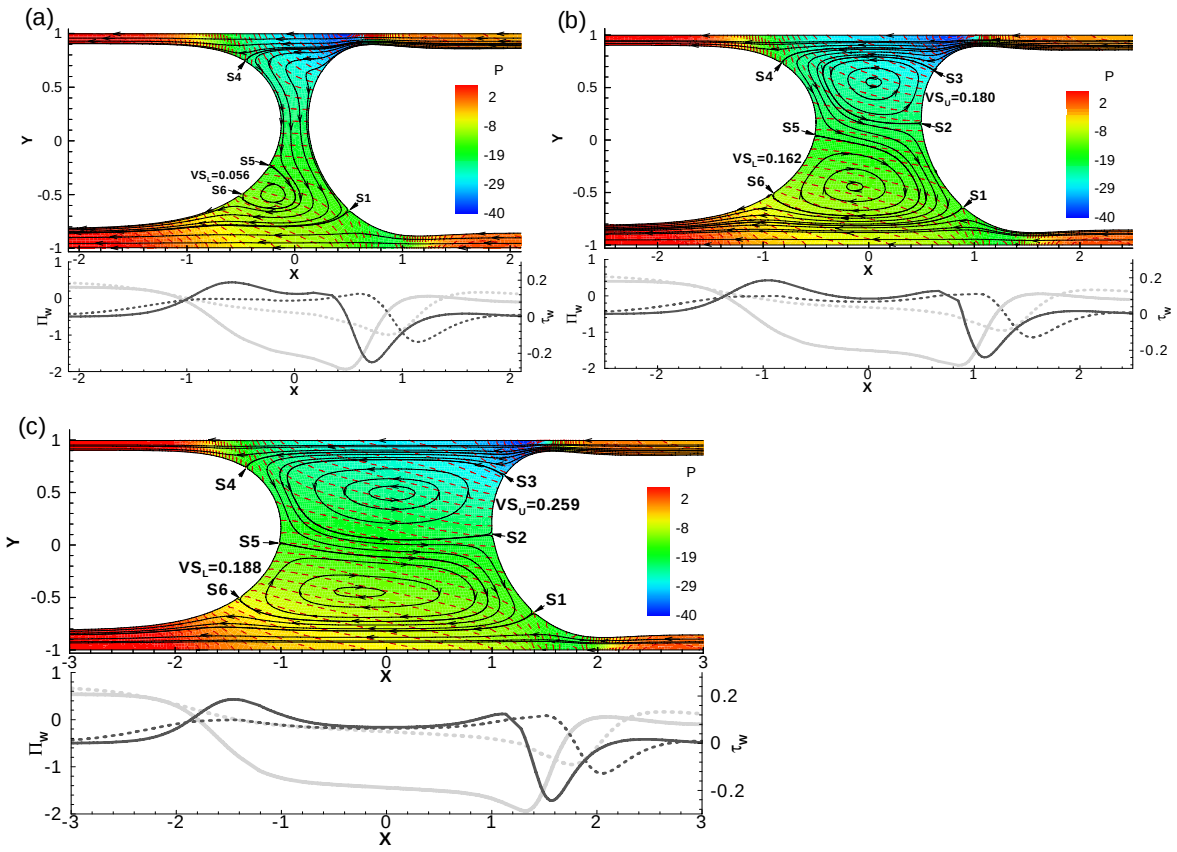

Figure 2.5 The streamlines, the pressure fields, wall pressure Π_w and shear stress τ_w vs. x for (a)LP=0.25, (b) LP=1 and (c) LP=2 at Ca=0.05, Re=0, $\alpha=\pi/2$, and Bo=0.6.

Fig. 2.5 shows the streamlines, pressure fields, Π_w and τ_w for L_P = 0.25 (a), 0.5 (b) and 2 (c) at Ca = 0.05, Re= 0, Bo= 0.6, and $\alpha = \pi/2$ without surfactant. Similar to Fig. 4b&c, there are three major flows in the plug domain while the number of recirculations in the whole domain can be 1 or 2 as L_P changes. The upper recirculation disappears at Bo=0.6 for L_P=0.25, while it remains for $L_P \geq 0.5$ in the range of 0≤Bo≤0.8. When $L_P < 1$, the lower recirculation is stronger than the upper one, i.e. $VS_U<VS_L$, and the recirculation centers move towards the center line x=0 with increasing L_P from 0.25 to 1; while the trend reverses when $L_P \geq 1$: $VS_U>VS_L$ and the recirculation centers shift further away from x=0 with increasing L_P. The x positions of the lower and upper recirculations are x_L=-0.19, -0.15, -0.12, -0.16 and -0.28; x_U=N/A, 0.089, 0.041, 0.047 and 0.054 for L_P=0.25,

0.5, 1.0, 1.5, and 2.0 respectively. The pressure gradients and the shear stress in the transitions regions are almost independent of L_P. The maximal magnitude of τ_w occurs on the top walls with $|\tau_{TW}|_{max}$=0.249, 0.239 and 0.243 at x=0.71, 1.09 and 1.57; and $|\Pi_w|_{max}$=1.933, 1.916, and 1.938 for L_P=0.25, 1 and 2 respectively.

2.4.3 Effect of α

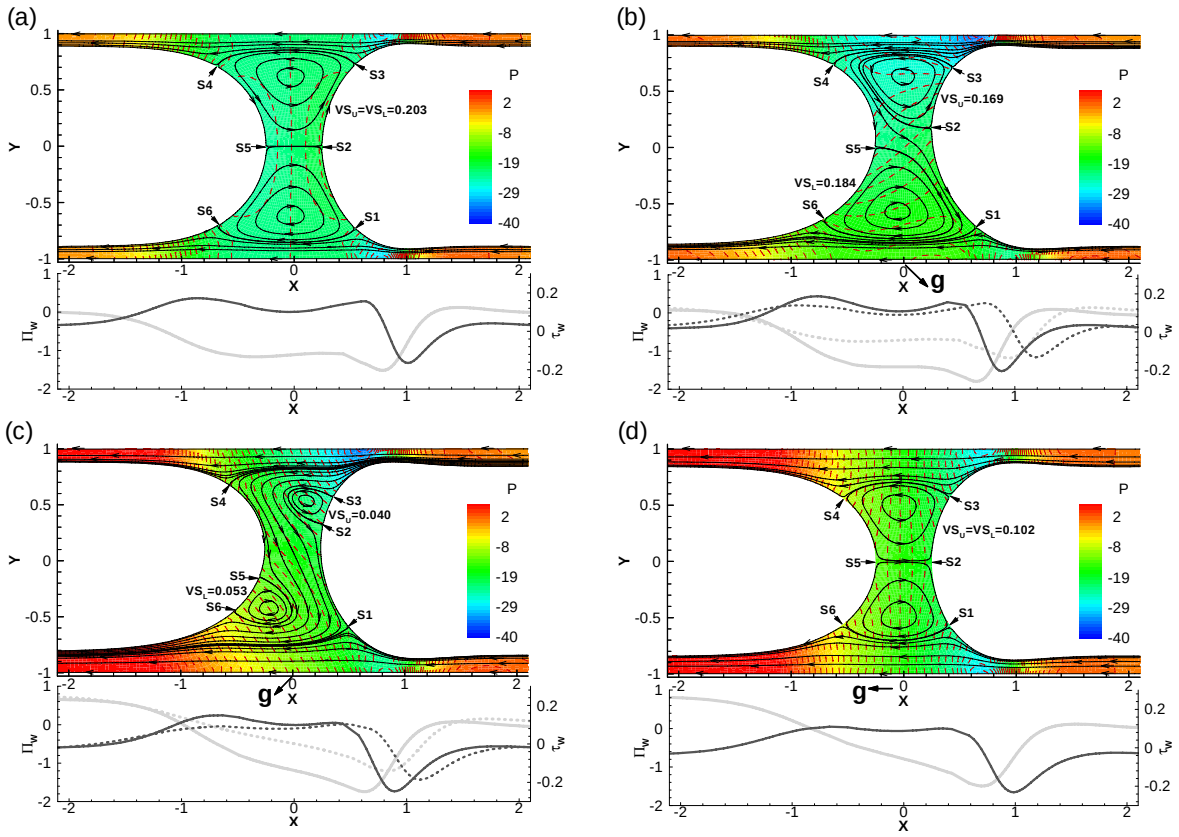

Figure 2.6 The streamlines, the pressure fields, wall pressure Π_w and shear stress τ_w vs. x for (a)α=0, (b) α=π/4, (c) α=3π/4 and (d) α=π at Ca=0.05, Re=0, LP=0.5, and Bo=0.6.

Fig. 2.6 shows the streamlines, pressure fields, Π_w and τ_w for α=0 (a), π/4 (b), 3π/4 (c), π (d) at L_P = 0.5, Ca=0.05, Bo=0.5 and Re=0 without surfactant. As Bo≥0.55, for α=0, the plug is in free fall, thus the flow field is compared at Bo=0.5 in this set of figures. There is a distinct pressure difference from far-upstream to downstream, which is due primarily to the weight of the fluid. At α = 0 or π, the plug is symmetric with the midline and no fluid flows between the upper and the lower half domain. As 0<α<π, the plug mass skews below the mid line, fluid flows from the upper precursor film, through the plug core, and into the lower trailing film. As α increases in 0≤α<π, VS_U and VS_L

decrease, and the recirculation centers shift further away from the center line. Π_w and τ_w have a complicated dependence on α, which is mainly because of the dependence of film thickness on α as discussed below. The decreased film thickness causes the magnitudes and gradients of Π_w and τ_w to increase. Thus $|\Pi_w|_{max}$ and $|\tau_w|_{max}$ always occur in the upper front transition region for $0<\alpha<\pi$ and have slight increases as α increases.

Fig. 2.7 shows the upper to lower film thickness ratio h_{t+}/h_{t-} (2.7a) and the mass left on the trailing films $h_{t+}+h_{t-}$ (2.7b) vs. Bo for different α at L_P=0.5, Ca=0.05, Re=0. It shows in 2.7a that the ratio h_{t+}/h_{t-} is 1 for both α=0 and π and reaches a minimum for $\alpha=\pi/2$. It decreases with increasing α for $0\le\alpha<\pi/2$ but increases with α for $\pi/2\le\alpha\le\pi$. The upper trailing film thickness decreases with increasing α for $0\le\alpha<\pi/2$ while increases with α for $\pi/2\le\alpha\le\pi$ and the inverse is true for the lower trailing film. h_{t+}/h_{t-} is found to decrease with increasing Bo for $0<\alpha<\pi$ but have negligible dependence with L_P. Fig. 2.7b shows that the mass left behind $h_{t+}+h_{t-}$ increases with Bo when $\alpha>\alpha_0$ while the trend is opposite when $\alpha\le\alpha_0$, in which α_0 is found to be $2\pi/5$. For a fixed value of Bo>0, it is shown that the mass left behind increases with α. Thus more fluid can be deposited in the trailing films for larger gravitational orientation α and larger Bo as $\alpha>\alpha_0$.

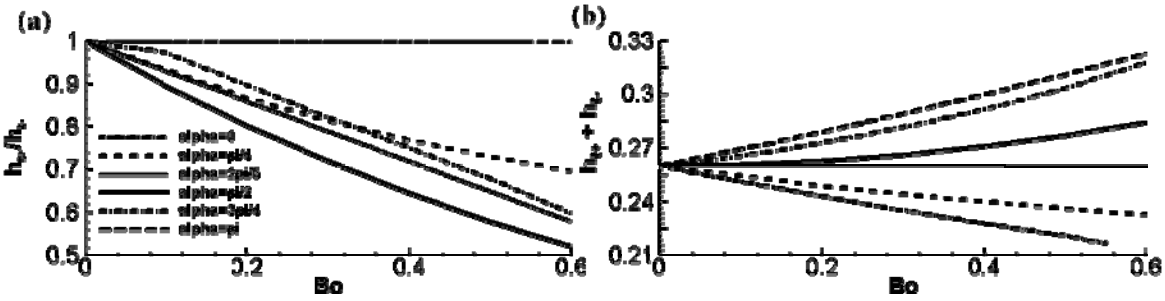

Figure 2.7 (a)The ratio of the upper to lower trailing film thickness h_{t+}/h_{t-} and (b)the mass left behind in the trailing films $h_{t+}+h_{t-}$ vs. Bo for different α at Ca=0.05, Re=0, LP=0.5.

Hazel et al. [29] studied semi-infinite bubble propagation through a 3-D tube. In their work, for Ca=0.05, Bo=0.45 at α=0, Bo=0 and Bo=0.45 at $\alpha=\pi$, the film thickness is equal to 0.110, 0.124, and 0.140. In our paper, for the same parameters, the film thickness is equal to 0.113, 0.130 and 0.153. We showed the qualitative agreement and the quantitative difference is mainly because the difference between tube and channel [4]: the trailing film thickness of semi-infinite bubble propagation in a tube is smaller than

that in a channel. Hodges et al. [30] studied the effect of gravity on the droplet with a lubricant film, which corresponds to the lower half plug in our study. They found that the film thickness is equal to $0.407Bo^{1/4}\alpha$ as α <<1 and Bo<<α^{-1}, in which α is the small tilt angle to the horizontal plane and the gravity acts vertically to the horizontal plane. For comparison, we fitted the lower trailing film thickness vs. Bo with $a*Bo^b$ when Ca=0.05, L_p=2 and gravity acts vertically to the flow direction with 0<Bo≤0.8. We get b≅0.21, which agrees well with [30].

2.4.4 Effect of Ca

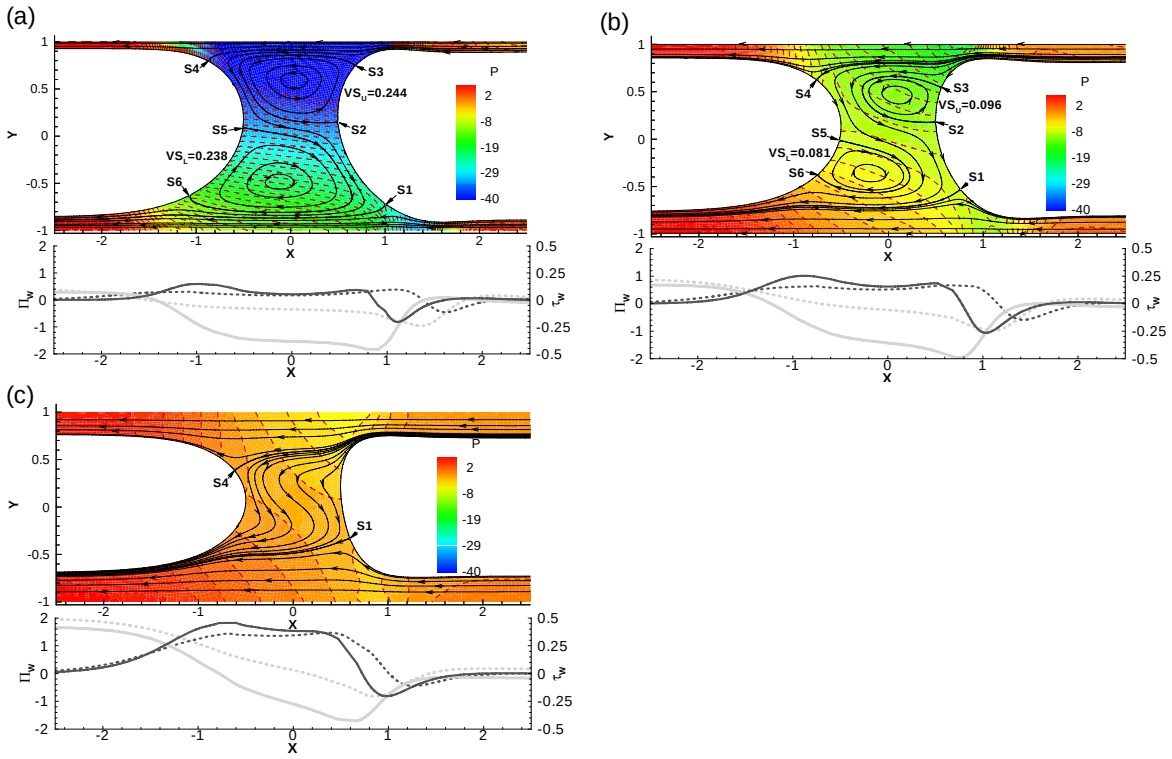

Figure 2.8 The streamlines, the pressure fields, wall pressure Π_w and shear stress τ_w vs. x for Ca = (a) 0.03, (b) 0.1, and (c) 0.3 at Re=0, LP=1, Bo=0.6 and $\alpha=\pi/2$.

Fig. 2.8 shows the streamlines, pressure fields, Π_w and τ_w at Re=0, Bo=0.6, L_P=1, and $\alpha=\pi/2$ for Ca = 0.03 (a), 0.1 (b) and 0.3 (c). The vortices shift further away from the center line x=0 and their strengths decrease with increasing Ca. When Ca=0.3, at Bo=0.6, all vortices disappear in the whole plug domain and only two stagnation points S1 and S4 remain. The fluid in the upper precursor film separates into two branches, one enters the upper trailing film; and the other passes through the whole plug core region and enters the lower trailing film. While for Ca≤0.2 at Bo=0.6, two vortices remain in the plug

domain, thus six stagnation points exist. As Ca increases, the film thickness increases, the amplitude of the capillary wave tends to decrease and the plug is less skewed. Π_w and τ_w are found to increase with Ca on the rear transition regions, which agree with [27]. $|\tau_W|_{max}$=0.457 at x=-0.60 while $|\Pi_w|_{max}$= 1.705 at x =0.67(front transition) on the top wall for Ca=0.3. However, the negative peaks of Π_w and τ_w at the front transition regions seem to have very small dependence on Ca and have smaller magnitude than the ones at the rear transitions at Stokes flow regime.

Fig. 2.9 shows h_{t+}/h_{t-} (a) and $h_{t+}+h_{t-}$ (b) vs. Ca for Bo=0.1, 0.3 and 0.6 at L_P=1, Re=0 and $\alpha=\pi/2$. Fig.2.9a shows that h_{t+}/h_{t-} decreases with increasing Bo but increases with Ca. For small Bo, i.e. Bo=0.1, the ratio increases linearly with Ca, while its trend becomes nonlinear and shows a larger slope for larger Bo, which causes the increases of h_{t+}/h_{t-} with Bo to be larger for smaller Ca. The mass deposition on the trailing films increases largely with Ca while has relatively small dependence on Bo as $\alpha=\pi/2$, as shown in 2.9b. Thus, in the Stokes flow regime, larger speed causes the plug to be more symmetric and more mass to be deposited on the trailing films.

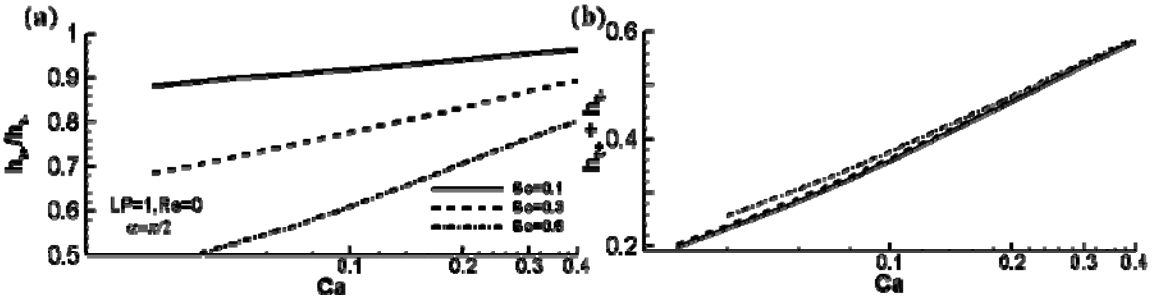

Figure 2.9 (a) The ratio of the upper to lower trailing film thickness h_{t+}/h_{t-} and (b) the mass left behind $h_{t+}+h_{t-}$ vs. Ca for different Bo at Re=0, LP=1 and $\alpha=\pi/2$.

2.4.5 Effect of surfactant

As surfactant is present, the flow is different as shown in Fig. 2.10: the streamlines, the pressure fields, Π_w and τ_w in 2.10a; and the surfactant concentration contour with velocity vectors in 2.10b with $C_0=10^{-4}$, Ca=0.05, Re=0, Bo=0.6, $\alpha=\pi/2$, L_P=0.5, Pe=5 x10^2, Pe_s=5x10^3, $K_a=10^4$, $K_d=10^2$, E=0.7 and $\beta=10^{-2}$. It is shown in 2.10a, the recirculations detach the interfaces, instead, each one forms one saddle point inside the plug core just beneath the interface, unlike the recirculations attach to the interfaces with two stagnation points in the case of C_0=0. Two stagnation points, S1 and S4, still

exist on the interfaces to separate the wall layer flow from the bulk flow and S1 climbs up towards the midline. More surfactant transported from large concentration region, through the core, to the lower film, which increased the bulk concentration in the lower film. Thus, not only the total mass of surfactant on the lower film is larger, but also the bulk surfactant concentration is larger.

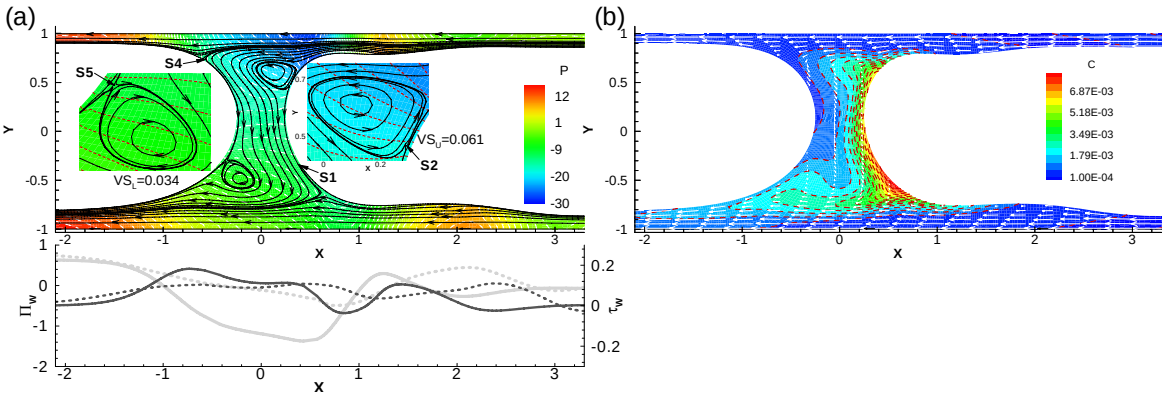

Figure 2.10 (a) The streamlines, the pressure fields, wall pressure Π_w and shear stress τ_w vs. x; (b) the surfactant concentration with velocity vectors in the plug with surfactant at Ca=0.05, Re=0, Bo=0.6, LP=0.5, $\alpha=\pi/2$ with $C_0=10^{-4}$. In 2.10a, the solid lines with arrows are streamlines and the dashed lines are that for constant pressure; in 2.10b, the dashed lines are for constant concentrations and the solid lines with arrows are velocity vectors.

When $C_0=10^{-4}$ (2.10a), the thick films are developed in the front transition region, which leads to the local maximal Π_w and reduced τ_w in this thick film region. $|\tau_W|_{max}=0.183$ at x=-0.735 while $|\Pi_w|_{max}= 1.375$ at x =0.433 in the field. The maximal magnitude of Π_w and τ_w are reduced due to the presence of the surfactant. The film thickness attains a minimum where the thick film connects the lower precursor film, which results in a negative value of shear stress. The thick film region extends longer and is thicker in the lower film than the upper. The maximum surfactant concentration attains the value of $C=7.9\text{x}10^{-3}$ and occurs at the lower front interface due to the surface flow shown in 2.10b, instead of two symmetric locations for the maximum surfactant concentration with respect to the midline as Bo=0. The front interfacial surfactant concentrates near the stagnation point S1 from upstream precursor film, reaches equilibrium and causes desorption from the surface into the bulk. The Marangoni stress opposes the flow, which results in nearly zero velocity in the transition region and developing thick films. The increased concentration in the upstream is then convected

preferentially to the lower trailing film and induces a larger concentration in the bulk and the interface in the lower half of the trailing film.

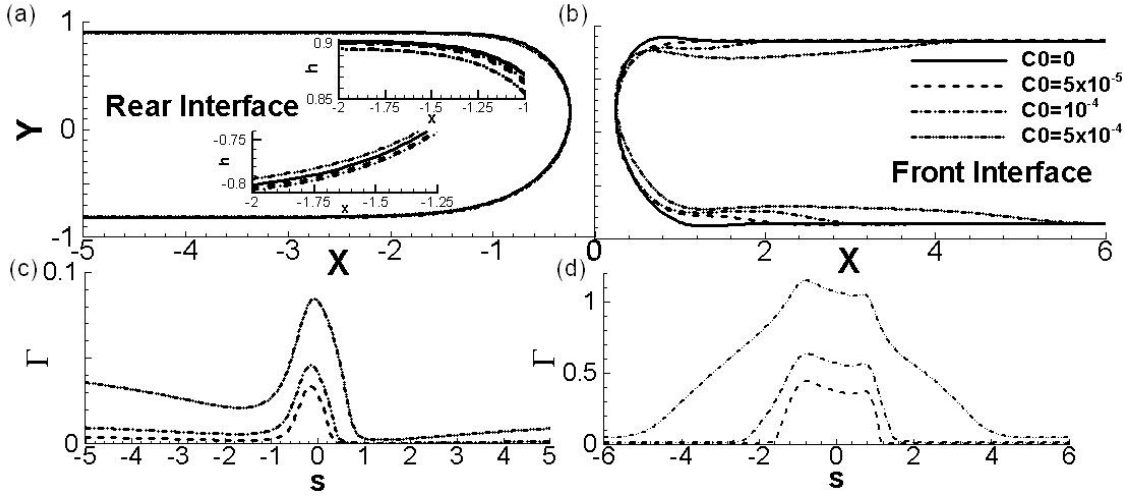

Figure 2.11 The interface position and interfacial surfactant concentration along the interface arc s with different C_0 at Ca=0.05, Re=0, Bo=0.6, LP=0.5, $\alpha=\pi/2$.

Figure 2.11 shows the interface positions and corresponding interfacial surfactant concentration along the arc s for LP=0.5 and Bo=0.6 with C_0=0, $5x10^{-5}$, 10^{-4} and $5x10^{-4}$. s<(≥)0 indicates the interface position at y<(≥)0. The film thickness in the rear interface (2.11a) monotonically decreases along x and the far end film thickness increases with C_0. For C_0=0, the thinnest film thickness occurs in the transition region at the front interface (2.11b), however, as $C_0 \geq 5x10^{-5}$, this minimum disappears. In the transition region of the front meniscus, Γ shows a steep gradient (2.11d), which causes the surfactant accumulated and thick films developed. Gravity causes the surfactant to be convected preferentially to the lower downstream film and lower plug core interface, thus causes Γ to be higher along the interface at the lower plug core and transition region than the upper ones. As C_0 increases, the Marangoni stress affects larger regions of the precursor films; the film extends longer and is much thicker. For $C_0=5x10^{-4}$, the thickest film is about twice the precursor film thickness. Γ at the rear interface increases with C_0 and shows a maximum at the meniscus tip and a minimum in the trailing transition regions. The change of Γ indicates the change of the local surface tension σ, which induces the Marangoni stress that affects the surface flow. As $C_0=5x10^{-4}$, 2.11d shows Γ reaches the maximum value of Γ=1.15 and Γ>1 for -1.28<s<0.86, which means the interfacial

surfactant concentration exceeds the maximum equilibrium concentration. When it attains the maximum dynamic concentration ($\Gamma>\sim1.2$), the surfactant monolayer will buckle and micelles can be formed [10, 31, 32], which is not considered in this study.

As surfactant is present, Fig.2.12 shows the interface positions and the interfacial surfactant concentration for Bo=0, 0.3 and 0.6 with $C_0=10^{-4}$. At the rear interface (2.12a), the lower film thickness increases and the upper one decreases with increasing Bo. At the front interface (2.12b), the lower thick film region extends longer and is thicker while upper one is shorter and thinner with increasing Bo. The interfacial surfactant concentration Γ is shown to decrease with Bo at the rear meniscus tip (2.12c) and the transition regions. Moreover, Γ is found to decrease with Bo at the upper trailing film while increase at the lower one. At the front interface (2.12d), Γ have a larger value and slightly larger gradient in the lower transition region, which causes more surfactant accumulated, thus a thicker and longer film there.

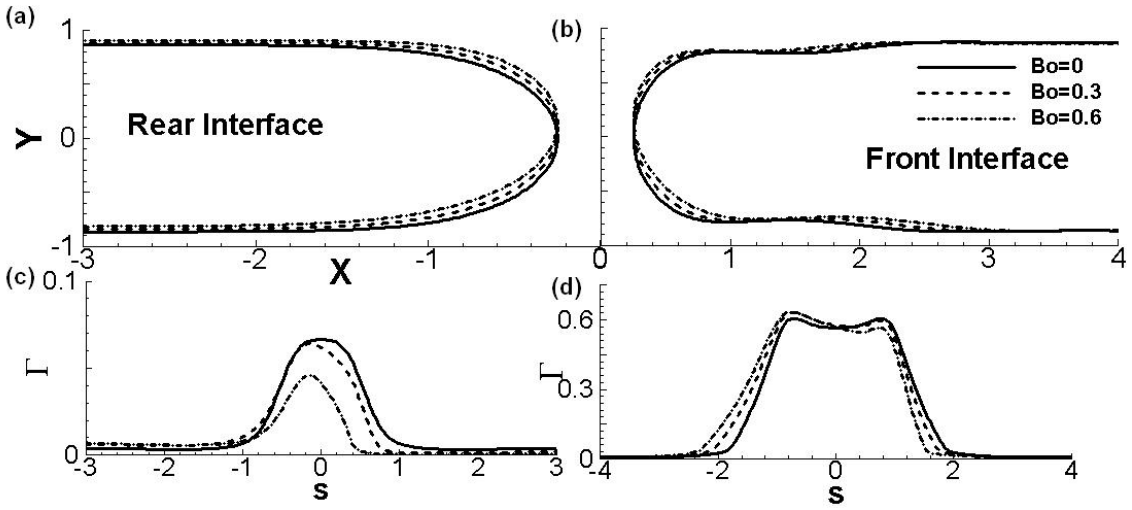

Figure 2.12 The interface position and interfacial surfactant concentration Γ along the interface arc s with Bo=0, 0.3 and 0.6 at Ca=0.05, Re=0, LP=0.5, $\alpha=\pi/2$, $C_0=10^{-4}$.

Fig. 2.13 shows the ratio of the upper and lower trailing film thickness (h_{t+}/h_{t-}) (2.13a) and the mass left behind on the trailing films ($h_{t+}+h_{t-}$) (2.13b) vs. Bo for $C_0=0$, 5×10^{-5}, 10^{-4} and 5×10^{-4} at Ca=0.5, Re=0, $L_P=0.5$ and $\alpha=\pi/2$. The presence of surfactant is found to cause a slight increase on the ratio h_{t+}/h_{t-}, while no further increase on the ratio with increasing C_0 from 5×10^{-5} to 5×10^{-4} (2.13a). The mass left behind $h_{t+}+h_{t-}$ increases with Bo while the slope is higher for $C_0=0$. With the presence of the surfactant, both

upper and lower films become thicker with increasing the surfactant concentration at small Bo, i.e. Bo<0.4, however, for Bo≥0.4, the lower trailing film thickness decreases when C_0 increases from 0 to $5x10^{-5}$ but increases again when C_0 increases from $5x10^{-5}$ to $5x10^{-4}$ and the upper trailing film thickness keeps its increasing trend with C_0. Fig. 2.13c shows the overall pressure drop $\Delta P=p_1-p_2$ across the plug vs. C_0 for Bo=0, 0.3 and 0.6. ΔP is found to increase with C_0 monotonically and a larger slope is shown for $C_0<10^{-4}$, and ΔP shows slight decrease with increasing Bo. In steady state, the pressure drop needed to push the plug is balanced with the drag force on the channels. Thus the overall force on the channels increases with surfactant concentration but have very little change with Bo.

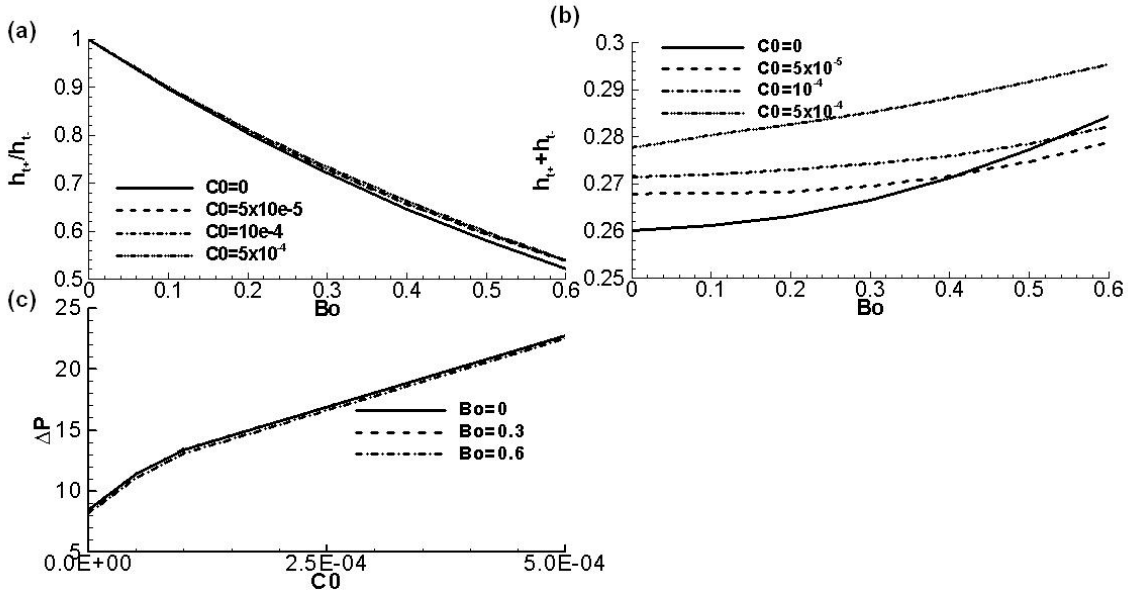

Figure 2.13 (a) The ratio of the upper to lower trailing film thickness h_{t+}/h_{t-}, (b) the mass left behind $h_{t+}+h_{t-}$ vs. Bo for different values of C_0, and (c) the pressure drop ΔP vs. C0 for Bo=0, 0.3 and 0.6 at Re=0, LP=0.5 and $\alpha=\pi/2$.

2.4.6 Effect of Re

Fig. 2.14 shows the streamlines, the pressure fields, Π_w and τ_w at Bo=0.6, $\alpha=\pi/2$, $L_P=2$, $\lambda=1000$, for Re=30 (2.14a) and 50 (2.14b). All the recirculations are centered on the left side of the centerline and skew more to the left with increasing Re with the x positions of them being x_L=-0.540 and -0.645, and x_U=-0.239 and -0.370 respectively. The capillary waves are more pronounced in the precursor films and their amplitudes increase with Re. The peak magnitudes of Π_w and τ_w ($|\tau_W|_{max}$=0.496 at x=1.378 while

$|\Pi_w|_{max}$= 3.45 at x =1.31 at Re=50)increase greatly with Re in the front transition regions, which indicate a significantly higher risk of cell damage on the top wall due to the front meniscus of a plug passing with high inertia.

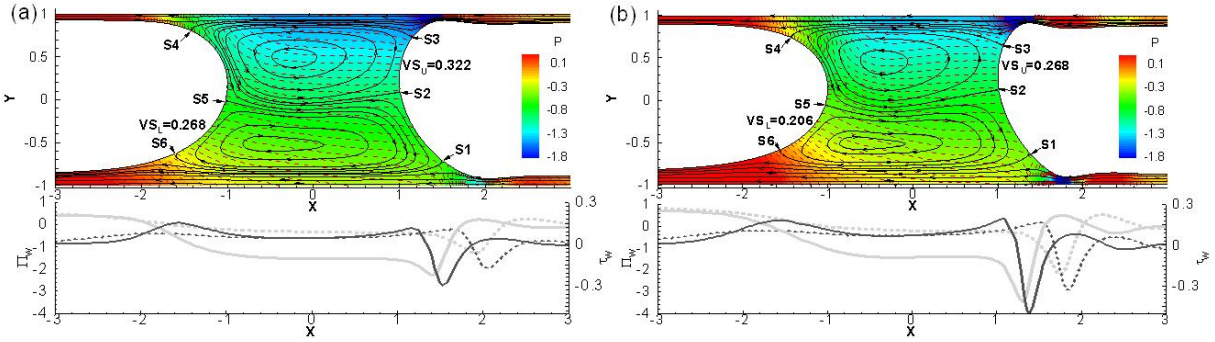

Figure 2.14 The streamlines, the pressure fields, wall pressure Π_w and shear stress τ_w vs. x for (a) Re=30 and (b) Re=50 at L_P=2, Bo=0.6 and $\alpha=\pi/2$.

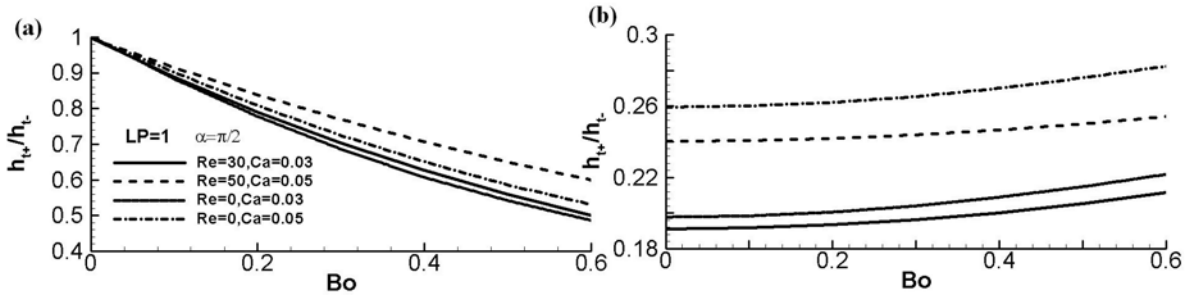

Figure 2.15 (a) The ratio of the upper to lower trailing film thickness h_{t+}/h_{t-} and (b) the mass left behind $h_{t+}+h_{t-}$ vs. Bo for different Re at LP=1 and $\alpha=\pi/2$.

Fig. 2.15 compares the ratio of the upper and lower trailing film thickness h_{t+}/h_{t-} (2.15a) and mass left behind $h_{t+}+h_{t-}$ (2.15b) vs. Bo at Re=0 to that at the same Ca but λ=1000 at L_P=1 and $\alpha=\pi/2$. It is shown that for the same Ca or a fixed λ, as Re increases, the film thickness ratio h_+/h_- increases, which means that inertia leads to a less-skewed plug and more homogenous liquid deposition. For all four cases, more liquid is left behind on the trailing films with increasing Bo as shown in Fig. 2.15b. Increasing Re causes the films become thinner and less mass deposition on the trailing films comparing to the Stokes flow.

2.5 Discussion

The lung airways have a 3-D structure and gravity may play an important role when the liquid plug is instilled into the lung airway. A common protocol in SRT is to turn the patients in different orientations to reduce inhomogeneity during liquid

instillation. The effect of gravity is quantified as well as its combined effects with plug volume, inertia and surfactant in this paper. The plug becomes asymmetric as it propagates with the driving force as both gravity and the pressure gradients from the ventilation. deBisschop et al. [33] have studied the effect of gravity on the bubble propagation with a small volume at Stokes flow regime. In their study, the bubble volume was very small (the dimensionless bubble volume was around 0.2π), strong interactions between the bubble shape and the film thickness, which shows different physics with our present study. There is no region for uniform film thickness. In the present study, the film thickness reaches uniform when $x<-4.08$ and $x>3.66$ for the lower trailing and precursor films, and $x<-3.08$ and $x>3.06$ for upper ones at $Ca=0.05$, $L_P=2$, and $Bo=0.6$. However, the trend in our study agrees well with theirs qualitatively: The plug asymmetry is enhanced with increasing gravity while reduced with increasing the plug speed and surfactant concentration. The lower trailing film thickness increases while the upper one decreases for steady plug propagation as gravity increases with its direction not parallel to the flow. Current study showed that both trailing films decrease with increasing Re or decreasing L_P.

This section compares the combined effects on the wall shear stress and wall pressure. Bilek et al. [27] and Kay et al. [28] have studied the surface tension induced lung epithelial cell damage in a model of airway reopening using a semi-infinite bubble propagating in a fluid-filled and pulmonary epithelial cells lined channel of mm scale. They found that the steep pressure gradient near the bubble front tip was the most likely cause of the observed cell damage. The maximal pressure gradient is found to be 6.96 dyne$\cdot$cm$^{-2}\cdot\mu$m^{-1} and the maximal shear stress and its gradient are 33.7 dyne$\cdot$cm^{-2} and 0.22 dyne$\cdot$cm$^{-2}\cdot\mu$m^{-1}. Fujioka and Grotberg [1] have shown a peak wall shear stress and wall pressure at the minimum precursor film thickness during a liquid plug propagation, which indicates a higher risk of pulmonary cell damage in the front meniscus.

It is found in this study that the wall pressure and shear stress also depend on the gravity. Fig. 2.16 compares Π_w and τ_w on both top and bottom walls against x for $Ca=0.05$, $LP=0.5$ and $\alpha=\pi/2$ at different situations. The bottom wall pressure Π_{BW}, shown in Fig. 2.16a increases with the increases of Bo and C_0, and it increases with Re for the rear half ($x<0$). Π_{BW} attains a minimum and has a sharp peak at the front transition

region, i.e. x= 0.777 at Re=0, C0=0, and Bo=0.1, while this peak magnitude decreases with its position extending to the right, i.e. x=1.018 for Bo=0.6. The peak magnitude of Π_{BW} increases greatly with Re while decreases with C_0. Thus if the epithelial cells are sensitive to the wall pressure, cell damage on the bottom wall has a high risk when the front meniscus of a liquid plug passes with decreasing Bo and C_0 while increasing Re. In the contrast, the peak magnitude of Π_{TW} (2.16b) increases with Bo and Re while has a slight decrease with increasing C_0. And the peak as well as the transition regions shift towards the center line as Bo increases, i.e. x=0.719 and 0.577 for Bo=0.1 and 0.6 respectively at Re=0 and C0=0. Thus cell damage on the top wall has a higher risk at larger Bo and Re, while smaller C_0.

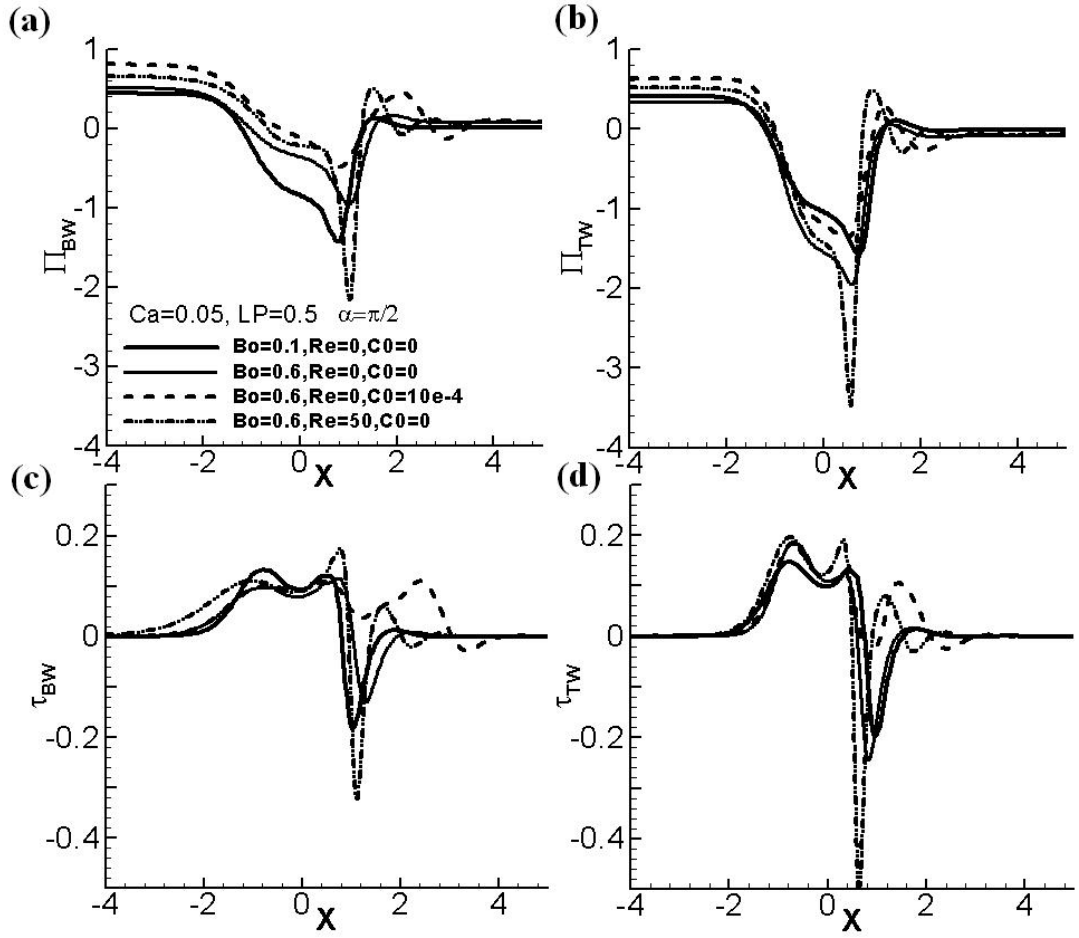

Figure 2.16 Comparisons of bottom wall pressure Π_{BW}, top wall pressure Π_{TW}, bottom wall shear stress τ_{BW} and top wall shear stressτ_{TW} vs. x for different conditions of Bo, Re and C_0.

Fig. 2.16c shows that in the rear half plug (x<0), the bottom wall shear stress, τ_{BW}, has a slight decrease with increasing Bo for the local positive peak. The length of the transition region is longer as Re or Bo increases. In the front part of the plug (x>0), τ_{BW} changes significantly with Bo, Re and C_0. τ_{BW} shows a sharp negative peak at thinnest film region: x=1.038 for Bo=0.1, while this negative peak is reduced and shifts to the right: x=1.303 for Bo=0.6. Increasing Re causes the peak to be enhanced while the presence of surfactant causes τ_{BW} to keep a positive value in the transition region since a thick film region was developed. Thus the risk of cell damage on the lower wall can be reduced by decreasing Re or increasing Bo and C_0. On the top wall as shown in Fig. 2.16d, the local peak of τ_{TW} for x<0 increases with Bo and Re but does not change with C_0, and the length of the transition region decreases with increasing Bo. At the front half plug (x>0), the maximum magnitude of τ_{TW} occurs at the thinnest film as well: x = 0.972 and 0.838 for Bo=0.1 and 0.6 with Re=0 and C_0=0. As Re increases, the peak magnitude increases significantly, this enhances the risk of significant damages on the pulmonary epithelial cells. At the far end films, the wall shear stress is 0 since the flow is nearly uniform in the film region.

To apply these results into the human airways, we quantify the pre-bifurcation asymmetry by the volume ratio (Vr) for the liquid plug distribution. Vr is defined as the ratio of the plug volume above the center line (y=0) to that below the center line: $Vr = \frac{V^+}{V^-}$ as shown in Fig. 2. $V^+(V^-)$ is the plug volume above (below) the center line with x in the range of $x_{t+} \le x \le x_{p+}$ ($x_{t-} \le x \le x_{p-}$) and x_i is defined as the horizontal position where the film thickness is within 1% difference with its far end $h = (1+0.01)h_i$ (i = t-, t+, p+, p-).

Fig. 2.17 shows the volume ratio Vr vs. Bo for different L_P and presence of surfactant (2.17a) and Vr vs. Ca for Bo=0.1, 0.3 and 0.6 (2.17b) at Stokes flow regime with L_P=1 and $\alpha=\pi/2$. When Bo=0, the plug is symmetric and Vr=1. As Bo increases, a larger fraction of the plug volume resides in the lower half of the channel (y<0) and Vr starts to decrease. Increasing L_P, i.e. greater liquid volume, leads to larger Vr. The presence of surfactant (increasing C_0) tends to decrease the asymmetry, hence the liquid

plugs tend to distribute more uniformly. As plug speed increases, Vr increases, as shown in Fig. 17b, and this effect is more obvious for larger Bo. Although the final plug splitting is demonstrated to be determined by the pressure difference on the daughter tubes due to gravity (shown in Chapter 3), the prebifurcation asymmetry (Vr) has been demonstrated here to be as significant as 0.5. Hence faster speed, longer plug or the presence of surfactant all lead to more homogeneous liquid distribution.

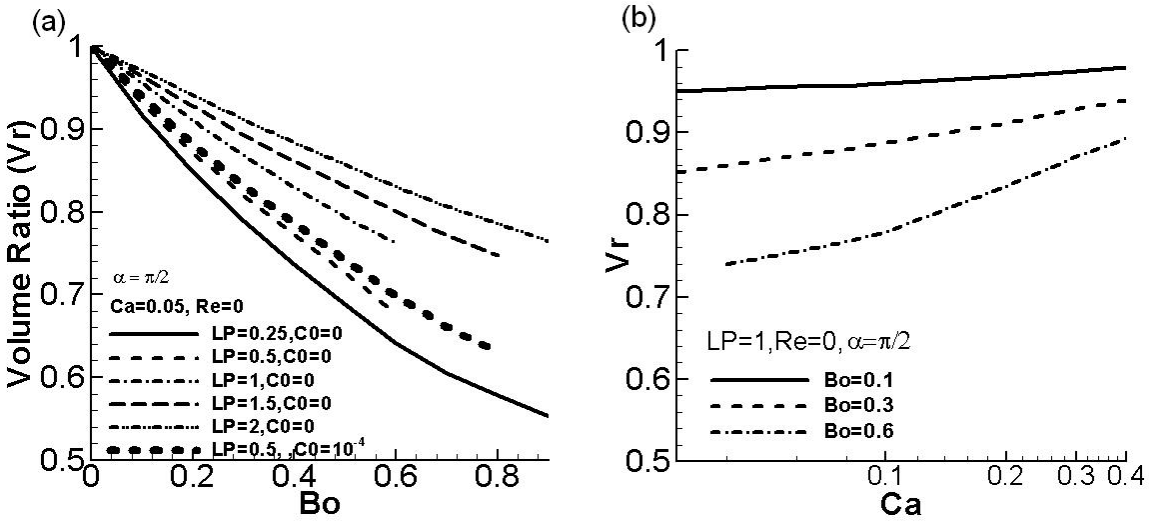

Figure 2.17 (a) The volume ratio Vr vs. Bo for different L_P and C_0, and (b) Vr vs. Ca for different Bo with L_P=1 at $\alpha=\pi/2$ and Re=0.

In this study, there are some limitations in the numerical scheme. The solution is hard to be obtained for low capillary number mainly because the film is too thin to be solved numerically. The computation is unstable when the film is very thin for small Ca and when the upper film thickness tends to be very small for large Bo as well.

When Bo is large, there are some instability issues, such as wet ceiling instability, i.e. the upper films can grow to ridges, and the instability from liquid film flowing down an inclined plane [34], which forms a ridge-like shape on the lower films. In this paper, we did not find the film instability for the range of Bo we studied, thus the film instability is not considered in the present study.

In the modeling process, some other limitations exist. The pulmonary airway branching tube is modeled as a 2-D planar geometry, thus the top and bottom films can only interact through the plug core, which simplifies the simulation. Also, as mentioned in section 2.4, the micelle transport is not considered in this study, rather, a monolayer of

interfacial surfactant transport is simulated without collapse and buckling, hence, the surfactant transport is modeled at a fairly low concentration than that in a healthy lung.

2.6 Conclusion

This chapter investigates the flow and transport phenomena in the plug with the combined effects of gravity, plug speed, volume, airway orientation and the presence of surfactant. It is found that gravity causes the plug to be asymmetric and the flow interactions to occur between the upper and lower half domain. When Bo=0, the flow inside plug is symmetric and independent in the upper and lower half domains. While as Bo>0 and $\alpha \neq 0$ or π, the fluid is found to flow from the upper precursor films, through the plug cores, and enters the lower trailing films. The flow recirculations become weaker with the increase of Bo and the resulting number of vortices can be 0, 1 and 2 depending on the flow parameters. As the surfactant is present, the vortices detach from the interfaces and lead to two saddle points inside the plug core. Capillary waves develop in the front transition regions with the amplitude increases with Bo and Re, which results in an increasing magnitude of wall pressure and wall shear stress and a higher risk of pulmonary epithelial cell damage on the top wall. The pre-bifurcation asymmetry is quantified by the volume ratio and the results show that the asymmetry is enhanced by increasing Bo but reduced by increasing the plug volume, speed and surfactant. The fluid mass deposited in the trailing films is found to increase with increasing Bo for $\alpha > 2\pi/5$, gravity orientation α, plug length L_P and plug speed through Ca. It is also found to increase with C_0 for small Bo (Bo<0.4) while decreases with C_0 as Bo≥0.4.

The study is helpful for understanding the plug flow and transport phenomena in pulmonary airways. It provides some insights for the physical mechanisms on the liquid instillation process and airway reopening.

References

1. Fujioka, H. and J.B. Grotberg, *Steady Propagation of a Liquid Plug In a 2-dimensional Channel.* J. Biomech. Eng. Transaction of ASME, 2004. **126**(5): p. 567-577.
2. Fujioka, H. and J.B. Grotberg, *The steady propagation of a surfactant-laden liquid plug in a two-dimensional channel.* Physics of Fluids, 2005. **17**(8): p. 082102.
3. Giavedoni, M.D. and F.A. Saita, *The axisymmetric and plane cases of a gas phase steadily displacing a Newtonian liquid - A simultaneous solution of the governing equations.* Physics of Fluids, 1997. **9**(8): p. 2420-2428.
4. Halpern, D. and D.P. Gaver, *Boundary-Element Analysis of the Time-Dependent Motion of a Semiinfinite Bubble in a Channel.* Journal of Computational Physics, 1994. **115**(2): p. 366-375.
5. Halpern, D. and O.E. Jensen, *A semi-infinite bubble advancing into a planar tapered channel.* Physics of Fluids, 2002. **14**(2): p. 431-442.
6. Halpern, D., et al., *Unsteady bubble propagation in a flexible channel: predictions of a viscous stick-slip instability.* Journal of Fluid Mechanics, 2005. **528**: p. 53-86.
7. Heil, M., *Airway closure: occluding liquid bridges in strongly buckled elastic tubes.* Journal of Biomechanical Engineering, 1999. **121**(5): p. 487-93.
8. Heil, M., *Finite Reynolds number effects in the Bretherton problem.* Physics of Fluids, 2001. **13**(9): p. 2517-2521.
9. Krueger, M.A. and D.P. Gaver, *A theoretical model of pulmonary surfactant multilayer collapse under oscillating area conditions.* Journal of Colloid and Interface Science, 2000. **229**: p. 353-364.
10. Otis, D.R., Jr., et al., *Dynamic surface tension of surfactant TA: experiments and theory.* Journal of Applied Physiology, 1994. **77**(6): p. 2681-8.
11. Chang, C.H. and E.I. Franses, *Adsorption Dynamics of Surfactants at the Air/Water Interface - a Critical-Review of Mathematical-Models, Data, and Mechanisms.* Colloids and Surfaces a-Physicochemical and Engineering Aspects, 1995. **100**: p. 1-45.
12. Ghadiali, S.N. and D.P. Gaver, *The influence of non-equilibrium surfactant dynamics on the flow of a semi-infinite bubble in a rigid cylindrical capillary tube.* Journal of Fluid Mechanics, 2003. **478**: p. 165-196.
13. Patankar, S.V., *Numerical Heat Transfer and Fluid Flow*. 1980, London: Hemisphere.
14. Thompson, J.F. and Z.U. Warsi, *Boundary-fitted coordinate system for numerical solution of partial differential equations - a review.* Journal of Computational Physics, 1982. **47**: p. 1-108.
15. Cassidy, K.J., et al., *A rat lung model of instilled liquid transport in the pulmonary airways.* Journal of Applied Physiology, 2001. **90**: p. 1955-1967.
16. Ghadiali, S.N. and D.P. Gaver, *An investigation of pulmonary surfactant physicochemical behavior under airway reopening conditions.* Journal of Applied Physiology, 2000. **88**(2): p. 493-506.
17. Schurch, S., *Surface tension properties of surfactant.* Clinics in Perinatology, 1993. **20**(4): p. 669-82.

18. Agrawal, M.L. and R.D. Neuman, *Surface diffusion in monomolecular films, II. experiment and theory.* Journal of Colloid and Interface Science, 1988. **121**(2): p. 366-379.
19. Launoissurpas, M.A., et al., *Behavior of Pure and Mixed Dppc Liposomes Spread or Adsorbed at the Air-Water-Interface.* Colloid and Polymer Science, 1992. **270**(9): p. 901-911.
20. Thompson, J.F., B.K. Soni, and N.P. Weatherill, *Handbook of Grid Generation*. 1999: CRC Press.
21. Wesseling, P., et al., *Computing flows on general two-dimensional nonsmooth staggered grids.* Journal of Engineering Mathematics, 1998. **34**(1-2): p. 21-44.
22. Pantankar, S.V., *Numerical Heat Transfer and Fluid FLow.* London: Hemisphere, 1980.
23. Press, W.H., et al, *Numerical Recipes in C. 2 ed.* Cambridge University Press, 1992.
24. Muzaferija, S. and M. Peric, *Computation of free-surface flows using the finite-volume method and moving grids.* Numerical Heat Transfer Part B-Fundamentals, 1997. **32**(4): p. 369-384.
25. Demmel, J.W., et al., *A supernodal approach to sparse partial pivoting.* Siam Journal on Matrix Analysis and Applications, 1999. **20**(3): p. 720-755.
26. Nucci, G., B. Suki, and K. Lutchen, *Modeling airflow-related shear stress during heterogeneous constriction and mechanical ventilation.* Journal of Applied Physiology, 2003. **95**(1): p. 348-356.
27. Bilek, A.M., K.C. Dee, and D.P. Gaver, *Mechanisms of surface-tension-induced epithelial cell damage in a model of pulmonary airway reopening.* Journal of Applied Physiology, 2003. **94**(2): p. 770-783.
28. Kay, S.S., et al., *Pressure gradient, not exposure duration, determines the extent of epithelial cell damage in a model of pulmonary airway reopening.* Journal of Applied Physiology, 2004. **97**(1): p. 269-276.
29. Hazel, A.L. and M. Heil, *The steady propagation of a semi-infinite bubble into a tube of elliptical or rectangular cross-section.* Journal of Fluid Mechanics, 2002. **470**: p. 91-114.
30. Hodges, S.R., O.E. Jensen, and J.M. Rallison, *Sliding, slipping and rolling: the sedimentation of a viscous drop down a gently inclined plane.* Journal of Fluid Mechanics, 2004. **512**: p. 95-131.
31. Ries, H.E., *Stable Ridges in a Collapsing Monolayer.* Nature, 1979. **281**(5729): p. 287-289.
32. Schief, W.R., et al., *Liquid-crystalline collapse of pulmonary surfactant monolayers.* Biophysical Journal, 2003. **84**(6): p. 3792-3806.
33. DeBisschop, K.M., M.J. Miksis, and D.M. Eckmann, *Bubble rising in an inclined channel.* Physics of Fluids, 2002. **14**(1): p. 93-106.
34. Yih, C.S., *Stability of liquid flow down in inclined plane.* Physics of Fluids, 1963. **6**(3): p. 321-334.

CHAPTER 3

LIQUID DELIVERY AND DISTRIBUTION: SPLITTING – EFFECTS OF GRAVITY AND INERTIA ON LIQUID PLUG SPLITTING IN AN AIRWAY BIFURCATION MODEL

3.1. Introduction

When an initial plug forms in the trachea, followed by an air inspiration, it propagates and splits when it reaches each airway bifurcation. It is expected that the volume of liquid delivered to each branch will depend on gravity: more liquid enters the gravity-favored (lower) branch compared to gravity-opposed (upper) one; and propagation speed: more even splitting with larger speed. These phenomena will repeat at each airway bifurcation and affect the overall liquid distribution in the lung. Thus plug splitting at a single bifurcation is a basic feature of liquid transport in airways and our aim in this chapter is to develop a better understanding of this process by means of experimental and theoretical studies of plug splitting in a benchtop model of an airway bifurcation.

In clinical treatments such as SRT and liquid ventilation, liquid may be instilled in continuous time and liquid plugs may already exist in downstream airways from the previous instillations. The presence of the downstream plugs may affect the liquid distribution, and then affect the efficiencies in later treatments. Understanding the plug splitting with plug blockage in downstream airways will then be beneficial for optimizing the treatment strategies.

Experiments were performed in a benchtop model of an airway bifurcation that was oriented at different angles with respect to gravity. Two types of flow are studied: low Reynolds number (Re) regime and high Re regime. In some experiments a liquid plug

was introduced in one of the daughter tubes to simulate the effect of a liquid plug in downstream airways. Thus the effects of speed, gravity and preexisting downstream plug blockages are studied. Theoretical models of plug transport through an airway bifurcation were developed to predict the splitting ratio as a function of fluid properties, tube geometry, imposed flow rate and gravity and compared with the experimental results in both flow regimes.

Dry tubes were used in our experiments whereas the walls of real airways are lined with a thin liquid layer. As a plug moves through the tube, it deposits a trailing liquid film in the rear. However, a moving solid-liquid-air contact line is present where the front meniscus meets the tube wall. This moving contact line requires additional forces (explained later) acting on the plug that are not exactly representative of real airways. The gravity was assumed to have no effect on the equilibrium contact angle [1]. However, from a practical standpoint, it is more difficult to do experiments with pre-wetted tubes lined with a precursor liquid film [2, 3] since the liquid lining is unstable: hydrodynamic instabilities cause waves on the film surface to amplify [4, 5] and form liquid plugs for thick films [6] or undulate collars in the tubes [7] for thin films. While such instabilities are relevant for airway closure [3, 8, 9], the focus of this study is the effect of gravity on plug splitting. In this study, as the meniscus speed is small, it is expected that the *comparisons* between different orientations depend on gravity, not on the contact line forces. However, the contact line force is a physical force present in our experiments and its magnitude can be as large as the viscous force at low velocities but negligible at high Re flow, so we included this force in the theoretical analysis for plug splitting at low Re regime but not in the flow with high inertia.

3.2. Experimental Methods

Experiments were performed using a bench top model of a physiologic realistic airway bifurcation previously described by [2]. The diameter of the parent tube is 0.40cm (5/32 inch) while that of each daughter tube is 0.32cm (1/8 inch). The branch angle

between two daughter tubes is 60º. The total cross-sectional area increases by 28% from the parent to the daughters. The airway dimensions and area increase accurately represent generations 5 to 7 in the adult human lung [10]. Two clear 10 x 15 x 0.64 cm polycarbonate plates (McMaster-Carr, Elmhurst, IL) were ball-milled as a matching pair using a computerized milling machine and drawings of specifications in Solidworks. The physiological realistic model of Heistracher and Hofmann [11] is used. The detailed description of the bifurcation plate geometry and specifications can be found in [12] based on [11]. The flat inner surfaces of the bifurcation plates were coated with a gasket using Silastic T2 silicone rubber (Dow Corning, Midland, MI) with thickness h < 0.002cm, clamped together and cured for 24 hours to form an airtight seal.

The bifurcation plates were fixed to a platform that could be oriented at different angles with respect to gravity by changing the roll angle ϕ and the pitch angle γ as shown in Figure 3.1 and 3.3. $\phi = \gamma = 0°$, the bifurcation plates were placed iso-gravitationally. ϕ determines the relative gravitational orientation of the two daughter tubes such that as $\phi > 0°$, one daughter tube is lower than the other. γ determines the component of gravity acting along the axial direction of the parent tube: $\gamma >$ (<) 0°, gravity acts along (against) the liquid motion of the parent tube. A liquid plug with the initial length L_0 is instilled manually into the parent tube, which was then connected to a positive displacement pump (Harvard PHD2000, MA) by flexible tubes. The plug, driven by the air flow, propagates and splits across the bifurcation region with the flow rate specified by the air pump.

3.2.1 Low Re Regime

When plug speed is slow, the airway bifurcation model was placed under a video camera (Veo Velocity Connect web camera), which is fixed perpendicular to the test section and connected to a computer, shown in Fig. 3.1. A plug of liquid was injected into the parent tube using a syringe and pumped through the bifurcation into the daughter tubes with air as the driving fluid. Two different liquids, LB-400-X lubricant oil (Union Carbide Chemical) and 99.5% glycerin were used as plug fluids, the properties of which

are shown in Table 3.1. The speed of propagation was controlled by specifying the flow rate at the pump. Plug motion was recorded by the video camera at 30 frames per second and saved to the computer for further analysis. The experiment was repeated five times for each speed and orientation. After each run the system was flushed first with isopropyl alcohol and then deionized distilled water to remove plug fluid deposited on the channel walls. This process was repeated three to five times and the plates were finally flushed with isopropyl alcohol and then dried by blowing dry air at 20 – 25 psi for two minutes. The silicone rubber gasket was replaced once a week or when the plug fluid was changed.

Property\Liquid	DD water	60% glycerin	99.5%glycerin	LB-400X [17]
μ (g/cm/s)	0.01	0.097	9.6	1.51
ρ (g/cm^3)	1	1.16	1.26	0.989
σ (dyne/cm)	72.4	68.1	63.4	30.7
L_0 (cm)	2.0 ± 0.1	2.0 ± 0.1	1.5 ± 0.1	1.5 ± 0.1
L_{b0} (cm)	0.5 ± 0.1			0.7 ± 0.1
V_P	31.4 ± 1.5	31.4 ± 1.57	23.6 ± 1.6	23.6 ± 1.6
V_b	7.85 ± 1.5			7.1±1.5
Bo	0.54	0.65	0.78	1.26
Ca_p	$2x10^{-5}$~$3x10^{-3}$	0.0015~0.015	0.005- 0.11	0.001~0.11
Re_p	2~400	2~30	0.001 – 0.03	0.003~0.3
α_0 (polycarbonate)			56.3º	6.4º

Table 3.1. Materials and flow properties for the four liquids and experimental conditions studied. DD water represents de-ionized distilled water.

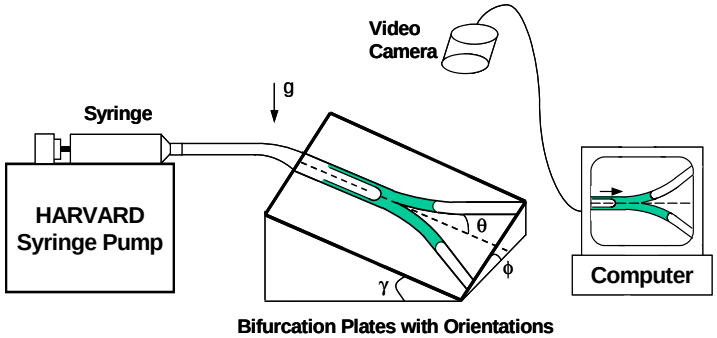

Figure 3.1 Schematic of the experimental setup at low plug speed. The roll angle, ϕ, and pitch angle, γ, describe the orientation of the bifurcation plates with respect to gravity. The branch angle of the daughter tube with respect to the parent tube is indicated by θ.

Two sets of experiments were performed at this regime to examine the effect of gravity on plug splitting. In the first case, experiments were performed at different roll and pitch angles ($\phi = 15°, 30°, 60°; \gamma = -15°, 0°, 15°, 30°$). A snapshot after plug splitting in such an experiment is shown in Fig. 3.2a. In the second case, a second liquid plug was introduced as a blockage into one of the daughter tubes and plug splitting was studied for $\phi = 15°, 30°, 60°$ and γ=0°. A snapshot of such an experiment prior to plug splitting with daughter B blocked is shown in Fig. 3.2b. The scale in the figures is in centimeters.

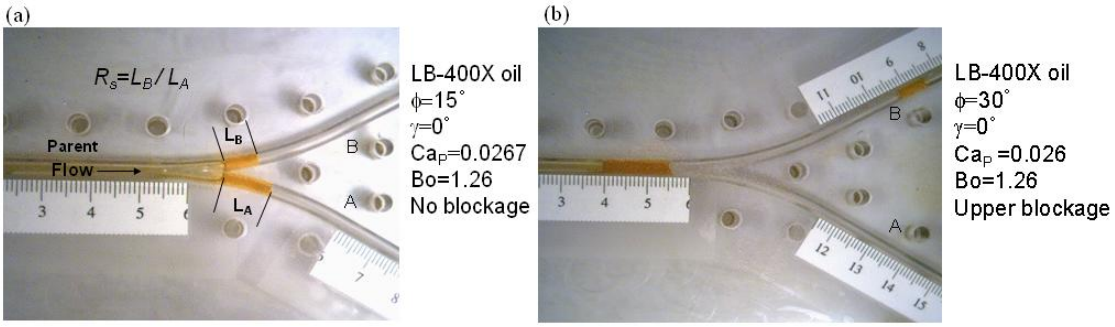

Figure 3.2 (a) Image of the plug immediately after it has entered two daughter branches and split. (b) Image of an experiment with blockage in daughter B.

For each experiment, the saved images were analyzed to measure the lengths L_A and L_B (Fig. 3.2a) as the distance between two meniscus tips of the plugs in the daughter tubes immediately after the rear meniscus of the parent plug passed the carina and separated into two menisci. The propagation speeds of the rear meniscus of parent plug were measured from the recorded plug motion, from which the rear meniscus capillary number $Ca_p=\mu U_p/\sigma$ was obtained (μ and σ are viscosity and surface tension of plug fluid, U_p is rear meniscus speed of the parent plug). A splitting ratio R_s was defined as the ratio of liquid volume in daughter B to that in daughter A immediately after the parent plug splits into two. Since the diameters of two daughter tubes are equal, $R_s = L_B / L_A$. Mean values and standard errors for R_s and Ca_p were calculated from the five runs for each speed and orientation. To minimize the effect of plug size variation on the results,

the parent plug length was measured just before it entered the expanding region of the parent tube and only cases where the plug length was 1.5 ± 0.1 cm were considered. The blockage length was 0.7 ± 0.1 cm.

3.2.2 High Re Regime

Fig. 3.3 shows the schematic of the experimental setup at finite Reynolds number regime. Two liquids are chosen for the experiments: deionized distilled water and 60% glycerin. The properties of LB-400X, 99.5% glycerin, 60% glycerin and deionized water are shown in Table 3.1. The viscosities of the liquids are measured using a falling ball viscometer and their surface tensions are measured using a capillary glass tube. The liquid plugs are injected into the parent tube using a syringe and pumped through the bifurcation into the daughter tubes using a syringe pump with air as the driving fluid. A differential pressure transducer (2641005WB, Setra, MA) is connected to the inlet using a T-tube section to measure the pressure drop of the plug as shown in Fig.3.3.

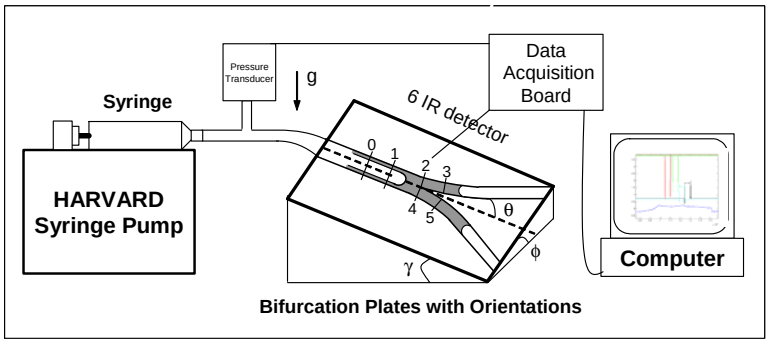

Figure 3.3 Schematic of the experimental setup of plug splitting at finite Reynolds flow regime. 0, 1, 2, 3, 4 and 5 indicate 6 IR sensors for the parent and two daughter tubes.

The plug velocities and length in parent and both daughter tubes are then measured using the technology developed by [13]. They used pairs of IR sensors to measure the flow velocities and lengths of the two- and three-phase slugs, each pair of which consist of a light source (IR emitter) and a light-detecting sensor (photodiode detector). When a liquid plug meniscus is passing, the sensor detects a difference in absorption and a binary signal is obtained. Fig. 3.4a shows a schematic of the measurement for plug velocity and

length using IR sensors. When the front and rear menisci pass the IR sensors, 0 and 1, binary signals are recorded. With the distance between two sensor pairs and the time difference of the front (rear) meniscus passing 0 and 1, the velocity of front (rear) meniscus can be measured, thus the plug length can be calculated from their average. Hence, the same IR sensors are selected in this study: Type TSAL4400, Vishay Telefunken with peak wavelength 940 nm is used for the IR emitting diode; and the IR detector is Type TSL261, Farnell. Data acquisition from the pressure transducer and IR sensors are performed using a USB-based A/D board (PMD-1608FS, Measurement Computing). The board is capable of sampling 8 channels and the maximum sampling rate is 100KHz. Raw data signals are stored and processed afterwards. All the experiments are performed at sampling rates of 4-10 kHz/channel.

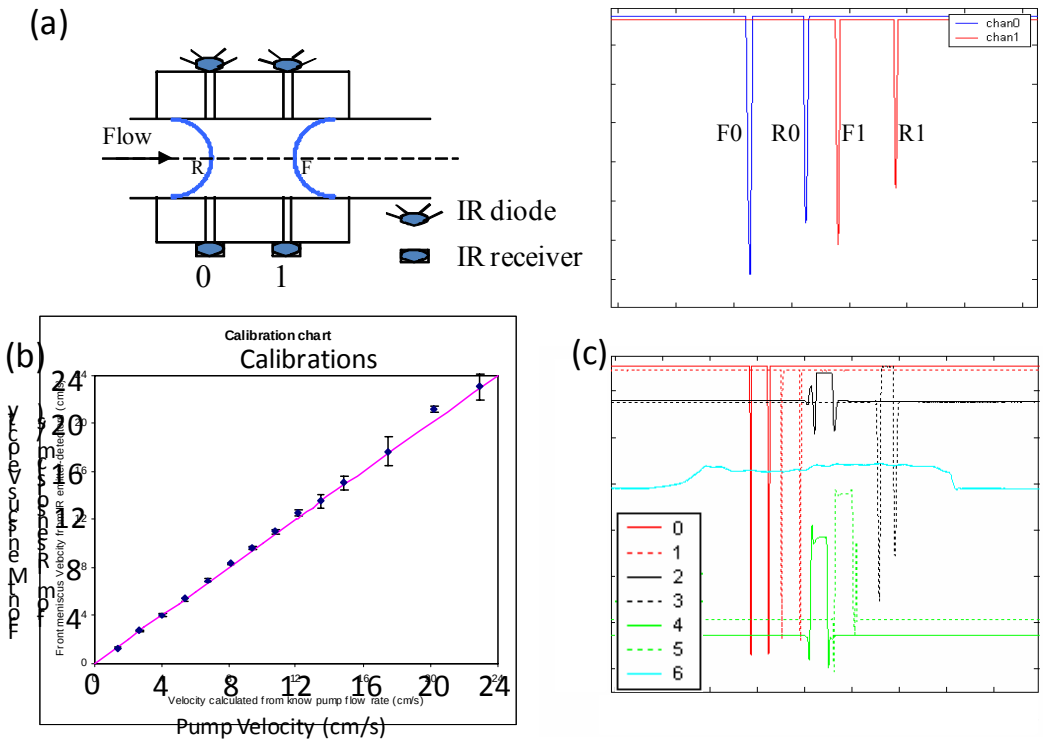

Figure 3.4 (a) Schematic of the measurement of plug velocity / length by two pair of IR sensors and the sample binary signal of meniscus recording. (b) The calibration chart of the front meniscus velocity measured from IR sensors vs. that from the pump flow rate in a 4mm glass tube. (c) The sample signal of the experiment. 0 and 1 is the binary signal of the menisci of the parent plug; 2 and 3 is the signal for upper daughter; 4 and 5 for lower daughter; and 6 is the pressure signal.

Fig. 3.4b shows the calibration chart of average velocity measurement from the IR sensors vs. velocity generated from the pump as a water plug propagates in a long straight glass tube with diameter 4mm. The film thickness is expected to be $O(10^{-4})$-$O(10^{-2})$ since the water viscosity is very small and its capillary number is in the range of $O(10^{-6})$-$O(10^{-3})$. Thus, these thin films are expected to have negligible effects on the average velocity measurement. The symbols in the figure show the data measured and the straight line has a function y=x. The square of the correlation coefficient R^2=0.99, which is nearly 1, justified the use of IR sensors for our measurement.

In the parent tube, the IR sensors, shown as 0 and 1 in Fig. 3.3, are positioned before the bifurcation region starts with the distance 1.62cm between them. In the daughter tubes, one pair of IR sensors is put just after the bifurcation region for each daughter tube (2 and 4 in Fig. 3.3) and another pair is put 0.72cm downstream of each daughter, shown as 3 and 5 in Fig. 3.3. Fig. 3.4c shows sample signals of pressure and meniscus recordings during plug splitting across the bifurcation. 0 and 1 show the binary signals for the parent plug passing two IR sensors, where the plug passes the acceleration stage and has a steady motion, i.e. the pressure curve (signal 6) passes the maximum and goes to a stage which is nearly constant. The plug is expected to be steady before it reaches the bifurcation region, therefore, the pressure signal is recorded to make sure that the plug velocity in the parent tube is measured after the plug passes the acceleration stage and have a steady motion. As the plug reaches the bifurcation region, it splits into two: signals 2 and 4 record the two menisci in the upper and lower daughter tube just after the bifurcation region respectively. 3 and 5 show the recorded signals for the plug moving downstream in the upper and lower daughter tubes. The pressure (signal 6) increases and goes to a steady value again as the plugs pass the bifurcation region.

Two sets of experiments were performed in this finite Reynolds number regime to examine the effects of inertia as well as gravity on plug splitting. In the first case, experiments were performed at different roll and pitch angles (ϕ=15°, 30°, 60°; γ= -15°,

0°, 15°) without any downstream blockages to study the plug splitting driven by the air pump and gravity. Deionized water is the plug material except when ϕ=30°, both water and 60% glycerin are used, the results of which will be compared with LB-400X at low Re regime. In SRT or partial liquid ventilation, a clinical procedure will be set so that small plugs will be instilled into the lung continuously instead of a one-time instillation of a long plug to avoid choke or poor gas exchange from the acute airway obstruction. So in clinical situations, liquid plugs may exist from the previous treatments in downstream airways, which will affect the liquid distribution and the efficiencies of the later treatments. Therefore, in the second case, a secondary liquid plug was introduced as a liquid blockage into one daughter tube and experiments was performed at ϕ=15°, 30°, 60° and γ=0° with deionized water. For each experiment, the recorded signals are analyzed afterwards to obtain the information of the front/rear meniscus velocities and plug length in parent/daughter tubes. The splitting ratio R_s and the total volume ratio will be studied as the function of inertia, gravity and the blockage length.

3.2.3 Parameter Definitions

The relevant parameters include the physical properties of the liquids (viscosity μ, density ρ and air-liquid surface tension σ), parent plug velocity (U_p), the parent plug volume (V_p^*), gravitational acceleration (g), roll and pitch angles (ϕ, γ), branch angle θ, contact angle at the front interfaces α, parent tube radius (a_1) and the daughter tube radius (a_2). The speed of the rear meniscus in the parent tube is chosen to characterize the plug speed, since it can be easily measured from the recorded images. For the blocked tube experiments, the volume of the blockage V_b^* is another parameter. These parameters are combined to obtain the following non-dimensional groups: Capillary number $Ca_p = \mu U_p / \sigma$, Bond number $Bo = \rho g a_1^2 / \sigma$, Reynolds number $Re_p = \rho U_p a_1 / \mu$, dimensionless plug length $L_p = L_p^* / a_1$, dimensionless blockage length $L_b = L_b^* / a_1$, the radius ratio a_2/a_1, and angles θ, ϕ, γ and α. Ca_p and Bo represent the ratio of viscous and gravitational forces, respectively, to surface tension force, while Re_p represents the ratio

of inertial to viscous forces. In Stokes flow regime, the most important parameters are Ca_p (controlled by changing U_p), ϕ, γ and Bo. Inertia of the plug fluid can be neglected if Re_p is small, which is true for the liquids and small velocities used. In large airways as discussed in [14], Re_p is ~ O(10) to O(10^3), thus inertia may play a very important role for the liquid plug transport and splitting. The purpose of these experiments in finite Reynolds regime focus on the effects of Re_p, ϕ, γ, and Bo on R_s.

3.3 Theoretical Analysis

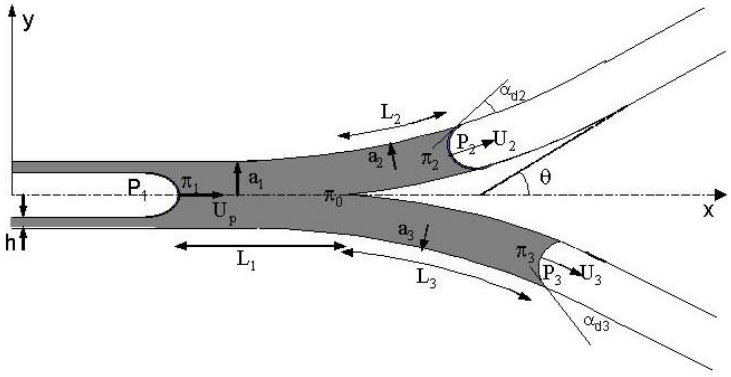

Figure 3.5 Schematic of the theoretical model of plug flow through a bifurcation. a_1, a_2 and a_3 are the radius of the parent, upper and lower daughter tube respectively. P_1 is the pressure of the pumped air. P_2 and P_3 are atmospheric pressure. L_1, L_2 and L_3 are the plug lengths in the parent, upper and lower daughter tube respectively. π_1, π_0, π_2 and π_3 are the pressures in the liquid plug at the rear interface, bifurcation zone, front meniscus of upper daughter and front meniscus of lower daughter respectively. U_p, U_2 and U_3 are the plug velocities of rear meniscus in parent tube and front menisci in upper daughter and lower daughter tubes.

To better understand the fluid transport of plug splitting process, theoretical models are developed to predict or compare the experimental results. A schematic model of plug splitting with all the dimensions is shown in Figure 3.5. For simplification, the curved tubes of the experimental bifurcation model are replaced by straight tubes. The branch angle in the experiments is a function of the distance from the bifurcation, since the proximal segments of the daughter tubes have a non-zero axial curvature. The initial value of the branch angle at the bifurcation is θ=10° and the distal value starting at

approximately 3 cm from the bifurcation is θ=30°. For the theory we selected a constant average value, $\theta = 20°$. The plug lengths were shorter than 3 cm, so this seems a reasonable approximation. The motion of the plug is considered to be quasi-steady and expressions for the splitting ratio R_s are derived by a theoretical calculation of the pressure drops and mass balances between the parent and daughter tubes. The effect of gravity on the meniscus shape of the air-liquid interface is neglected. The pressure drop between the parent and daughter tubes has different contributions. It includes the capillary jump across the air-liquid interfaces, viscous resistance estimated with Poiseuille's law, gravitational hydrostatic effects and the effect of moving contact lines at Stokes flow regime at the air-liquid interface in the daughter tubes.

The mass balance and definition of the splitting ratio are shown as follows. The flow rate in the parent tube must be equal to the sum of flow rates in the daughters, i.e.

$$Q_1 = Q_2 + Q_3 \tag{3.1}$$

$$R_s = \frac{Q_2}{Q_3} = \frac{U_2}{U_3} = \frac{\overline{U}_2}{\overline{U}_3} = \frac{L_2}{L_3} \tag{3.2}$$

where $Q_i = \pi a_i^2 U_i$ is the flow rate in the parent tube(i=1) and daughter tubes(i =2,3) with a_i, U_i and $\overline{U}_i$ being the radius, mean front meniscus and mean plug speed. Since our bifurcation model is symmetric, we have a_2=a_3. U_1 is the speed of the front meniscus of the plug in the parent tube. It can only be defined till the meniscus enters the daughter tubes at the beginning of splitting. Later in the section we will relate U_1 to the rear meniscus speed U_p in the parent tube which can be defined till plug splitting is complete. L_2 and L_3 are the lengths of the liquid plug in the daughter tubes at any time. From (3.1) and (3.2) the flow rates, capillary numbers, Reynolds number, and plug length in the daughter tubes can be related to those in the parent tube as

$$Q_2 = \frac{R_s}{R_s + 1} Q_1, \quad Q_3 = \frac{1}{R_s + 1} Q_1; \tag{3.3}$$

$$Ca_2 = (\frac{a_1}{a_2})^2 \frac{R_s}{R_s+1} Ca_1,\ Ca_3 = (\frac{a_1}{a_2})^2 \frac{1}{R_s+1} Ca_1 \tag{3.4}$$

$$\mathrm{Re}_2 = (\frac{a_1}{a_2})^2 \frac{R_s}{R_s+1} \mathrm{Re}_p,\ \mathrm{Re}_3 = (\frac{a_1}{a_2})^2 \frac{1}{R_s+1} \mathrm{Re}_p \tag{3.5}$$

The theoretical analyses are performed as follows in two regimes respectively.

3.3.1 Low Re Regime

Suppose L_0 is the plug length in the parent tube just as the front meniscus reaches the bifurcation. As the plug moves towards the daughters, it deposits a trailing film of thickness h in the parent tube. Let the plug length in the parent tube be $L_1 < L_0$ when the plug has partially entered the daughter tubes, as shown in Fig. 3.5. Conservation of liquid mass requires the following relationship to be satisfied.

$$\pi a_1^2 L_0 - (\pi a_1^2 - \pi(a_1 - h)^2)(L_0 - L_1) = \pi a_2^2 (L_2 + L_3) \tag{3.6}$$

From (3.2) and (3.6) we then obtain

$$L_3 = (\frac{a_1}{a_2})^2 \frac{L_0 - (1-(1-\frac{h}{a_1})^2)(L_0 - L_1)}{R_s+1} \tag{3.7}$$

Numerical studies by [15] showed that, when liquid inertia and gravity are neglected, h depends on the speed of propagation and the tube radius according to the relation

$$\frac{h}{a_1} = 0.36\left(1 - e^{-2Ca_p^{0.523}}\right), \tag{3.8}$$

where Ca_p is a capillary number based on the speed U_p of the rear meniscus. We use (3.8) as an approximate expression for the trailing film thickness in our theoretical model. Liquid inertia is neglected at the small speeds of the experiments, however (3.8) does not consider variations of the trailing film thickness along the tube circumference due to gravitational effects. U_p is related to the mean front meniscus speed U_1 by

$$Q_1 = \pi a_1^2 U_1 = \pi(a_1 - h)^2 U_p, \tag{3.9}$$

So

$$Ca_1 = \left(1 - \frac{h}{a_1}\right)^2 Ca_p . \tag{3.10}$$

Now consider the pressure drop between the parent and daughter tubes. In the parent tube, the difference between the air pressure P_1 and the liquid pressure π_1 at the rear meniscus is equal to

$$P_1 - \pi_1 = \frac{2\sigma}{a_1 - h}. \tag{3.11}$$

which represents the Young-Laplace law for the capillary pressure jump across a *static* hemispherical interface whose radius r is equal to the tube radius minus the film thickness ($r = a_1$-h). Since the meniscus velocity is very small, the viscous effect is neglected for the pressure drop across the interface. The pressure drop within the plug liquid is approximated by the Poiseuille law for flow in tubes. For long plug length and small capillary number, this assumption is valid and simplifies the calculations. We neglect the entrance effects and secondary flows that prevail when liquid enters the daughter tubes. We do not expect these features to have much effect on the splitting ratio since the inertia is negligible and capillary number is small. Also, a hydrostatic pressure drop resulting from gravity is included. Thus, in the parent tube

$$\pi_1 - \pi_0 = \frac{8\mu Q_1 L_1}{\pi a_1^4} - \rho g L_1 \sin\gamma \tag{3.12}$$

Similarly, pressure drops can be written for the upper daughter (Eqn.(3.13)) and lower daughter (Eqn.(3.14)).

$$\pi_0 - \pi_2 = \frac{8\mu Q_2 L_2}{\pi a_2^4} + \rho g L_2 (\sin\theta \sin\phi - \cos\theta \sin\gamma) \quad \textit{(B, upper)}, \tag{3.13}$$

$$\pi_0 - \pi_3 = \frac{8\mu Q_3 L_3}{\pi a_3^4} - \rho g L_3 (\sin\theta \sin\phi + \cos\theta \sin\gamma) \quad \textit{(A, lower)}. \tag{3.14}$$

The capillary jumps at the air-liquid-solid interfaces in the daughter tubes are given by

$$\pi_2 - P_2 = -\frac{2\sigma}{a_2}\cos\alpha_{d2} \tag{3.15}$$

$$\pi_3 - P_3 = -\frac{2\sigma}{a_3}\cos\alpha_{d3} \tag{3.16}$$

where the dynamic contact angles α_{d2} and α_{d3} depend on the speed of the interfaces, and hence on the front meniscus capillary numbers, Ca_2 and Ca_3. This dependence was modeled using an empirical correlation given by Bracke *et al.* [16]

$$\frac{cos\ \alpha_d - cos\ \alpha_0}{cos\ \alpha_0 + 1} = -2Ca^{1/2} \tag{3.17}$$

where α_0 is the static contact angle at the three phases contact line. The equation (3.17) is an empirical equation which predicts the dependence of the dynamic contact angle on the static contact angle and the meniscus capillary number under air entrainment conditions. The equation was obtained from the experiments with a strip drawn into a large pool of liquid. We also tried one of the first empirical correlations given by Jiang et al. [17], which is based on data published by Hoffman [18] from a study of non-polar liquids forced to spread through a glass capillary tube,

$$\frac{cos\ \alpha_d - cos\ \alpha_0}{cos\ \alpha_0 + 1} = -tanh(4.96Ca^{0.702}), \tag{3.18}$$

The two correlations give results which are within 5-10%. In our study, the capillary number covers from 10^{-3} to 10^{-1}. Bracke *et al.* [16] gave a relatively simple correlation and matches the range of capillary number we investigated.

When there is no blockage in the daughter tubes, the difference in the air pressure between the parent and the two daughter tubes can be found by combining Eqns. (3.11) - (3.18) to be

$$P_1 - P_a = \frac{2\sigma}{a_1 - h} - \frac{2\sigma}{a_2}\cos\alpha_{d2} + \frac{8\mu Q_1 L_1}{\pi a_1^4} - \rho g L_1 \sin\gamma + \frac{8\mu Q_2 L_2}{\pi a_2^4} + \rho g L_2(\sin\theta\sin\phi - \cos\theta\sin\gamma) \tag{3.19}$$

$$P_1 - P_a = \frac{2\sigma}{a_1 - h} - \frac{2\sigma}{a_3}\cos\alpha_{d3} + \frac{8\mu Q_1 L_1}{\pi a_1^4} - \rho g L_1 \sin\gamma + \frac{8\mu Q_3 L_3}{\pi a_3^4} - \rho g L_3(\sin\theta\sin\phi + \cos\theta\sin\gamma) \tag{3.20}$$

Equating (3.19) and(3.20), using (3.1)-(3.10), an equation relating R_s and the other parameters is obtained:

$$8\left(\frac{a_1}{a_2}\right)^4 Ca_p(1-\frac{h}{a_1})^2(R_s-1) + Bo(R_s+1)\sin\theta\sin\phi - Bo(R_s-1)\cos\theta\sin\gamma + 4\left(\frac{a_1}{a_2}\right)^2 \frac{\left[Ca_p(1-\frac{h}{a_1})^2\right]^{\frac{1}{2}}(\cos\alpha_0+1)}{(L_3/a_1)} \frac{(R_s^{1/2}-1)}{(R_s+1)^{1/2}} = 0 \tag{3.21}$$

Equation (3.21) is solved numerically to determine R_s for given flow rate (Ca_p), orientation (ϕ, γ), Bo and plug length (L_0). The first term in Equation (3.21) represents the flow (viscous) effects, the second and third terms represent the gravity effect and the last term expresses the moving contact line effects at the front menisci. All the theoretical curves for LB-400X are plotted with the static contact angle α_0 fixed at 6.4º, while for glycerin, α_0 =56.3º.

When a plug is introduced into one of the daughter tubes as a blockage, there is an additional pressure drop in that daughter: viscous drag within the blockage and capillary jump across two menisci of the plug blockage including the new trailing film of the moving blockage. We assume that the blockage remains stationary until the parent plug begins to split and then moves at the same speed as the liquid entering that branch. While in the experiments, it was observed that the blockages start moving before the plug starts to split, which may contribute for the discrepancy of the theory and experiments. If the length of the blockage at any time is L_b and its flow rate is Q_b, the pressure drop across it is equal to

$$\Delta P_{BLK} = \frac{2\sigma}{a_2 - h_2} - \frac{2\sigma}{a_2}\cos\alpha_d + \frac{8\mu Q_b L_b}{\pi a_2^4} \pm \rho g L_b \sin\theta\sin\phi - \rho g L_b \cos\theta\sin\gamma, \tag{3.22}$$

where the positive and negative signs in ± refer to the upper and lower daughters respectively. Since the blockage moves the same distance as the length of the bifurcating plug entering that daughter, conservation of mass requires that L_b and the known initial blockage length L_{b0} are related as

$$\pi a_i^2 L_b = \pi a_i^2 L_{b0} - \pi\left(a_i^2 - \left(a_i - h_i\right)^2\right) L_i, \tag{3.23}$$

where $i = 2$ if the blockage is in the upper daughter and $i = 3$ if it is in the lower daughter. The trailing film thickness h_i is related to the local capillary number by (3.8). The pressure drop in Eqns. (3.19) or (3.20) is modified by adding this contribution and the following equations are obtained for blockages in the lower (3.24) and upper (3.25) daughters respectively:

$$\begin{aligned} &8\left(\frac{a_1}{a_2}\right)^4 Ca_p(1-\frac{h}{a_1})^2\left((R_s-1)-\frac{L_b}{L_3}\frac{1}{R_s+1}\right)+Bo\,(R_s+1+\frac{L_b}{L_3})\sin\theta\sin\phi \\ &-Bo(R_s-1-\frac{L_b}{L_3})\cos\theta\sin\gamma-\frac{2a_1^2}{a_2 L_3}\left[(1-\cos\alpha_0)-(1+\cos\alpha_0)\left(2Ca_2^{1/2}-4Ca_3^{1/2}\right)\right]=0 \end{aligned} \tag{3.24}$$

$$\begin{aligned} &8\left(\frac{a_1}{a_2}\right)^4 Ca_p(1-\frac{h}{a_1})^2\left((R_s-1)+\frac{L_b}{L_3}\frac{R_s}{R_s+1}\right)+Bo\left(R_s+\frac{L_b}{L_3}+1\right)\sin\theta\sin\phi \\ &-Bo\left(R_s+\frac{L_b}{L_3}-1\right)\cos\theta\sin\gamma+\frac{2a_1^2}{a_2 L_3}\left[(1-\cos\alpha_0)+(1+\cos\alpha_0)\left(4Ca_2^{1/2}-2Ca_3^{1/2}\right)\right]=0 \end{aligned} \tag{3.25}$$

3.3.2 High Re regime

Since Ca_p is very small and Re_p is very large, the motion of the plug when the plug starts splitting and enters the daughter tubes is considered as an entrance flow. The pressure-flow relation within pulmonary airways has been investigated numerically [19, 20] and experimentally [21, 22]. And the pressure-flow relationship in a single pulmonary bifurcation was also investigated experimentally for expiratory flow [23]. However, those studies were single phase flow and did not provide any information for the pressure drop of multiphase flow in an airway bifurcation model. In this section, a theoretical model was developed in finite Reynolds number regime to predict the experimental results and further understand the two phase fluid mechanics in the plug splitting process. The expressions for R_s are derived by a calculation of pressure drops and mass balance

between parent and daughter tubes using entrance flow theory.

The trailing film thickness is neglected due to the high Re_p and low Ca_p. From the mass balance, we can have the daughter plug length to be

$$L_2 = \left(\frac{a_1}{a_2}\right)^2 \frac{R_s}{R_s+1} L_0, \quad L_3 = \left(\frac{a_1}{a_2}\right)^2 \frac{1}{R_s+1} L_0 \tag{3.26}$$

where L_0 is the initial plug length in the parent tube before the front meniscus reaches the bifurcation and Re_p is the Reynolds number based on the parent plug speed U_p, which is same as the mean plug speed $\overline{U}_1$ here. The plug length in the parent tube be $L_1 < L_0$ when the plug has partially entered the daughter tubes, as shown in Figure 3.5.

The inertia effect is dominant (Re_p is high), so it is assumed that the plug motion into the daughter tubes is entrance flow. By applying an energy balance on the plug flow in the upper daughter tube

$$\begin{aligned} \int_{A_{1+}} pu\, dA - \int_{A_2} pu\, dA = & \int_{A_2} \left(\frac{1}{2}\rho q^2 + \rho g x_2 \left(\sin\theta\sin\phi - \cos\theta\sin\gamma\right)\right) u\, dA \\ & - \int_{A_{1+}} \left(\frac{1}{2}\rho q^2 + \rho g x_1 \left(\sin\theta\sin\phi - \cos\theta\sin\gamma\right)\right) u\, dA + \Phi_2 \end{aligned} \tag{3.27}$$

A_{1+} is the cross sectional area of the bifurcation region where flow goes to the upper daughter and A_2 is the distal cross section area (front meniscus) of the plug in the upper daughter tube. The mass conserves from A_{1+} to A_2, i.e. $\int_{A_{1+}} u_1\, dA = \int_{A_2} u_2\, dA$. The left hand side shows the net work of pressure force between cross section 1 and 2. The first two terms in the right-hand side represent the net gains of the kinetic energy. Φ_2 is the total frictional dissipation rate in the region between section 1 and 2. p and u are the pressure and velocity profile in one cross section. q is the magnitude of the velocity u. x_1 and x_2 are the axial positions of the two cross sections A_1 and A_2.

The flow averaged pressure and velocity square is defined as

$$\pi_i = \frac{1}{Q_i}\int p_i u\, dA, \quad \hat{q_i^2} = \frac{1}{Q_i}\int q_i^2 u\, dA \tag{3.28}$$

Dividing Eqn. (3.27) by Q_2 and using Eqn.(3.28), the pressure drop can be written for the upper daughter tube

$$\pi_0 - \pi_2 = \frac{1}{2}\rho\left(\hat{q}_2^2 - \hat{q}_1^2\right) + \rho g L_2\left(\sin\theta\sin\phi - \cos\theta\sin\gamma\right) + \frac{\Phi_2}{Q_2} \tag{3.29}$$

Similarly, in the lower daughter tube

$$\pi_0 - \pi_3 = \frac{1}{2}\rho\left(\hat{q}_3^2 - \hat{q}_1^2\right) - \rho g L_3\left(\sin\theta\sin\phi + \cos\theta\sin\gamma\right) + \frac{\Phi_3}{Q_3} \tag{3.30}$$

where π_0 is the plug pressure in the bifurcation region, and π_2 and π_3 is the end downstream pressure of the plug in the upper and lower daughter tube as shown in Figure 3.14. Since the capillary number is very small in this paper and on the interface ReCa<1 and Ca<<1, which means the surface tension instead of inertia dominates the pressure drop across the interface from the interface stress balance conditions. Thus, at the air-liquid-solid interfaces in the daughter tubes, the pressure drops are approximated as

$$\pi_2 - P_2 = -\frac{2\sigma}{a_2}, \quad \pi_3 - P_3 = -\frac{2\sigma}{a_2} \tag{3.31}$$

Assume the inlet velocity at A_1 into the daughter tubes is uniform and the front menisci speed of the plug at downstream ends A_2 and A_3 in daughter tube is also uniform. Thus, we have

$$\hat{q}_1^2 = \overline{U}_1^2, \quad \hat{q}_2^2 = \overline{U}_2^2, \quad \hat{q}_3^2 = \overline{U}_3^2 \tag{3.32}$$

Previous studies have shown that the frictional pressure drop ΔP_v, normalized by the Poiseuille pressure drop ΔP_P in the same condition, $\frac{\Delta P_v}{\Delta P_P}$ is proportional to $\mathrm{Re}^{1/2}$, such as $\frac{\Delta P_v}{\Delta P_P} = 0.556 + 0.06\,\mathrm{Re}^{\frac{1}{2}}$ in [23]. We then assume the frictional pressure drop $\frac{\Phi}{Q}$ in our model to have similar nonlinear relationship with the plug velocities in both upper and lower daughter tubes are

$$\frac{\Phi_2}{Q_2} = \alpha \frac{(\rho \mu L_2)^{\frac{1}{2}}}{a_2} \overline{U}_2^{\frac{3}{2}} + \beta \frac{8\mu \overline{U}_2 L_2}{a_2^2} \tag{3.33}$$

$$\frac{\Phi_3}{Q_3} = \alpha \frac{(\rho \mu L_3)^{\frac{1}{2}}}{a_2} \overline{U}_3^{\frac{3}{2}} + \beta \frac{8\mu \overline{U}_3 L_3}{a_2^2} \tag{3.34}$$

Therefore, the total pressure drops in the daughter tubes are:

$$\pi_0 - P_2 = \frac{1}{2}\rho\left(\overline{U}_2^2 - \overline{U}_1^2\right) + \rho g L_2 \left(\sin\theta \sin\phi - \cos\theta \sin\gamma\right) + \alpha \frac{(\rho \mu L_2)^{\frac{1}{2}}}{a_2} \overline{U}_2^{\frac{3}{2}} + \beta \frac{8\mu \overline{U}_2 L_2}{a_2^2} - \frac{2\sigma}{a_2} \tag{3.35}$$

$$\pi_0 - P_3 = \frac{1}{2}\rho\left(\overline{U}_3^2 - \overline{U}_1^2\right) - \rho g L_3 \left(\sin\theta \sin\phi + \cos\theta \sin\gamma\right) + \alpha \frac{(\rho \mu L_3)^{\frac{1}{2}}}{a_2} \overline{U}_3^{\frac{3}{2}} + \beta \frac{8\mu \overline{U}_3 L_3}{a_2^2} - \frac{2\sigma}{a_2} \tag{3.36}$$

Equaling (3.35) and (3.36), and substituting (3.3) - (3.5) and (3.26), an equation of R_s as the function of the other parameters is obtained:

$$R_s = 1 - \frac{2\rho g L_1 \sin\theta \sin\phi}{\frac{A_1}{A_2}\frac{\mu^2}{2\rho a_1^2}\mathrm{Re}^2 + \alpha \frac{\mu^2}{\rho a_1 a_2}\left(\frac{L_0}{a_1}\right)^{\frac{1}{2}} \frac{A_1}{A_2}\mathrm{Re}^{\frac{3}{2}} + \beta \frac{8\mu^2 L_0}{\rho a_1 a_2^2}\frac{A_1}{A_2}\mathrm{Re} + \rho g L_0 \left(\sin\theta \sin\phi - \cos\theta \sin\gamma\right)} \tag{3.37}$$

α and β are assumed to depend on gravity and the bifurcation geometry.

	ϕ=15°, γ=0°	ϕ=30°, γ=0°	ϕ=60°, γ=0°	ϕ=30°, γ=-15°	ϕ=30°, γ=15°
β	4.5228	4.6101	4.8158	3.2444	6.4286
LSE	0.06207	0.0080	0.0073	0.0061	0.0183

Table 3.2. Values of the fitting parameter, β at different orientations.

When the plug splits across the bifurcation into the curved daughter tubes with gravity acting, the velocity profiles are very complicated. The viscous dissipation may depend on the velocity profiles in the boundary layers or flow rates in the daughter tubes, which is different for different gravitational conditions. The experimental data is then fitted for each orientation ϕ and γ with no plug blockages using lease-square method on Eqn.(3.37). The fitting parameter α is found to be 0 for all cases at best fitting and the values of fitting parameter β are shown in Table 3.2, the range of which is between 3.24

and 6.43. The least square error (LSE), as the minimal sum of the deviation squared, is between 0.061 and 0.0682. Thus, in this study with plugs moving in the bifurcation, the frictional pressure drop is shown to be proportional to Re in stead of $Re^{3/2}$ for 2<Re<400. Results show that β slightly increases with increasing roll angle ϕ from 15° to 60°, while β has a large increase when γ increases from -15° to 15°.

With α=0 in Eqn.(3.37), we can get an explicit solution for critical Re, below which R_s=0:

$$\mathrm{Re}_c = -\beta \frac{4\mu^2 L_0}{\rho a_1 a_2^{\,2}} \frac{A_1}{A_2} + \frac{\mu}{2} \frac{A_1}{A_2} \sqrt{\frac{64\beta^2 \mu^2 L_0^2}{\rho^2 a_1^{\,2} a_2^{\,4}} + 2\rho g a_2^{\,2} L_0 \left(\sin\theta \sin\phi + \cos\theta \sin\gamma\right)} \quad (3.38)$$

It is found that Re_c decreases with increasing β at given orientations while increases with increasing ϕ and γ from this equation.

3.4. Experimental Results

In the experiments at low Re regime, the plug length instilled into the parent tube is L_p^*=1.5 ± 0.1cm and the blockage length L_b^*=0.7 ± 0.1cm. In the high Re experiments, the plug length in the parent tube is L_p^*=2.0 ± 0.1cm and the blockage length L_b^*=0.5 ± 0.1cm.

3.4.1 Low Re Regime

Effect of changing ϕ

The pitch angle was fixed at γ = 0º and experiments were performed for three values of the roll angle, ϕ = 15º, 30º, 60º, and a number of different speeds such that 0.001 < Ca_p < 0.11 and 0.001< Re_p < 0.03. In Fig. 3.6 the symbols show the experimental results for the mean values of R_s plotted against Ca_p for different ϕ. The bi-directional bars on each experimental point represent the standard error. In all cases a larger fraction of the plug liquid entered the lower daughter, A, than the upper daughter, B, after bifurcation and so R_s < 1. Note that for each ϕ there is a critical value of the capillary number, $Ca_p = Ca_c$ below which $R_s = 0$, i.e. no liquid enters the upper daughter. Thus a minimum speed (pressure) is needed for the liquid to overcome gravity and enter the

upper daughter after bifurcation. For $Ca_p > Ca_c$, R_s increases with Ca_p and the slope of R_s – Ca_p curve decreases. In contrast, results for the iso-gravitational case [2] ($\phi = \gamma = 0^o$) showed that $R_s \approx 1$ for all Ca_p and did not indicate the existence of a critical capillary number. As ϕ increases, Fig. 3.6 indicates that Ca_c increases and R_s decreases at a given $Ca_p > Ca_c$. These observations are consistent with the increasing gravitational asymmetry between the two daughters.

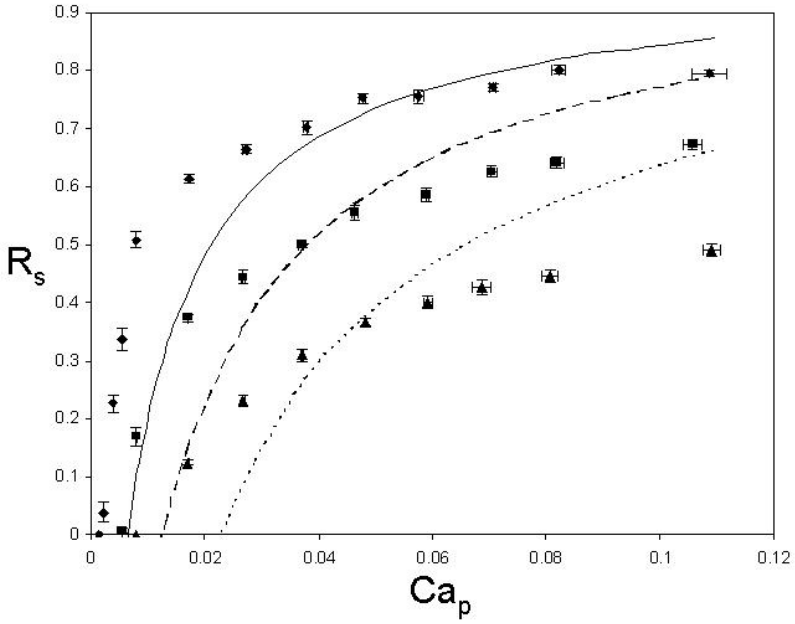

Figure 3.6 Splitting ratio R_s vs. Ca_p for γ=0º and different ϕ using LB-400-X oil. ϕ=15º: ◆(exps), ——— (theory); ϕ=30º: ■(exps), – – –(theory); ϕ=60º:▲(exps), ····· (theory).

Effect of changing γ

Experiments were performed for four values of the pitch angle γ =-15º, 0º, 15º, 30º with the roll angle fixed at $\phi = 30^o$ and 0.001< Ca_p <0.1. Experiments with $\gamma \neq 0^o$ and $\phi = 0^o$ were performed, and it is found that $R_s \approx 1$ with $\phi = 0^o$. To study the effect of pitch angle, we studied the case with non-zero roll angle and let $\phi = 30^o$. Results are plotted in Fig. 3.7 with the symbols representing experimental results. When γ =-15º, $R_s > 0$ for all Ca_p chosen. Critical capillary numbers Ca_c, that increase with γ, were found for $\gamma > 0^o$. R_s decreases with γ for a given $Ca_p > Ca_c$. However, when $Ca_p > 0.1$, R_s seems to asymptote to a value ~ 0.7 independent of γ. These results indicate that the effect of gravity in axial

direction is more important at low speeds than high speeds. At low speeds, the flow contribution to the pressure drop $P_1 - P_a$ is small and the hydrostatic pressure due to axial gravity dominates. Since this component varies with γ, R_s is a function of γ at small Ca_p. At high speeds, the flow contribution dominates the pressure drop and thus changing γ has only a small effect on R_s. For $\gamma > 30^o$ or $\gamma \leq -30^o$ it was not possible to form a stable plug in the parent tube and the liquid drained as a film along the bottom of the parent tube.

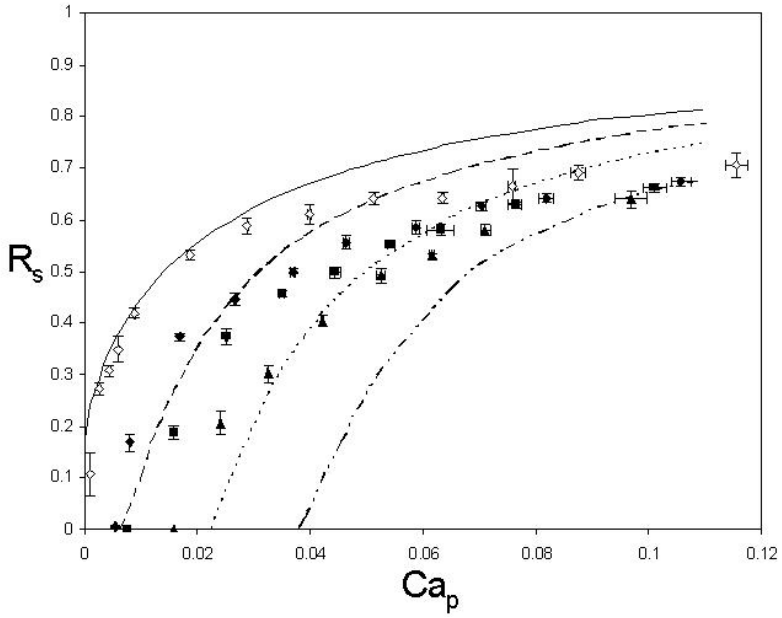

Figure 3.7 R_s vs. Ca_p for ϕ=30º and different γ using LB-400-X oil. γ=-15º: ◇ (exps), ——— (theory); γ=0º: ◆(exps), – – –(theory); γ=15º: ■(exps), ·····(theory); γ=30º:▲ (exps), —·—·—(theory).

Effect of blockages in the daughter tubes

Experiments were performed with a liquid plug introduced as a blockage into one of the daughter tubes and Ca_p and R_s were measured. Experiments were performed separately for blockages in the upper and lower daughters. The length of the blockages is $L_b^* = 0.7 \pm 0.1$cm. Experimental results are plotted as symbols shown in Fig. 3.8a-c for the orientations $\phi = 15^o, 30^o, 60^o$; $\gamma = 0^o$. Data from the unblocked experiments of Fig. 3.6 are included for comparison. In the unblocked case, more liquid enters the lower daughter which is gravity preferred. The presence of a blockage in one of the daughter

tubes introduces an additional asymmetry, which can counteract or enhance the gravitational asymmetry.

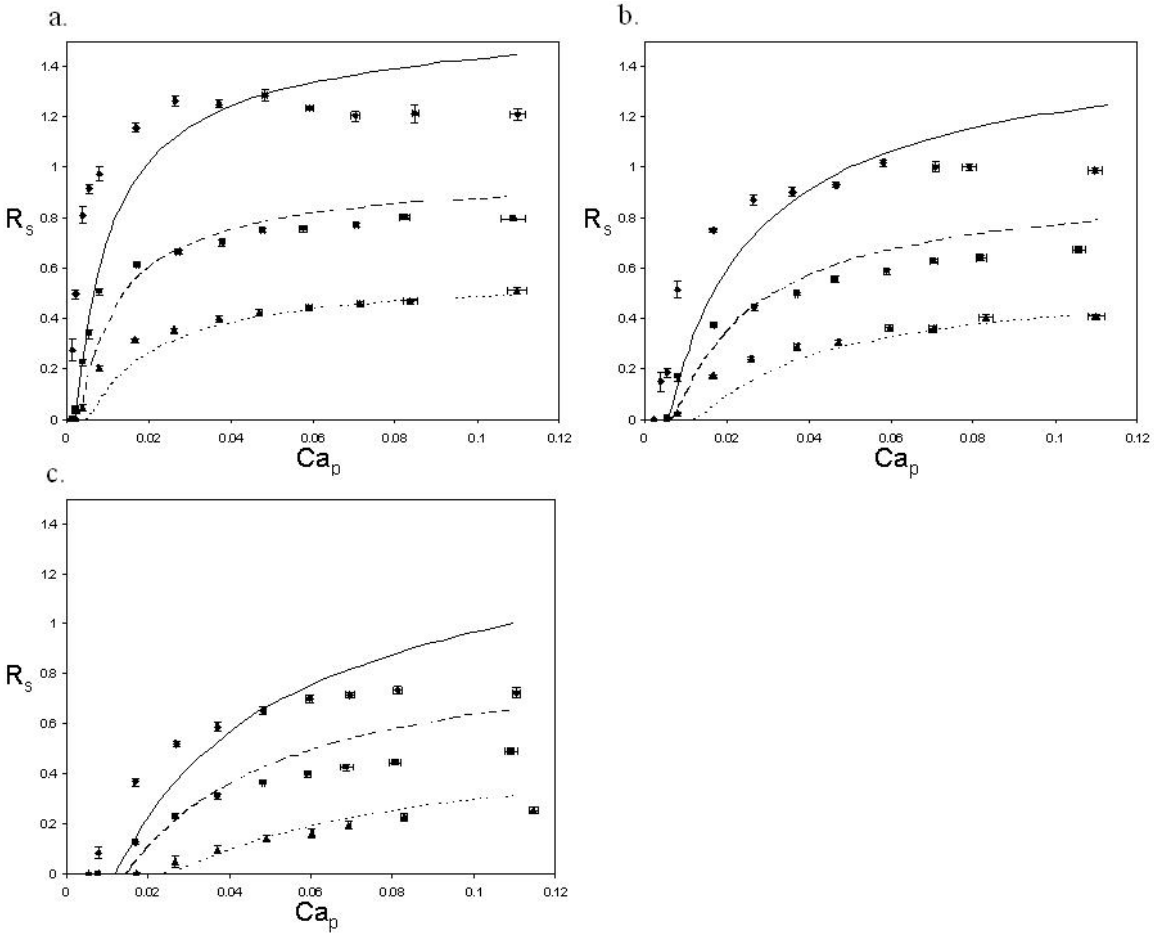

Figure.3.8 R_s vs. Ca_p for γ=0º and different blockage conditions with a pitch angle γ=0º and a roll angle of (a) ϕ=15º, (b) ϕ=30º, and (c) ϕ=60º using LB-400-X oil. Blockage in lower daughter:◆(exps), ——(theory); No blockage:■(exps), − − −(theory); Blockage in upper daughter: ▲ (exps), ····· (theory).

The figures (Fig. 3.8a-c) show that a blockage in the lower daughter tends to oppose the effect of gravity and results in larger R_s. In fact, this effect can overcome gravity and cause more liquid to enter the upper daughter than the lower daughter, leading to R_s values as high as 1.26 in Fig. 3.8a (ϕ = 15º). The same effect is seen in Fig. 3.8b and c for the larger roll angles (ϕ=30º, 60º), but R_s values are smaller due to the greater effect of gravity in these more asymmetric orientations. In contrast blockages in the upper daughter accentuate the gravitational asymmetry and lead to smaller values of R_s

compared to the unblocked case. These results are consistent with [2] who found that more liquid tends to enter the unblocked daughter in the iso-gravitational case.

The effect of the blockages can be quite significant. A blockage in the lower daughter reduces Ca_c and at $Ca_p < 0.03$, a blockage in the lower daughter can increase R_s by 200% to 1000% while at $Ca_p > 0.03$, R_s increases by 50%-100% compared to the unblocked (Fig. 3.8a-c). In contrast, a blockage in the upper daughter increases Ca_c and R_s can decrease by 40%-80% at $Ca_p > 0.02$ while by 200% to 600% at $Ca_p < 0.02$. These effects become more noticeable as ϕ is increased from 15º to 60º. Another interesting observation is the presence of maxima in the $R_s - Ca_p$ curves in Fig. 3.8a and b when the lower daughter is blocked. The maximum is most noticeable at the smaller roll angle, $\phi =$ 15º (Fig. 3.8a), but disappears when $\phi =$ 60º (Fig. 3.8c). In some clinical studies, a pre-treatment as a blockage in nearby airway branches can be introduced, which may be effective to control the liquid delivery to a targeted position in the lung.

Effect of Bo

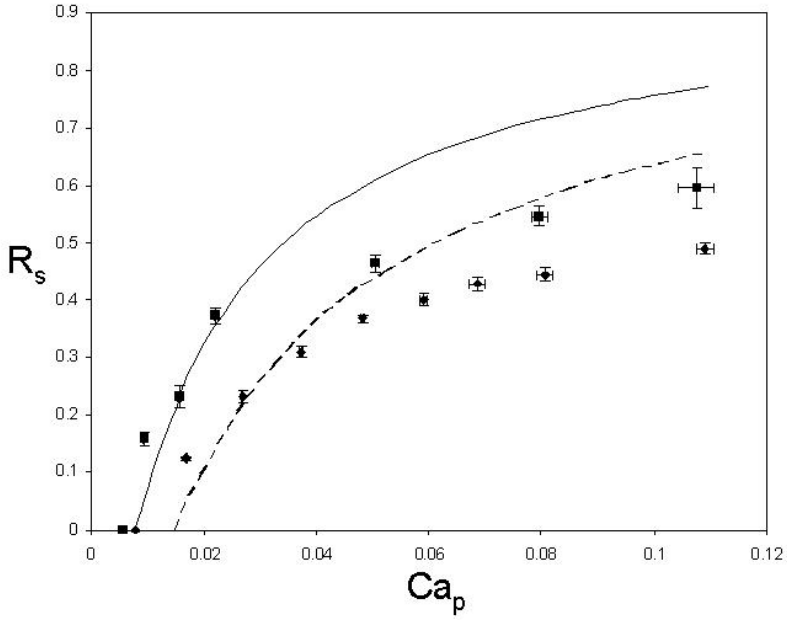

Figure 3.9 R_s vs. Ca_p at ϕ=60º, γ=0º for different Bo. Glycerin Bo=0.78: ■ (exps), —— (theory); LB-400-X Bo=1.26: ◆ (exps), – – – (theory).

Two different liquids, LB-400-X oil (Bo = 1.26) and glycerin (Bo = 0.78), were used

to study the effect of changing *Bo* on R_s at $\phi = 60º$, $\gamma = 0º$. The static contact angle of LB-400X oil on polycarbonate plate is measured about 6.4º using video camera, consistent with [24] in which the static contact angle of silicone oil, with similar physical properties as LB-400X, on polycarbonate plate is 6.2º. The static contact angle of glycerin on polycarbonate plate is measured as 56.3º. We expect that the difference in R_s is mainly due to the difference in Bo not the variation of static contact angle α_0 since it is predicted in Section of "Theoretical Analysis" that R_s varies within 5% when only changing static contact angle α_0 from 0° to 60°. Results are plotted as symbols in Fig. 3.9 and indicate that a 60% change in *Bo* leads to a 10 – 50% change in R_s for $0.007 < Ca_p < 0.14$. R_s is more sensitive to *Bo* at lower Ca_p which is because at low speeds gravity contribution to pressure drop is more important, therefore changing *Bo* leads to bigger changes in R_s.

3.4.2 High Re Regime

As Re_p is high, the inertia plays an important role in plug splitting, which makes the splitting ratio above 0 even at low Ca. The following experimental results present R_s vs. Re_p at different experimental conditions, in which Re_p is in the range of $2<Re_p<300$, while the capillary number is in a very small range of $2x10^{-5}<Ca_p<3x10^{-3}$. For convenience, Re_p is used as the characteristic speed in this regime. The symbols in the figures shown below represent the experimental data, while the lines represent the theoretical predictions from Section 3.3.2.

Effect of changing ϕ

To study the effect of roll angle on the plug splitting, experiments were performed with initial plug length L_0=2cm at different roll angle ϕ, fixed pitch angle γ, and a number of different speeds so that $5 < Re_p < 300$. Experimental results were found to be the same by flipping the bifurcation plates upside down, i.e. $\phi = \pm |\phi|$ at $\gamma = 0°$, which demonstrated the symmetry in our bifurcation. And at $\phi = 90°$ and $\gamma = 0°$, R_s is found to be approximately 0 in the range of Re_p we investigated since the gravity effect is very large.

Thus in Figure 3.10 the symbols show the experimental results for mean values of R_s plotted against Re_p for ϕ=15°, 30°, 60° and γ=0°. The standard error is shown by the bi-directional bars on each experimental point. Similar to the experiments in Stokes flow regime, a critical Reynolds number, $Re_p=Re_c$ is found to exist for each case below which $R_s=0$, i.e. no liquid enters the upper daughter tube. Generally a minimum speed (pressure) is required for the liquid to overcome gravity and enter the upper daughter tube after the bifurcation region. Re_c increases and R_s decreases with increasing ϕ at a given $Re_p>Re_c$. For a given ϕ, R_s increases with Re_p. The results show more homogenous plug splitting as the plug speed increased or the gravitational roll angle ϕ decreased. From the monotonic increase of R_s vs. Re_p, we expect that R_s will approach 1 when Re_p goes to infinity for the increasing trend of R_s with Re_p if there is no plug rupture. Though the plug speed investigated has a limited range in our experiments due to the limitation of the pump, we expect our results provide most features of the experiments.

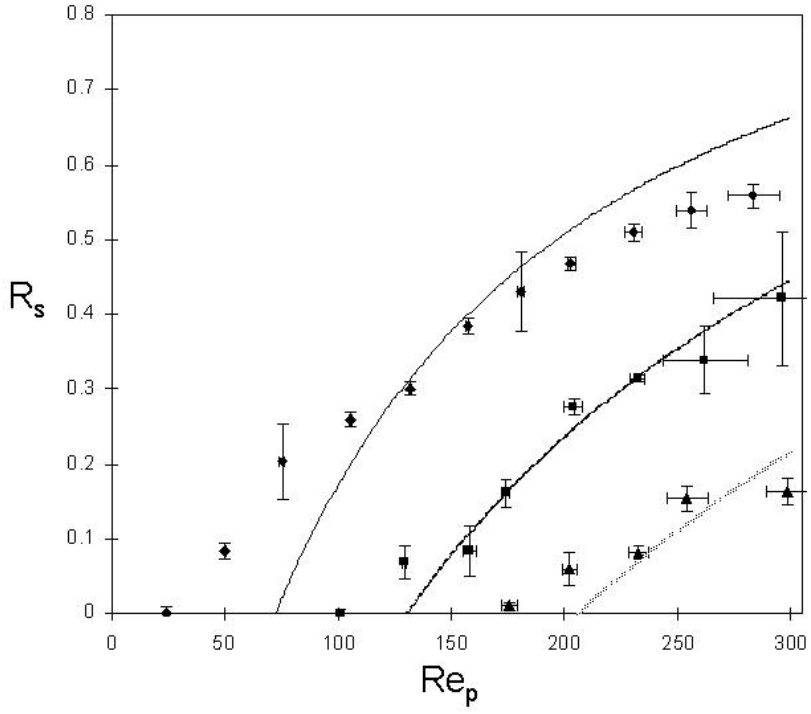

Figure 3.10 R_s vs. Re_p for γ=0º and different ϕ using LB-400-X oil. ϕ=15º: ◆(exps), —— (theory); ϕ=30º: ■(exps), – – –(theory); ϕ=60º:▲(exps), ····· (theory).

Effect of changing γ

Experiments were performed with initial plug length L_0=2cm for three values of pitch angle γ=-15°, 0°, 15°; roll angle ϕ=30°; and Re_p was in the range of $2<Re_p<300$. Results are plotted in Figure 3.11 with the symbols representing experimental results. When γ=-15°, no critical Reynolds number Re_c is found for the range of Re_p in the experiments. When γ>0°, Re_c increases with γ. R_s decreases with γ for a given $Re_p>Re_c$ while R_s increases with Re_p. These results also provide evidence that increasing speed results in more homogenous splitting, moreover, decreasing pitch angle γ causes more homogenous splitting too. As we discussed in our previous paper, when γ is above around 30° or below -30°, the plug flow freely along the tube due to the gravity without air pumping, which make it very hard for the accurate measurements. We expect three values of pitch angle will provide enough information on the trend of R_s with γ.

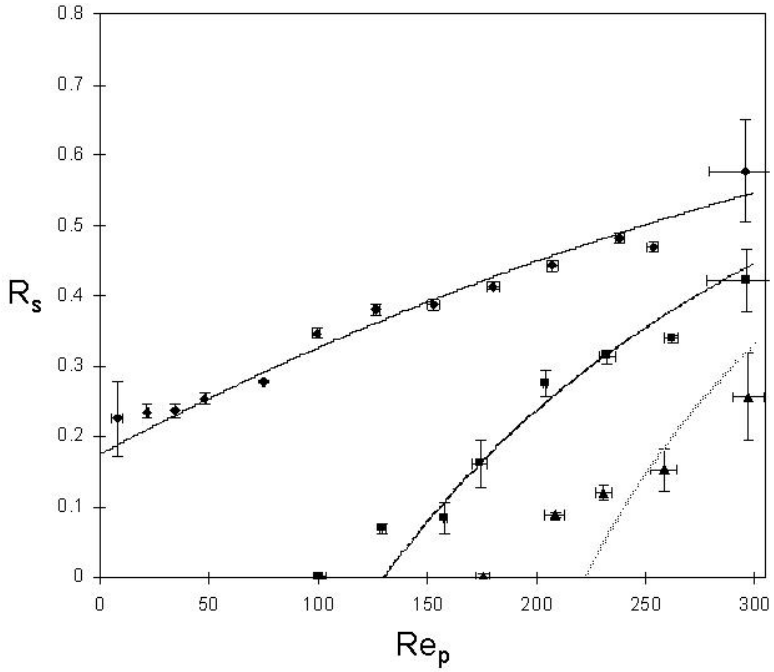

Figure 3.11 R_s vs. Re_p for ϕ=30º and different γ using LB-400-X oil. γ=-15º:◆(exps), —— (theory); γ=0º:■(exps), – – –(theory); γ=15º:▲(exps), ·····(theory).

Effect of plug length

Two different initial plug length (L_0=1.0cm and L_0=2.0cm) were used to test the

effect of plug length on plug splitting at ϕ=15°, γ=0° and 2<Re_p<300. Results are plotted as symbols in Figure 3.12 and indicate that doubling the initial plug length L_0 leads up to 40% decreases in R_s for 20< Re_p<300, which means that shorter plug result in more homogeneous splitting in finite Re regime. The results show an opposite trend for LB400X, which showed that R_s increased with increasing the initial plug length when inertia effect was negligible.

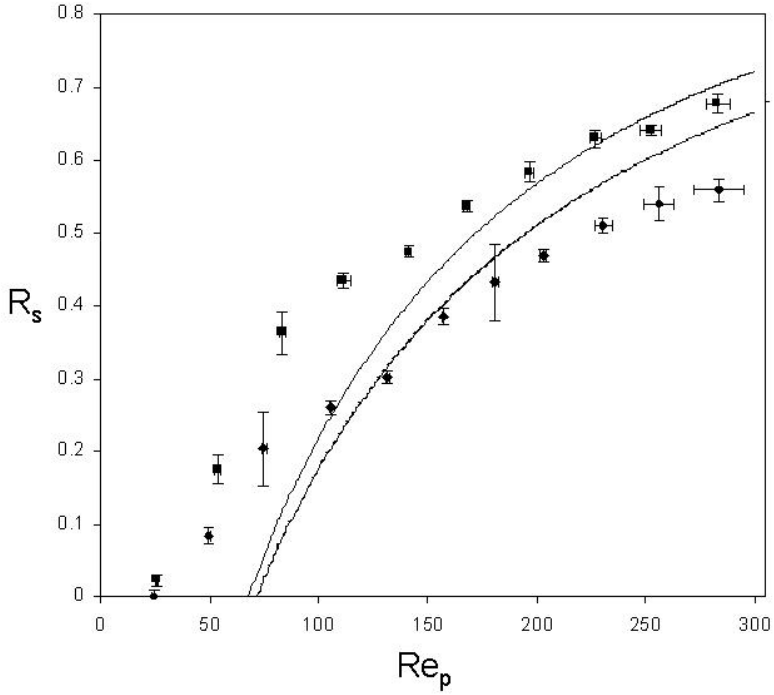

Fig. 3.12 Experimental results of effect of parent plug volume on splitting ratio, R_s, vs. Re_p for deionized distilled water at ϕ=15º, γ=0º. L_0=1cm (L_0/a_1=5): ■ (exp.), —— (theory); L_0=2cm (L_0/a_1=10): ◆ (exp.), − − − (theory).

Effects of plug blockages

Experiments were performed with a liquid plug introduced as a blockage into one of the downstream daughter tubes in our bifurcation model. The initial length of the blockages L_{b0}=0.5cm. As a plug blockage is introduced into the upper daughter tube, the gravitational asymmetry is enhanced. R_s is approximately 0 and no plug splitting occurs at the bifurcation region for three cases of orientation: ϕ=15°, 30°, 60° with γ=0° at 2<Re_p<300, which means all liquids enter the lower unblocked daughter tube. These

results are quite different with those at Stokes flow regime in which R_s could increase up to 0.5 with upper daughter blockage for LB-400X at ϕ=15°, 30°, 60° and γ=0°.

As a plug blockage exists in the lower daughter tube, experimental data at ϕ=15°, 30°, 60° and γ=0° are shown in Figure 3.13. The lower plug blockage acts adversely to the gravitational asymmetry. Our results show that as Re_p is small, R_s is very large and can be as high as 18; while it decreases as Re_p increases at ϕ=15°. At ϕ=30°, it seems that R_s stays in the range of $5<R_s<6.5$. At ϕ=60°, Re_c is found, below which R_s=0, and R_s increases with Re_p at $Re_p<50$, then asymptotes to a finite value around 4. R_s is also shown to decrease with increasing ϕ for any fixed Re_p at $2<Re_p<300$.

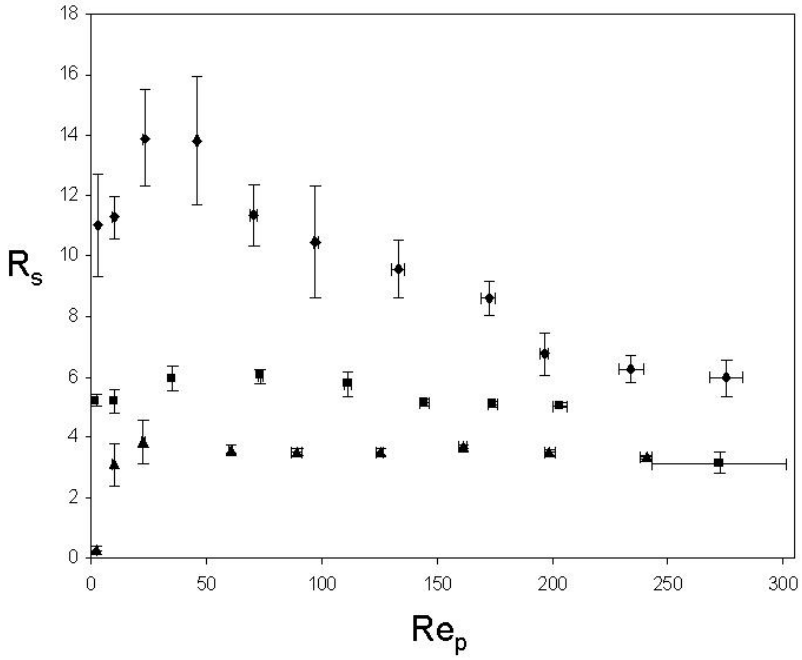

Figure 3.13 Experimental results of R_s vs. Re_p with the presence of lower plug blockage for γ=0º and different ϕ using deionized distilled water. ◆: ϕ=15º; ■: ϕ=30º; ▲: ϕ=60º.

These phenomena may be because of the unsteady effect when the plug splits. The existence of the inertia requires a large initial force to move the plug blockage. When Re_p is very small, at small gravity effect, i.e. ϕ=15° and 30° , the blockage effects dominate and most of liquid enters the unblocked daughter tube; while at large ϕ, i.e. ϕ=60°, the gravity effect is dominant, more liquid enters the lower daughter tube, which causes a small R_s. As Re_p increases, the inertia effect starts to play an important role and the

gravity effect diminishes, thus the plug tends to split more homogeneously and R_s-Re_p curves for three ϕ asymptote to one curve when Re_p keeps increasing. We expect R_s will approximate to a finite value, which may depend on the plug blockage length, as Re_p goes to infinity.

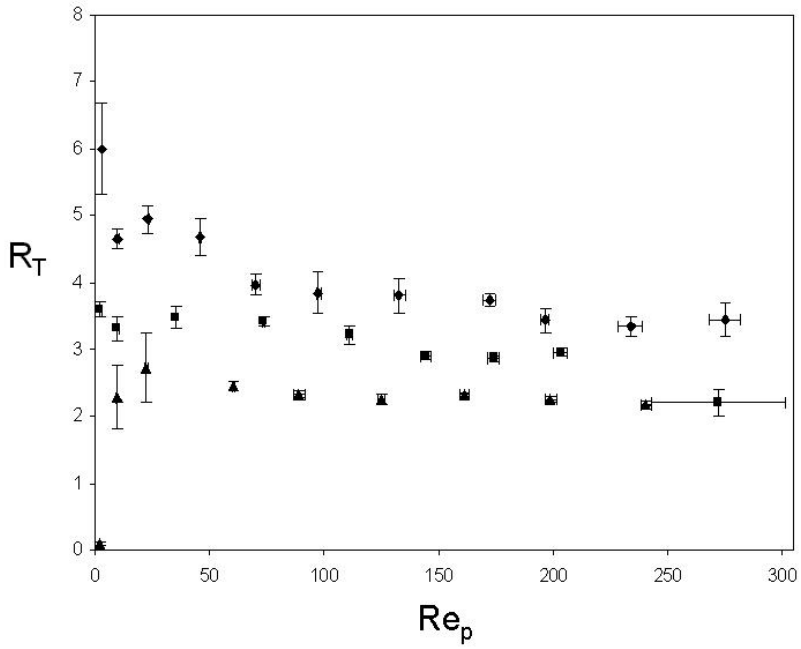

Figure 3.14 Experimental results of the total liquid ratio, R_T vs. Re_p with the presence of the lower plug blockage for γ=0º and different ϕ using deionized distilled water. ◆: ϕ=15º; ■: ϕ=30º; ▲: ϕ=60º.

A total mass ratio, R_T, is defined as the ratio of the total liquid volume in the upper daughter tube to that in the lower one including the blockage mass. Figure 3.14 shows the experimental data for R_T vs. Re_p at $2<Re_p<300$ with a lower blockage at ϕ=15°, 30°, 60° and γ=0°. R_T decreases with increasing ϕ. At ϕ=15°, 30°, it seems that R_T decreases monotonically with increasing Re_p, while at ϕ=60°, R_T increases to a steady value with increasing Re_p. The total mass tends to distribute more homogeneously when Re_p is larger, i.e. R_T is expected to approach to a finite value for all three curves, which is expected to be slightly greater than 1 as Re_p goes to infinity.

3.5 Discussion

3.5.1 Low Re Regime

The simplified theoretical model qualitatively captures the features of the experimental data. Fig. 3.6 – 7 show a comparison of the experimental data (symbols) with theoretical predictions for R_s (lines) for different ϕ and γ. The theory captures the trends of the experimental data: 1) the existence of a critical capillary number, 2) the increase of R_s with Ca_p and its decreasing slope, and 3) the decrease of R_s with increasing ϕ. When $\gamma = 0^o$, Fig.3.6 shows that there is qualitative agreement between the theory and experiments, which is promising given the simplifying assumptions of the theory. The agreement is better for smaller values of ϕ. At lower values of Ca_p, the theory underpredicts R_s, which leads to an overprediction of the critical capillary number. At higher values of Ca_p, R_s is overpredicted. Fig.3.7 shows R_s as a function of Ca_p for different values of γ. For γ = -15º, the theory does not predict the existence of Ca_c, but agrees fairly well with experiments for $Ca_p < 0.04$. For other values of γ, the theory underpredicts R_s for small Ca_p, while for large Ca_p, the theory overpredicts R_s for all values of γ. The discrepancy between the theory and experiments increases with γ.

Fig.3.8a – c show comparisons of theory and experiments with the effect of blockages. The theory is more accurate when the upper daughter is blocked and for smaller values of ϕ. Also the theory is unable to predict the maxima in the experimental $R_s - Ca_p$ curve observed when the lower daughter is blocked.

Fig.3.9 compares theoretical and experimental results for different Bond numbers. It is seen that the theoretical results show bigger changes when Bo is varied than the experiments, but they agree qualitatively.

The discrepancies between theory and experiment are a result of approximations to the geometry of the model and the fluid dynamics in the theoretical analysis. The simplified theoretical model does not account for the transition in geometry from the bifurcating region of the parent tube to the daughter tubes. Pressure drops in the liquid were computed under the assumption of Poiseuille flow. While this assumption is accurate for a long plug in the parent tube [25], entrance and transient effects are likely to

be important when the bifurcating plug enters the daughter tubes. The unsteady effect in the motion of the plug is neglected in the theory, which may play a complicated role in the experiments especially when the daughter blockages are present. It was observed in the experiments that the blockages start moving before the parent plug splits and plug speeds entering the daughter tubes are not constant so that the ratio L_A/L_B changes over the course of plug splitting.

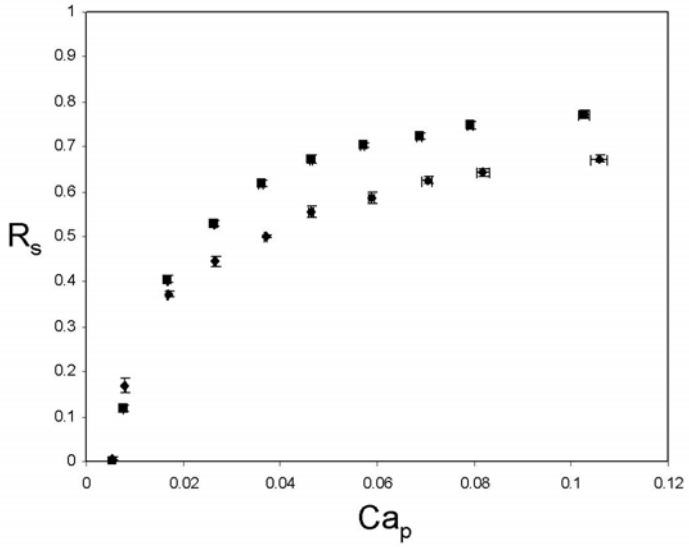

Figure 3.15 Experimental results of effect of parent plug volume on splitting ratio, R_s, and capillary number, Ca_p for LB-400-X oil at ϕ=30º, γ=0º. ■: L_0=3cm (L_0/a_1=15), ◆: L_0=1.5cm (L_0/a_1=7.5).

In order to study the effect of plug length on R_s, we performed a set of experiments by doubling the parent plug length to 3 cm. Results are shown in Figure 3.15. The critical capillary number was found to be unaffected by the plug length. For $Ca_p < 0.01$, doubling the plug length was found to decrease R_s by about 20%. For $Ca_p>0.01$, R_s for the longer plug was about 15% larger than the shorter plug. Since the variation in plug length in our experiments was small ($L_0 = 1.5 \pm 0.1$ cm), we do not expect significant effects on R_s from plug length effects. Larger *Ca* experiments in which the plugs entering the daughter branches are very short have a greater potential for error since small variations in measuring plug lengths can lead to large changes in R_s.

3.5.2 High Re Regime

Figure 3.10-3.11 show the comparison of experimental data (symbols) and theoretical results (line) for R_s with fitted β and $\alpha=0$ at different conditions of gravitational orientations ϕ and γ. β is found in the range of $3.24 \leq \beta \leq 6.43$ and shows a slight decrease with roll angle ϕ but increases with pitch angle γ. It is expected that the frictional dissipation may depend on the gravity since the flow rate and the velocity profile in the daughter tubes may be changed by gravity. The range of β shows our frictional pressure drop is much higher than the Poiseuille pressure drop, which is reasonable as we know that the Poiseuille flow has the minimum viscous dissipation. The roughness of the bifurcation tubes may also account for some pressure drop due to pure friction. In our experiments, the plug flow in the daughter tube is complicated since entrance effects may be important and the daughter tubes have curved geometries. All these will cause additional dissipation. With $\alpha=0$ and a small fluctuation of the parameter β, we expect our theory to predict the main features of the experiments: 1) the existence of a critical Reynolds number except the case $\gamma=-15°$; 2) the increases of R_s with Re_p; 3) the decreases of R_s with increasing ϕ and γ. In fact, even with $\alpha=\beta=0$, our theory can still predict the main features of the experiments, but cannot quantitatively agree with the experiments, which indicates that the inclusion of the viscous dissipation into the theory is essential for the quantitative agreements.

Figure 3.12 shows the comparison of the experiments and theory with $\alpha=0$ and $\beta = 4.52$ for different plug length at $\phi=15°$ and $\gamma=0°$. It qualitatively agrees with the experiments and predicted that R_s increases with decreasing the initial plug length L_0 and the difference of R_s for different L_0 is larger for larger speed. However, with $\beta = 4.52$, the theory under predicts the experimental data for shorter plug $L_0=1.0$cm, which indicates that β may also depend on the plug length, i.e. β may increase with decreasing plug length. These observations are consistent with our expectations: inertia increases the homogeneity of liquid distribution through one bifurcation and inertia may be more

important for shorter plugs because of more interactions between the front and rear menisci [25].

There are some assumptions in theoretical studies, which may cause discrepancies in certain degree to exist between the theory and experiments. The effects of bi-phase flow is neglected and the frictional viscous dissipation is assumed to have similar dependence with Re as one phase flow. The input velocity profiles to each daughter tubes are assumed to be the same: flat and uniform, which in fact maybe skewed to three dimensional profiles and maybe different for two daughters because of gravity effect. The inlet pressure to each daughter tube is assumed to be the same, while the actual pressure difference may exist on the inlets for two daughter tubes due to gravity or some other effects. The moving contact line force is neglected in the front meniscus since the Ca_p turns out very small, which is expected to have negligible effects. As R_s is very small, the flow rate in the upper daughter tube is very small, thus the flow in upper daughter may be close to Poiseuille flow while the flow in the lower daughter may be very complicated. The overestimated pressure drop in the upper daughter with our theory may cause the underestimated R_s and overestimated Re_c. When Re_p is very small, there should be a transition to Poiseuille flow, which, however, is not included in this theory. These assumptions in the theory may cause over-predicted Re_c and under-predicted R_s for small Re_p.

Experimental limitations. The present system contains certain physiological limitations. The fabrication of the bifurcation plates determined that our bifurcation systems have rigid walls and the bifurcation region is a sharp corner instead of a physiologically rounded corner, which may cause large difference for the pressure drop. The length of the parent plug is measured before the leading meniscus enters the central zone of the bifurcation to get the parent volume with the average velocity measured through two IR sensors. Care was taken so that the error from the liquid plug length is within 10%. Figure 3.12 shows that within 40% decrease of R_s with doubling the plug

length at ϕ=15° and γ=0°. Hence, it is expected that the error coming from the plug length is not important for R_s. Previous experiments have shown R_s depends weakly on the plug and blockage lengths [2].

The error for measuring R_s for high Re regime involves the IR measurement error as well as the error from the rounded plug meniscus. It includes: 1) the error from the IR detector size for recording the plug menisci. IR detector size is 1.5mm and its sensitive size is around 1mm, which cause the error for tracking the plug meniscus is around 1mm. 2) the error of the plug length measurement in daughter tubes. The daughter tube is curved and the plug does not have a fully steady motion when it splits into two daughter tubes. Thus the error exists on the plug velocity and length measurement in IR sensors. 3) the error from the non-uniform air flow. When Re_p is high, the air flow from the pump is not quite uniform in the tube cross section. Thus the meniscus shape, which may change by the velocity and gravity, will be affected and error will be present on the meniscus tracking. 4) the error from rounded meniscus. The signal of the meniscus is not exactly binary since the meniscus is a 3-D shape in the tube and its curvature is very complicated. As the detector senses the liquid absorption, the maximum difference of the absorption is recorded as the meniscus passes by.

Effect of inertia

For better understanding the effect of inertia on the plug splitting, additional experiments were performed at initial plug length L_0=2cm, roll angle ϕ=30° and pitch angle γ=0° with 60% glycerin ($2 < Re_p < 25$ and $0.0015 < Ca_p < 0.015$). The results are compared with those using deionized water ($70 < Re_p < 400$ and $0.0005 < Ca_p < 0.0028$) and lubrication oil LB-400X from previous section with $0.012 < Re_p < 0.17$ and $0.0045 < Ca_p < 0.065$ at the same gravitational conditions. The same characteristic speed, Ca_p is used in three fluids for better comparison. In Figure 3.16, the symbols show the experimental results for mean values of R_s plotted against Ca_p in log scale for three liquids. The standard error is shown by the bi-directional bars on the experimental points.

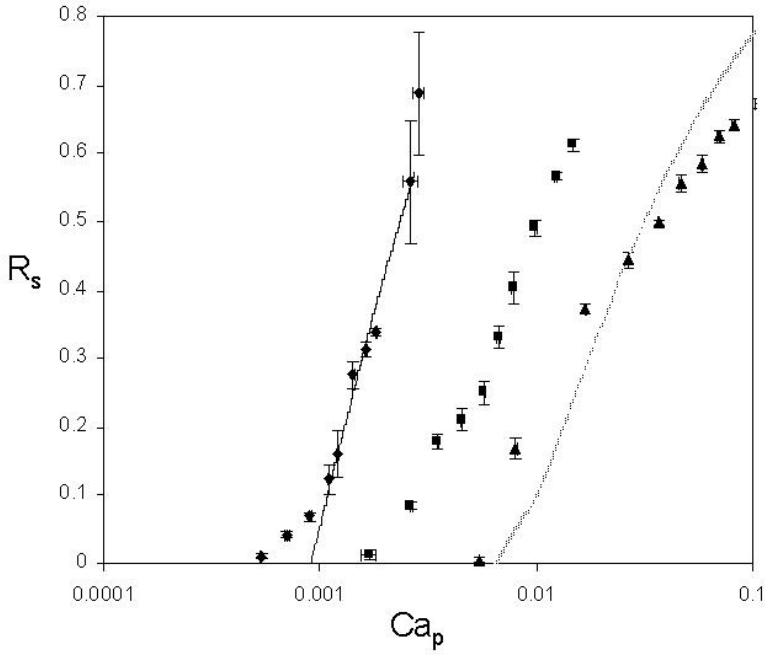

Figure 3.16 R_s vs. Ca_p for γ=0º and $\phi = 30$º with three liquid materials at different flow regimes. deionized distilled water: ◆(exp.), —— (theory); 60% glycerin: ■ (exp.); LB-400X: ▲ (exp.), ····· (theory).

The three sets of data have the similar trend: 1) a critical $Ca_p=Ca_c$, below which, $R_s=0$, 2) R_s increases with Ca_p. However, the curve shifts to the left when the liquid plug material changes from LB-400X to 60% glycerin, then to deionized water with the critical capillary number Ca_c=0.0045, 0.0015 and 0.0005 respectively. The viscosity of the liquid decreases around 150 times from LB-400X to the deionized water, which causes great decreases on Ca_p while great increases on Re_p from the right curve to the left. It is shown that for deionized water, R_s increases from 0 to 0.8 when $0.0005<Ca_p<0.0028$, in the range of which, however, R_s=0 for LB-400X. The bond number of these three liquids ranges from 1.26 to 0.54, which is not expected to have so much difference on R_s based on Fig. 3.9. The effect of plug length on R_s is expected to be small (L_0=2cm for water and glycerin, L_0=1.5cm for LB-400X). The main difference in these three experimental data is that Re_p is much higher for the left curve at O(100) than the right one at O(0.1). Thus, the inertia must play the most important role on R_s. With high Re_p, the plug can split more homogeneously even at small Ca_p. Using Re_p as the characteristic

speed brings more convenience for this set of experiments.

The two lines in Fig. 3.16 represent the theoretical prediction for the two sets of experimental data at different conditions. The previous theory for negligible inertia is used to predict the experimental data with LB-400X and the theory presented for finite Re regime is used to predict the experiments with water and glycerin. It is found that the present theory have a good prediction for the experimental data in high Re_p while have some discrepancy in low Re_p region. The Stokes flow theory under predicts the experimental data with glycerin and cannot predict the data with water, while the theory in finite Re regime over predicts the experimental data with glycerin and cannot predict those for LB-400X in negligible inertia. Thus, to predict the total liquid distribution in the lung, we can expect the theory presented for finite Re regime to be used for the plug distribution in large and central airways (airway generation below ~ 10), where the plug Reynolds number is above O(10), while the theory with negligible inertia at Stokes flow regime can be used for small airways (generation above around 10) to predict the liquid distribution. A combination theory may be needed to predict the liquid distribution in a bifurcation at the intermediate range of parameters.

3.6. Conclusion

This chapter studies the effects of gravity, inertia, and liquid blockages in downstream branches on liquid plug splitting through bench-top experiments and theoretical models. A critical speed is found below which the entire plug drains into the gravitationally favored daughter leading to a splitting ratio R_s=0. For speed greater than the critical value, R_s depend on the plug speed, the roll angle ϕ and pitch angle γ. R_s increases with plug speed at a given ϕ and γ while R_s decreases with increasing ϕ and γ at a given plug speed. At low Re regime: as the plug speed increases R_s approaches a limiting value, which decreases with ϕ, but seems to be independent of γ; higher Bond numbers enhance the effect of gravity and lead to lower splitting ratios; This effect was more significant at low speed, but less important at higher speed. A comparison study

with at high Re regime shows that inertia plays an important role in plug splitting using three different plug materials: inertia results in more homogeneous plug splitting and it has more effect on shorter plug: shorter plug volume leads to larger R_s with inertia. Experiments were also performed with a liquid blockage in one of the daughter tubes. The presence of a blockage in the lower, gravitationally favored daughter counteracts the effect of gravity and results in larger splitting ratios compared to the unblocked case. When the upper daughter is blocked gravitational asymmetry is enhanced which causes smaller values of R_s.

At high Re regime, R_s is found to be approximately 0 in the range of plug speed studied with a plug blockage existing in the upper daughter tube, and results show that R_s can be up to 18 with lower blockage for ϕ=15°, and decreases with further increasing plug speed. The total mass ratio, R_T, is found to monotonically decrease for small ϕ while increase with the plug speed for larger ϕ, and R_T decreases with increasing ϕ at a fixed plug speed investigated. Mathematical models are developed for both regimes. At low Re regime, the theory accounted for pressure drops across the tubes due to surface tension, gravity, viscosity and moving contact line effects was developed. Predicted values of R_s capture the experimental trends and agree qualitatively with the data over a range of parameters. At high Re regime, it accounts for the pressure drop across the daughter tubes due to inertia, viscous dissipation, gravity and surface tension effects. Fitting parameters are obtained for frictional pressure drop in daughter tubes, which is shown to depend on the gravitational effects. The predicted R_s capture most of the experimental features. Combining the theory in both regimes is expected to provide a good prediction for the total liquid distribution in the human lungs.

This study provides some insights into the physical mechanisms that affect liquid plug transport in airways and quantifies the effects of flow rate, gravitational orientation and downstream liquid blockages. It represents a first step towards the development of a rational strategy to achieve targeted liquid delivery by manipulating ventilation (flow)

rate, posture (gravitational orientation) and instillation methods that promote or deter liquid plug formation in pulmonary airways. The parameter range studied in this work is applicable from small airways where fluid velocity is relatively low to large airways where inertia plays an important role.

References

1. Fujii, H. and H. Nakae, *Effect of Gravity on Contact-Angle.* Philosophical Magazine a-Physics of Condensed Matter Structure Defects and Mechanical Properties, 1995. **72**(6): p. 1505-1512.
2. Cassidy, K.J., N. Gavriely, and J.B. Grotberg, *Liquid plug flow in straight and bifurcating tubes.* J. Biomech. Eng., 2001. **123**(6): p. 580-589.
3. Cassidy, K.J., et al., *Surfactant effects in model airway closure experiments.* Journal of Applied Physiology, 1999. **87**(1): p. 415-427.
4. Bogy, D.B., *Drop Formation in a Circular Liquid Jet.* Annual Review of Fluid Mechanics, 1979. **11**: p. 207-228.
5. Michael, D.H., *Meniscus Stability.* Annual Review of Fluid Mechanics, 1981. **13**: p. 189-215.
6. Gauglitz, P.A. and C.J. Radke, *The dynamics of liquid film breakup in constricted cylindrical capillaries.* Journal of Colloid and Interface Science, 1990. **134**: p. 14-40.
7. Hammond, P.S., *Nonlinear adjustment of a thin annular film of viscous fluid surrounding a thread of another within a circular pipe.* Journal of Fluid Mechanics, 1983. **137**: p. 363-384.
8. Howell, P.D., S.L. Waters, and J.B. Grotberg, *The propagation of a liquid bolus along a liquid-lined flexible tube.* Journal of Fluid Mechanics, 2000. **406**: p. 309-335.
9. Kamm, R.D. and R.C. Schroter, *Is airway closure caused by a thin liquid instability?* Respiration Physiology, 1989. **75**: p. 141-156.
10. Weibel, E.R., *Morphometry of the human lung*. 1963, New York: Academic Press. 151.
11. Heistracher, T. and W. Hofmann, *Physiologically realistic models of bronchial airway bifurcations.* Journal of Aerosol Science, 1995. **26**(3): p. 497-509.
12. Cassidy, K.J., *Liquid film dynamics in the pulmonary airways*, in *Department of Mechanical Engineering*. 1999, Northwestern University: Evanston, IL. p. 171.
13. Wolffenbuttel, B.M.A., et al., *Novel method for non-intrusive measurement of velocity and slug length in two- and three-phase slug flow in capillaries.* Measurement Science & Technology, 2002. **13**(10): p. 1540-1544.
14. Cassidy, K.J., et al., *A rat lung model of instilled liquid transport in the pulmonary airways.* Journal of Applied Physiology, 2001. **90**: p. 1955-1967.
15. Halpern, D., O.E. Jensen, and J.B. Grotberg, *A theoretical study of surfactant and liquid delivery into the lung.* Journal of Applied Physiology, 1998. **85**(1): p. 333-352.
16. Bracke, M., F. Devoeght, and P. Joos, *The Kinetics of Wetting - the Dynamic Contact-Angle.* Progress in Colloid and Interface Science, 1989. **79**: p. 142-149.
17. Jiang, T.S., S.G. Oh, and J.C. Slattery, *Correlation for Dynamic Contact-Angle.* Journal of Colloid and Interface Science, 1979. **69**(1): p. 74-77.

18. Hoffman, R.L., *Study of Advancing Interface .1. Interface Shape in Liquid-Gas Systems.* Journal of Colloid and Interface Science, 1975. **50**(2): p. 228-241.
19. Liu, Y., R.M.C. So, and C.H. Zhang, *Modeling the bifurcating flow in a human lung airway.* Journal of Biomechanics, 2002. **35**: p. 465-473.
20. Pedley, R.J. and R.D. Kamm, *Dynamics of Gas Flow and Pressure-Flow Relationships.* The Lung: Scientific Foundations, Chapter 5.1.2.2, R.G. Crystal, J.B.West et al., eds., Raven Press, Ltd., New York, 1991.
21. Pedley, R.J., R.C. Schroter, and M.F. Sudlow, *Flow and Pressure Drop in Systems of Repeatedly Branching Tubes.* Journal of Fluid Mechanics, 1971. **46**(MAR29): p. 365-&.
22. Pedley, T.J., *Pulmonary fluid dynamics.* Annual Review of Fluid Mechanics, 1977. **9**: p. 229-274.
23. Collins, J.M., et al., *The steady expiratory pressure-flow relation in a model pulmonary bifurcation.* Journal of Biomechanical Engineering, 1993. **115**(3): p. 299-305.
24. Kim, H.Y. and J.H. Chun, *The recoiling of liquid droplets upon collision with solid surfaces.* Physics of Fluids, 2001. **13**(3): p. 643-659.
25. Fujioka, H. and J.B. Grotberg, *Steady Propagation of a Liquid Plug In a 2-dimensional Channel.* J. Biomech. Eng. Transaction of ASME, 2004. **126**(5): p. 567-577.

CHAPTER 4

MUCUS CLEARANCE - THE INFLUENCE OF MUCUS PROPERTIES AND SURFACTANT ON THE MUCUS PLUG CLEARANCE

4.1. Introduction

Many forms of respiratory diseases such as, asthma, cystic fibrosis and chronic bronchitis are characterized by an increased secretion of respiratory tract mucus. Thus, mucus plugging can form and block the breathing pathway, which threatens the patients' lives [1-4]. To clear the mucus in the pulmonary airways are essential to health and life safety. Mucus transport and clearance has been studied in two-phase flow regime before plugs are formed [5-12]. For example, Clarke et al. [5] studied the resistance of two phase gas-mucus flow in airways and showed that thicker mucus layer with lower air flow rate accompanied the increase of flow resistance. Kim et al. [6] studied two phase gas-mucus flow in the central airway and proposed the criteria of mucus transport: mucus layer transport speed and thickness increased with decreasing air flow rate.

Studies [8, 13-16] suggested that the nasal and lung mucus were markedly non-Newtonian with an appreciable elasticity, shear thinning, thixitropy and yield stress [17, 18]. Mucus rheology was also studied and found to be very important in neonatal RDS [19]. Surfactant was found to be able to change the viscosity of the mucus and improve the mucus clearance. Banerjee et al. [20] showed that the surfactant changed the viscosity of the mucus versus shear rate to follow a power law model. Positive effects of the surfactant were observed on mucus rheology. They also found that the shear thinning effect on mucus viscosity at relevant shear rates was very important when using a surfactant for diseases like asthma and chronic bronchitis. Craster et al. [21] studied the surfactant spreading behavior on mucus films with influence of two principle rheological properties of mucus, yield stress and shear thinning. The spreading behavior was shown to be severely retarded with the increasing effects of shear thinning and yield stress.

However, no study has included the effects of shear thinning and yield stress on the propagation and clearance of mucus plugs yet. Incorporation of these non-Newtonian effects into the recent lung modeling of plug propagations [22-25] can be advantageous. Therefore, in the present study, we focus on the shear thinning properties, liquid inertia and the effect of surfactant on the mucus plug clearance. To address the characteristics of mucus, several models give reasonable correlations, for example, power law model for shear thinning, Herschel-Bulkley constitutive law for both shear thinning and yield stress [21, 26, 27], Maxwell model [28] for viscoelastic behavior, and so on. For steady flow studied in this chapter, the yield stress and elastic properties are expected to be not very important for the mucus plug transport; therefore, the power law model is used for the mucus viscosity.

In this chapter, numerical simulations are performed for the steady mucus plug propagation along pulmonary airways. A mathematical model is used to study power-law plug propagation in a two-dimensional channel lined by uniform, thin liquid films with the inspiration pressure as the driving forces. The mechanisms of mucus clearance is studied through the mucus plug propagations with the effects of the non-Newtonian plug properties, inertia and the presence of surfactant.

4.2 Model Development

Model Description

The mathematical model is similar to that shown in Fig. 2.1 in Chapter 2. The gravity is neglected in this section and the plug viscosity is assumed to be non-Newtonian. The fluid viscosity μ^* is defined as a function of shear rate $\dot{\gamma}^*$ using a power-law model $\mu^* = K_n \left(\dot{\gamma}^*\right)^{n-1}$, where K_n is the consistency. The mucus viscosity is modeled based on the rheology of Sodium Carboxymethylcellulose (SCMC) material, which is shown to have similar shear thinning properties with mucus. The properties of which is shown in Table 4.1 [29], and the sample plots of the viscosity vs. the shear rate is shown in Fig. 4.1, in which $K_n = K_0 n^a$ and we get the fitting parameters K_0=*0.42* and a=-6.53 from the viscosity data of SMCS at Table 4.1. When the power law index n decreases or the shear rate decreases, the viscosity increases.

SCMC (%)	Power-law index (n)	Consistency Parameter (K) $(g/cm)s^{n-2}$	Surface Tension (σ) dyn/cm
0	1	0.01	72.4
0.67	0.7	3.04	71
1	0.56	24.9	70.6
1.5	0.5	33.5	69
2	0.375	255.1	68

Table 4.1 The properties of Sodium Carboxymethylcellulose (SCMC).

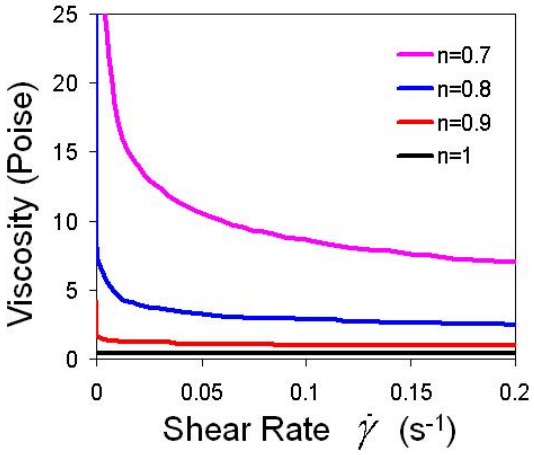

Figure 4.1 The sample plots of the viscosity vs. the shear rate for different power law index n. n=1 for Newtonian fluid, while n<1 for shear thinning fluid.

Governing Equations and Boundary Conditions

The steady flow inside the liquid plug is described by the dimensionless Cauchy equation and the continuity equation as

$$\begin{aligned} \mathrm{Re}\ \underline{u}\cdot\underline{\nabla}\,\underline{u} &= -\underline{\nabla}\,p + \underline{\nabla}\cdot\left(2\mu\underline{\underline{E}}\right) \\ \underline{\nabla}\cdot\underline{u} &= 0 \end{aligned} \tag{4.1}$$

where the viscosity μ is scaled by the Newtonian viscosity μ_0; $\underline{\underline{E}} = \frac{1}{2}\left(\underline{\nabla}\underline{u} + (\underline{\nabla}\underline{u})^T\right)$ and the shear rate $\dot{\gamma} = \sqrt{2\underline{\underline{E}} : \underline{\underline{E}}}$; the velocity, length, pressure and surface tension scales are the same as Chapter 2.2. The surfactant transport equations are shown in Chapter 2.2.2. The scaled viscosity equation is shown as:

$$\mu = \frac{K_n}{\mu_0}\left(\frac{U^*}{H^*}\right)^{n-1}(\dot{\gamma})^{n-1} \tag{4.2}$$

The capillary number studied in this chapter is defined as $Ca = \mu_0 U / \sigma$, in which μ_0 is the Newtonian viscosity. For the boundary conditions, the non-slip conditions are applied on the channel walls; kinematic conditions and stress balance conditions are applied on the plug interfaces. On the far end films, there is mass conservation from the trailing films to the precursor films and the fully developed flow is applied on the films. When the surfactant is present, the surfactant transport equations shown in Chapter 2.2 are solved as well.

Parameter Estimation

Typically, the mucus viscosity is at the range of 10^{-2} to 10^{2} poise [21]. The power law index is in a wide range of 0.3 to 1, with 1 to be Newtonian fluid. In this chapter, we present the studies in two regimes: Newtonian fluid with n=1 and μ=1 (μ is scaled with μ_0 = 0.42P), and power-law fluid with 0.6<n<1.

4.3. Numerical Grid and Methods

The curvilinear computational grid is generated in the same way as stated earlier. The physical domain (x,y) is mapped into the orthogonal computational domain (ξ,η) using the boundary fitted coordinate transformation [30]. The governing equations are

$$\frac{\partial}{\partial \xi}\left(\mathrm{Re}\, F^{\xi} \underline{u} - \frac{\mu B_{11}}{J}\frac{\partial \underline{u}}{\partial \xi}\right) + \frac{\partial}{\partial \eta}\left(\mathrm{Re}\, F^{\eta} \underline{u} - \frac{\mu B_{22}}{J}\frac{\partial \underline{u}}{\partial \eta}\right)$$
$$= -A^{T}\underline{\nabla}_{\xi} p + \frac{\partial}{\partial \xi}\left(\frac{\mu B_{12}}{J}\frac{\partial \underline{u}}{\partial \eta}\right) + \frac{\partial}{\partial \eta}\left(\frac{\mu B_{21}}{J}\frac{\partial \underline{u}}{\partial \xi}\right) + S_{\phi} \qquad (4.3)$$
$$\underline{\nabla}_{\xi} \cdot \underline{F} = 0$$

in which S_{ϕ} can be expressed as

$$S_{\phi} = \frac{\partial}{\partial \xi}\left(-\frac{\mu \partial v}{\partial \eta}\right) + \frac{\partial}{\partial \eta}\left(\frac{\mu \partial v}{\partial \xi}\right) \quad \text{for } u \text{ component}$$
$$S_{\phi} = \frac{\partial}{\partial \xi}\left(\frac{\mu \partial u}{\partial \eta}\right) + \frac{\partial}{\partial \eta}\left(-\frac{\mu \partial u}{\partial \xi}\right) \quad \text{for } v \text{ component} \qquad (4.4)$$

The SIMPLER algorithm is used to solve the momentum equation, the pressure equation, the pressure correction equation so that the calculated velocity field satisfies the momentum equations and continuity equation, as shown in steps (1)-(8) in Chapter 2.3. The viscosity, which is present in the coefficients are calculated using the velocities from

the previous iteration. A minimum critical $\dot{\gamma} = 10^{-5}$ is defined to prevent division by zero in Eqn. (4.2).

At far ends of the film regions, the fully developed conditions are applied and the mass balance occurs from the precursor films to the trailing films, which leads to $h_{p+} + h_{p-} = h_{t+} + h_{t-}$. as shown in Fig.2.2. In Chapter 2, the whole domain of the plug is calculated since there is plug asymmetry due to the gravity effect. In this chapter, we are using the same computational domain and the plug symmetry is verified. The trailing film thickness h_{t+} and h_{t-} are unknown quantities and part of solutions, thus the precursor films are updated to be $(h_{t+} + h_{t-})/2$ at each iterative step. In this steady state study, $h_{p+} = h_{p-} = h_{t+} = h_{t-}$ since the gravity effect is neglected. h will be used as the film thickness in the following text. The SuperLU solver [31] is used to solve the sparse linear system of the momentum, pressure, pressure correction and surfactant transport equations. The iterations continue until all equations and boundary conditions are satisfied, i.e. all corrections become negligible small, which satisfy: $\max\left(\left\|\underline{u}^{N} - \underline{u}^{N-1}\right\|\right) < 10^{-6}$ and $\max\left(\left\|\underline{x}^{N} - \underline{x}^{N-1}\right\|\right) < 10^{-3}$ (N is the iteration step).

In the grid generation for the plug domain, the film length is 15 units to the right meniscus and 18 units to the left. When the surfactant is present, the film length is 20 units to the right and 30 units to the left. The grid convergence is verified by comparing the trailing film thickness and pressure drops across the plug in different mesh systems.

4.4. Results and Discussions

In this section, the shear thinning properties of the fluid will be investigated as well as the effects of inertia and surfactant on mucus plug propagation. Both the pressure and the shear stress are plotted with surface tension scale $\prod = p^* / \left(\frac{\sigma_M^*}{H}\right) = Ca \cdot p$ and $\tau = \tau^* / \left(\frac{\sigma_M^*}{H}\right) = \mu \dot{\gamma}$.

4.4.1 Effect of Power Law Index n

Fig. 4.2 compares the streamlines, pressure and shear stress fields for Newtonian (n=1) (Fig. 4.2a) and power law (n=0.7) (Fig. 4.2b&d) plug with Ca=0.02 and LP=1 at

Stokes flow regime. The solid lines are streamlines; the color coded contour in the upper half of the plug represents the pressure and the lower is for the shear stress in Fig. 4.2a and b. Fig. 4.2c shows the axial velocity in the plug core center x=0 along y axis. Fig. 4.2d shows the viscosity color contour and velocity vectors in the plug domain.

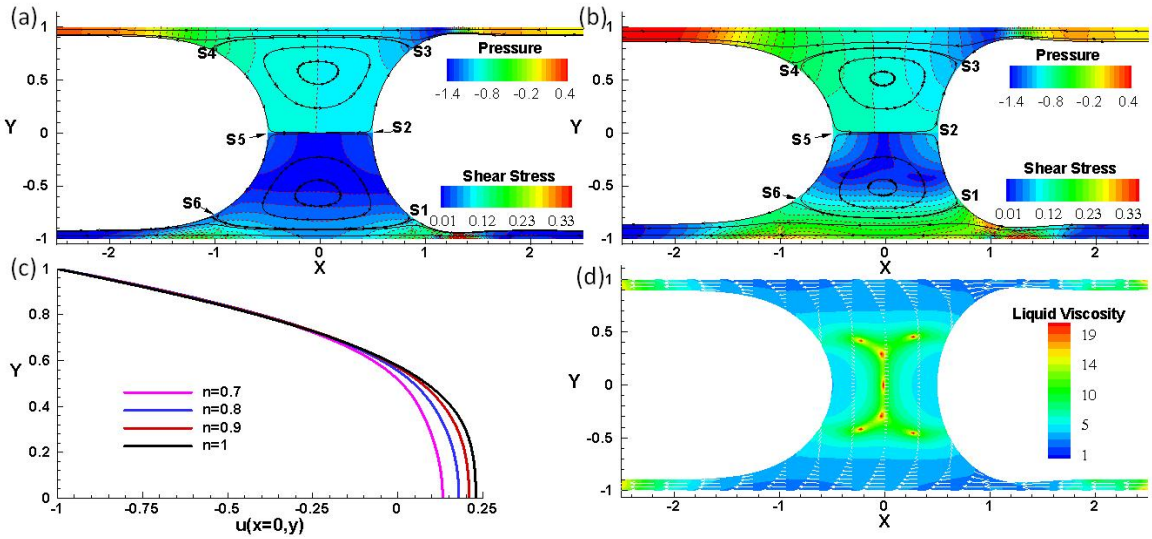

Figure 4.2 The streamlines, pressure, shear stress for LP=1, Ca=0.02 and Re=0 for (a) Newtonian n=1 and (b) power law n=0.7. The solid lines with arrows: steamlines, dash lines with color contour: pressure (upper half) and shear stress (lower half). (c) Center axial velocity u(x=0,y) for different n. (d) Viscosity color contour and velocity vectors as white arrows for n=0.7.

For a Newtonian plug, Fig. 4.2a shows the two types of flows: film flow and core recirculation flow as shown in Chapter 2.4. The stagnation points S1-6 appear along the interfaces to separate the film and core flows as well as separate the upper and lower half domains. The high negative pressure is achieved in the front transition region and a capillary wave occurs in this region with minimum film thickness developed, as discussed in Chapter 2. The shear stresses near the wall in both front and rear transition regions are higher than the plug core region. As n decreases (comparing Fig. 4.2a and Fig. 4.2b), trailing film thickness increases (h = 0.0794 and 0.135 for n=1 and 0.7) due to the increased effective capillary number from the increased effective viscosity. The vortex in the plug core is smaller and weaker and the stagnation points S1, S3, S4 and S6 moves towards the center. The pressure on the trailing films is found to increase and the shear stress is shown to increase near the wall and the plug tip. When the fluid is Newtonian, n=1, the dimensionless viscosity μ is 1 everywhere in the plug domain and film region.

While for a power law fluid with n=0.7, shown in 4.2d, the viscosity contour has higher value at the center of the plug core, the maximum in the plug core can be as high as around 22.4 and the far end film region, the viscosity is near infinity because of shear rate to be 0. Fig. 4.2c gives the axial velocity u(x=0,y) of the central cross-sectional plane along y axis. It is shown that u(x=0,y) flattens when n decreases because of the increased viscosity and decreased shear stress at the center.

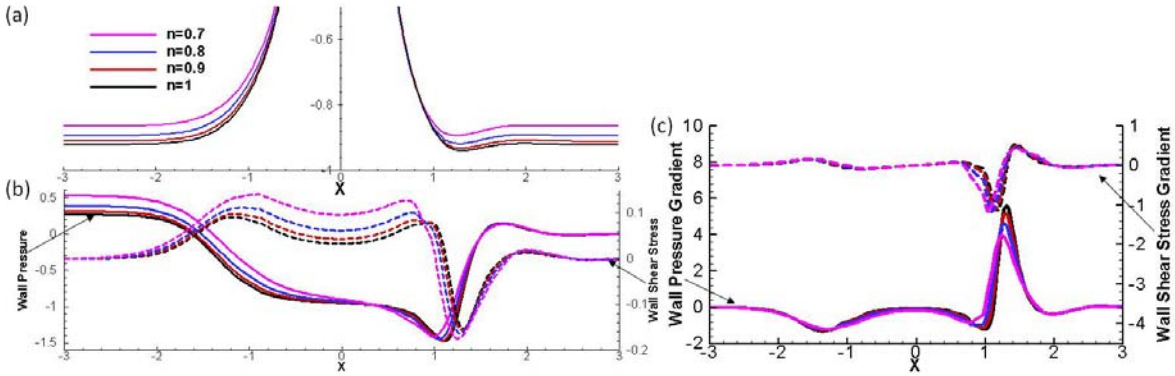

Figure 4.3 (a) The interface position, (b) wall pressure Π_w, and wall shear stress τ_w, and (c) wall pressure and shear stress gradients for different n at Ca=0.02, LP=1 and Re=0.

The interface position, wall stresses and wall stress gradients are then compared for different n at Ca=0.02 and LP=1, which is shown in Fig. 4.3a, b and c respectively. Again, in Fig. 4.3a, it can be seen that the film thickness increases in trailing films, both the front and rear interfaces move toward the center axial line and more liquid is deposited for smaller n. Fig. 4.3b shows that the wall pressure Π_w increases in the trailing films and rear transition regions with decreasing n. This is due to the increased pressure drop in the plug core region because of the increased effective viscosity when n decreases. The magnitude of wall pressure at the front transition region decreases due to the increased film thickness. The wall shear stress increases in the plug core, and both front and rear transition regions, but keep 0 on the films due to the fully developed flow on the films. The peak wall pressure gradient can be as high as 5.6 at n=1, and it decreases with decreasing n, with it to be around 4 at n=0.7. The shear stress gradient does not have much change in the magnitude, with peak value to be around -1.18, with decreasing n, but have slight spatial shift.

4.4.2 Effect of Plug Speed

Stokes Flow Regime

Fig. 4.4 demonstrates the variations of trailing film thickness *h* (4.4a) and pressure drop ΔΠ (4.4b) across the plug with the capillary number, which indicates the plug speed in Stokes flow regime, with both axes in log scale for different power law index n and LP=1 at the range of $5x10^{-3}$ <Ca<0.5. For Newtonian fluid, n=1, both film thickness and pressure drop show increases with increasing Ca, and log-log plot is shown to be linear when Ca is small; the slope of log*h* vs. logCa is around 0.6 and the slope of log(ΔΠ) vs. logCa is around 0.62 at Ca~0.006, which is close to the Bretherton's results $h=1.3377Ca^{2/3}$ and $\Delta\Pi \propto Ca^{2/3}$. While Ca is large, the slope decreases for the film thickness and increases for the pressure drop ΔΠ, which agrees with previous literatures [22, 23, 32, 33]. There are two components contributing to the pressure drop ΔΠ: (1) the viscous dissipation in the plug core, and (2) the net pressure jump across the air liquid interface. As n decreases, the pressure drop is found to increase because of the increased viscosity and increased viscous dissipation. When n decreases, we see the similar trend for *h* and ΔΠ, both h and ΔΠ increase with Ca but at a higher value. However, the curve slopes decrease: the slope for log h vs. log Ca is around 0.4 and that for log ΔΠ vs. log Ca is around 0.39 for n=0.7. This is mainly due to the increased effective viscosity in the plugs and increased effective capillary number, thus increased film thickness and shear stress with decreasing n.

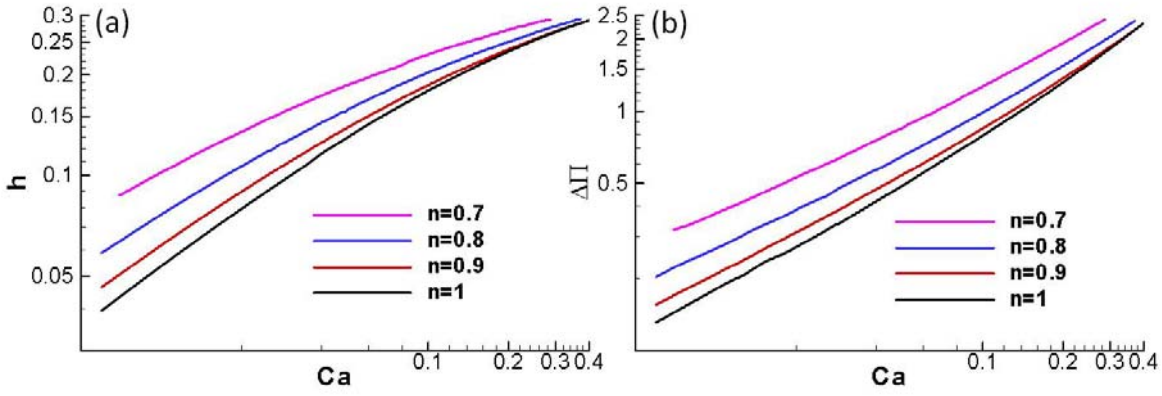

Figure 4.4 (a) The trailing film thickness *h* and (b) pressure drop ΔΠ vs. Ca with LP=1 at Stokes flow regime for different n.

Effect of Inertia

Fig. 4.5 shows the trailing film thickness *h* (4.5a) and pressure drop ΔΠ (4.5b) across the plug vs. the Reynolds Re for 5<Re≤55 with λ=1000 and LP=1 for four

different power law index, n=1, 0.9, 0.8 and 0.7. Both film thickness and pressure drop are found to increase with increasing Re and decreasing n. The slope of $\Delta\Pi$ vs. Re is found to be higher for smaller n. For n=1, the slope have slight change when Re increases, i.e. $\Delta\Pi$ vs. Re is roughly linear for Re<30 but curve up for Re is greater. For n=0.7, $\Delta\Pi$ vs. Re is linear for the whole range of 5<Re≤55. In other words, more increase in pressure drop is needed with increasing Re at small n. This shows the decreased effect of inertia when n decreases.

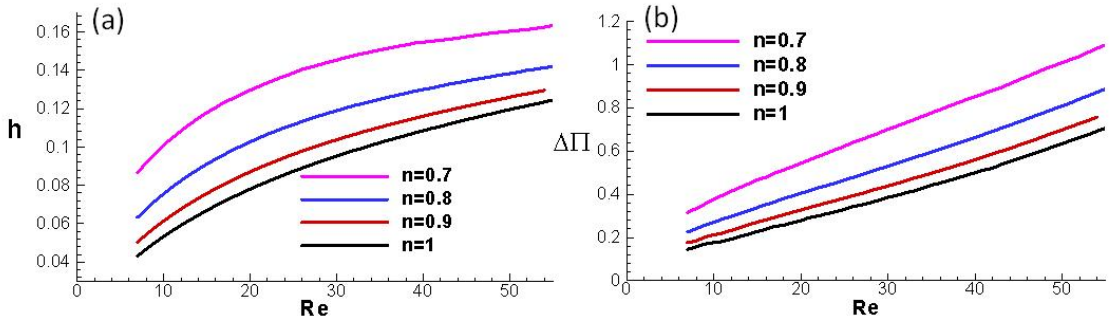

Figure 4.5 The trailing film thickness *h* (a) and pressure drop $\Delta\Pi$ (b) vs. Re with LP=1 and λ=1000 for different n.

4.4.3 Effect of Surfactant

Fig. 4.6 shows the streamlines, and the pressure fields in the upper half plug; and velocity vectors and shear stress fields in the lower half shown in 4.6a; and viscosity contour in the upper half plug while the surfactant concentration contour in the lower half shown in 4.6b with $C_0=10^{-4}$, Ca=0.02, Re=0, L_P=1, Pe=5 x10^2, $Pe_s=5x10^3$, $K_a=10^4$, $K_d=10^2$, E=0.7 and $\beta=10^{-2}$. The flow pattern indicates that there are two major flow regioins in the domain, one of which passes through the plug from the precursor film to the trailing film, the other is the recirculation region inside the plug core that does not communicate directly with the precursor and the trailing films. At the steady state, all the recirculation streamlines are closed and no convective momentum flux between these two regions. As there is no surfactant, all the six stagnation points attach the interfaces in the plug domain as shown earlier. With soluble surfactant shown in Fig. 4.6a, there is only one interfacial stagnation point at the tip, and the second one, however, appears on the midline inside the plug, off the meniscus tip, which is true for both front and rear interfaces. The streamline pattern varies with the surfactant concentration. The Marangoni stress causes the surface velocity to be almost zero, thus the recirculation zone

detaches from the interface. The recirculations are weaker and smaller as well compared to the surfactant-free case.

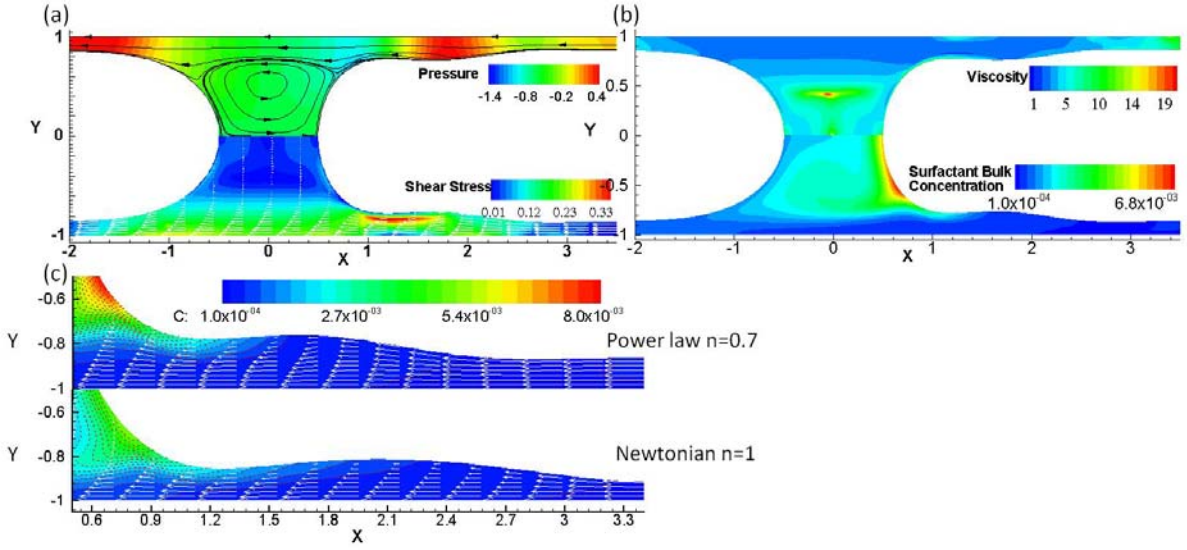

Figure 4.6 (a) The streamlines and pressure contour (upper half plug), velocity vectors and shear stress contours (lower half) for n=0.7; (b) the viscosity and surfactant bulk concentration for n=0.7; and (c) the zoomed front transition region with velocity vectors and color contour of surfactant bulk concentration for n=0.7 and n=1 with $C_0=10^{-4}$, Ca=0.02, Re=0, $L_P=1$, Pe=5 x10^2, $Pe_s=5x10^3$, $K_a=10^4$, $K_d=10^2$, E=0.7 and $\beta=10^{-2}$.

With no surfactant, a capillary wave is developed and local minimum film thickness is achieved in the front transition region at x=1.26 as shown in Fig. 4.2. However, with surfactant, shown in Fig 4.6a, the precursor film near the front meniscus at 1.0<x<2.0 is thicker than the film thickness far ahead of the plug, h=0.138, a local maximum film thickness in this region is achieved at x=1.66 with h=0.240 and local minima in this region is achieved at x=1.2 with h=0.224, and the minimum thickness h=0.132 is observed where this thick film region connects to the leading front precursor film. High pressure is developed where the thick films occur in the front transition regions. In the lower half domain of Fig. 4.6a, the shear stress contour is shown in color. Shear stress is found to be high in the film flow region but relatively low in the plug core region. Maximum shear stress is achieved in the thick film region near the front meniscus, between where the local minimum and local maximum film thickness occur.

The viscosity decreases in the plug core region and near the interfaces compared to the surfactant free case in Fig. 4.2c, due to the increased shear rate, shown in Fig. 4.6b. The bulk surfactant concentration is maximized, C~7x10^{-3}, at the front meniscus caused

by the accumulation of the interfacial surfactant here. The maximized surfactant concentration at the front meniscus thus minimizes surface tension in the interface so that Maragoni stress is developed to move the liquid away from the core interface and develop thick film in the front transition regions. The shear stress then increases in order to balance the increased Maragoni stresses.

When the thick film region is zoomed in, Fig. 4.6c shows the velocity vectors in the thick film region for n=0.7 and n=1 with color coded contour to be the surfactant concentration. The velocity profile in the front transition region is Couette-like linear shape for Newtonian flow n=1, rather than the uniform flow in the end film, which causes the thick films developed to conserve the mass [34, 35]. The velocity profile changes to non-linear shape for power law fluid, shown in 4.6c for n=0.7. The change of the velocity profile leads to higher shear stress in the front transition region. It can be seen that the maximal surfactant concentration is higher and the thick film region is shorter for n=0.7 than n=1. The increased shear stress near the interface in the front transition region leads to increased Marangoni stress and interfacial surfactant concentration gradients, therefore, shorter thick film region.

Fig. 4.7 summarizes the interface position (4.7a & b), interfacial surfactant concentration (4.7c & d), and surface velocity (4.7e & f) vs. arc length for different n at both rear and front interfaces. Arc length s is the horizontal axis, with s=0 defined at the interface tips on the midline, and it increases along the interface to the right but decreases along the left interface. When n decreases, the trailing film thickness h increases (4.7a); the gradient of interfacial surfactant concentration $\frac{d\Gamma}{ds}$ increases; and the rear transition regions shorten. While in the front transition region, the thick film region shortens and become thicker, as shown in Fig. 4.7b. The precursor film thickness near the front meniscus is thicker than the precursor film thickness far ahead and the maximum thickness in the front transition region is h_{max}=0.188 with trailing film thickness h=0.088, thus $h_{max}/h \sim 2.14$ at n=1 while h_{max}=0.24, h=0.138 and $h_{max}/h \sim 1.74$ at n=0.7. The decrease of h_{max}/h with decreasing n may be due to the velocity profile changes in the thick film region.

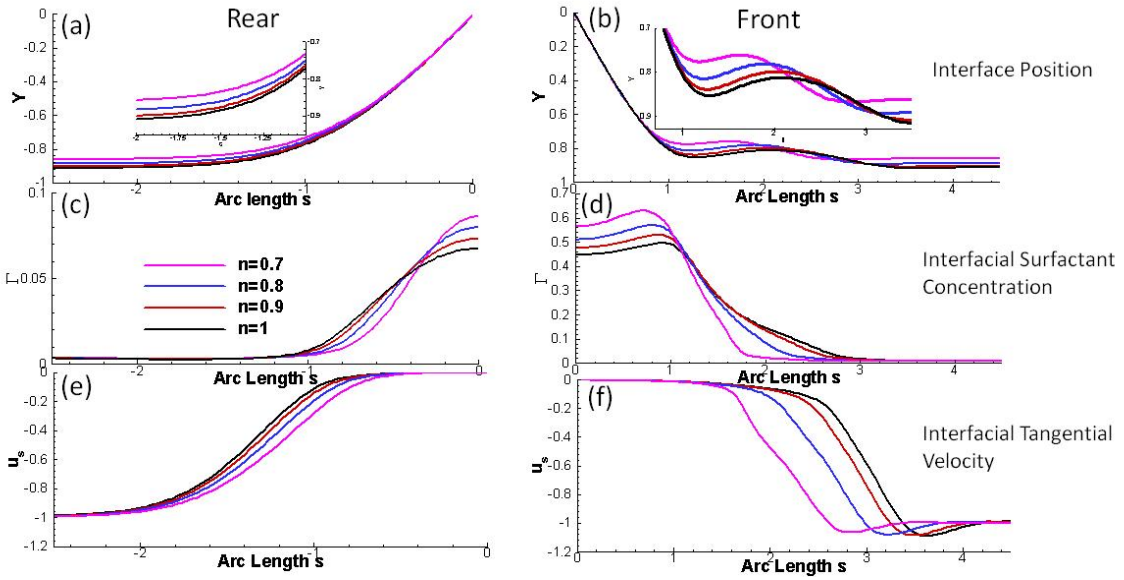

Figure 4.7 The interface position (rear at a and front at b), interfacial surfactant concentration (c & d), and the interfacial tangential velocity (e & f) vs. arc length for different n at $C_0=10^{-4}$, Ca=0.02, Re=0, $L_P=1$, Pe=5 $x10^2$, $Pe_s=5x10^3$, $K_a=10^4$, $K_d=10^2$, E=0.7 and $\beta=10^{-2}$.

As the plug propagates, the front meniscus sweeps up the preexisting interfacial surfactant in the precursor film. The interfacial surfactant accumulates on the front meniscus. Γ arises in the front meniscus and reach a maximum in the front meniscus surface, which causes a steep gradient in σ. As shown in Fig. 4.7c&d, the maximal Γ increases for both front and rear interface with decreasing n. In the front transition region for n=1, Γ_{max} is approximately 0.5 at s= 0.925 and the transition region span covers 0.925<s<3 where the gradient of Γ stays high. While for n=0.7, Γ_{max} is about 0.66 at s=0.7 and the transition region shifts towards the plug core and shorten at 0.7<s<1.9 for n=0.7. In the rear meniscus, Γ reach maximum at the meniscus tip with Γ_{max} ~ 0.0675 for n=1, and Γ_{max} ~ 0.0865 for n=0.7; the rear transition region shortens as well when n decreases. Thus along both front and rear interfaces, when n decreases, larger gradients of Γ is achieved, which causes stronger Marangoni stresses along the front and rear interface near the transition regions. The Marangoni stresses induced by the surface tension gradient oppose to the flow in the precursor film, which causes a rigid interface. The transitions from the thick film to the precursor film are similar for different n. However, the shortening of the thick film region causes the rigid interface shortens, which leads to

the shift of the surface velocity vs. the arc length towards to the plug core in both front and rear transition regions as shown in Fig. 4.7e&f.

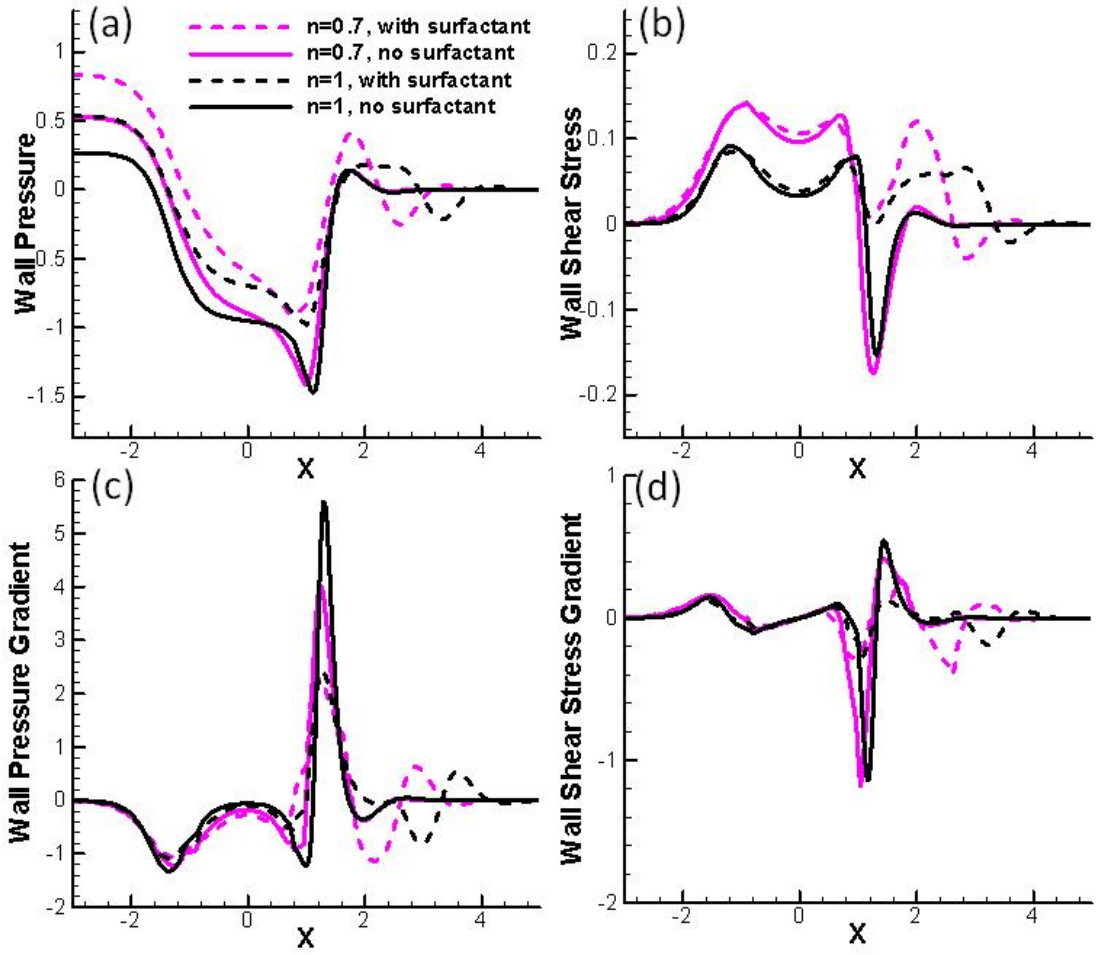

Figure 4.8 (a) Wall pressure (b) Wall shear stress (c) Wall pressure gradient (d) wall shear stress gradient along x for n =1 and 0.7 at the situations with or without surfactant.

The wall pressure and wall shear stresses are compared in Fig. 4.8a & b for n=1 and n=0.7 with or without the presence of the surfactant at Ca=0.02 and LP=1. The values of Π_W at the left end film increase with adding surfactant or decreasing n (Fig. 4.8a). The wall shear stresses increase near the rear and front transition regions with adding surfactant, the peak magnitude of wall shear stresses decreases near the front transition region, and a local maximum is developed in the thick film regions (Fig. 4.8b). The wall pressure increases in the rear films and the wall shear stress increases near the bulk and the front transition regions with decreasing n from the Newtonian to the power law fluid. With surfactant, local maximum are achieved in the front transition region and

is larger for the power law fluid than the Newtonian. This is due to the changes on the axial velocity profile, causing the local maximal stress to change and shift spatially towards the plug core with decreasing n. The wall pressure and shear stress gradients are shown in Fig. 4.8 c&d. The wall pressure gradient magnitude decreases with decreasing n and adding surfactant. The wall shear stress gradient has little change with n but decreases with adding surfactant as well.

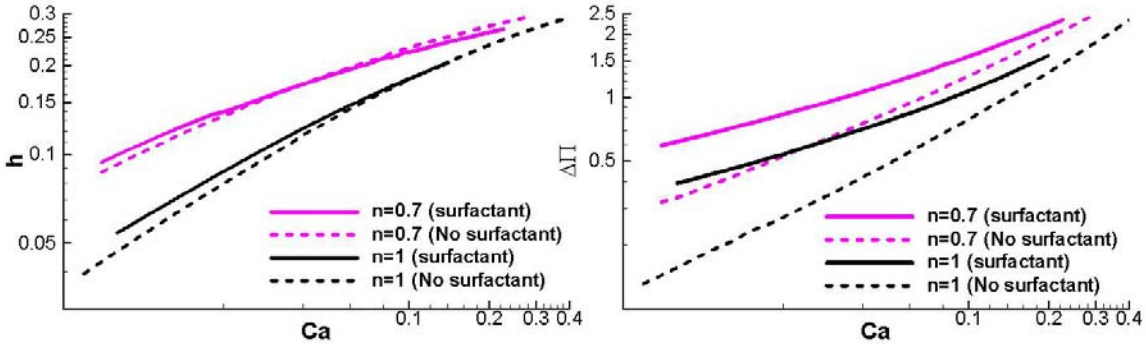

Figure 4.9 (a) The trailing film thickness *h* and (b) pressure drop ΔΠ vs. Ca with n=1 and n=0.7 at the conditions of surfactant or no surfactant at Stokes flow regime.

Fig. 4.9 shows the film thickness *h* (a) and the overall pressure drop ΔΠ (b) across the plug vs. Ca for two different power law components: power law fluid (n=0.7) and Newtonian fluid (n=1), with or without surfactant. The solid lines represent *h* and ΔΠ for surfactant-laden liquid plug when $C_0=10^{-4}$ is prescribed at the precursor film far ahead of the plug. The two dashed lines denote the "no surfactant" case as shown in Fig. 4.4. For all the cases, *h* increases as Ca increases. The increases of h have been shown in Fig. 4.4a with the increase of Ca and decrease of n without surfactant. When there is surfactant in Fig. 4.9a, the curves of h vs. Ca are more flatted with smaller slopes. For Newtonian fluid (n=1), the surfactant thickens the trailing film thickness when Ca<~0.12, but has little effects on the film thickness when Ca>~0.12. The thickening of the trailing film thickness with surfactant acts in a way similar to that for semi-infinite bubble propagation [36]. The interfacial surfactant in the rear meniscus lowers the surface tension, which results in a larger effective capillary number, thus increased h. However, for power law fluid (n=0.7), the trailing film thickness increases when Ca<0.0393 but decreases when Ca>0.0393. Though the surfactant lowers the surface tension in the rear meniscus, it lowers the liquid viscosity as well. With the two counteractive effects, the curves of h vs.

Ca for n=0.7 with or without surfactant cross at Ca=0.0393. Fig. 4.9b shows monotonic increases on ΔΠ with Ca for all the cases. Comparing the cases with and without surfactant, ΔΠ with surfactant is larger than that without surfactant for whole range of Ca in Fig. 4.9b. Therefore the surfactant increases the overall pressure drop across the plug. The Marangoni stresses induced by the surface tension gradient make the interface less mobile, requiring a larger force to move the meniscus. The curves of ΔΠ with surfactant have similar shape but smaller slopes comparing to the curves without the surfactant. When the power law index n decreases, the pressure drop ΔΠ increases. As mentioned earlier, the thick film region shortens for power law fluid when surfactant is present, which reduces the drag during plug propagation. Therefore, even though the surfactant causes the pressure drop ΔΠ to increase, the increase of ΔΠ is smaller and less dependent on Ca for power law fluid. In other words, for power law fluid, the effects of surfactant and plug speed are not as prominent as the cases of Newtonian plugs.

4.5. Conclusions

In this chapter, the flow and transport phenomena of the mucus plug are investigated in the mucus plug during mucus clearance from the pulmonary airways. The mucus properties are studied as well as the plug propagation speed and presence of surfactant. It is found that the power law fluid has a higher shear-thinning effect with decreasing the power law component n, which causes the effective viscosity, and shear stresses to increase. Consequently, the trailing film thickness and pressure drop increases due to the increased effective capillary number. The plug core recirculations become smaller and weaker with the decrease of n due to the increased viscosity in the plug core center. Larger driving force is required to drive the mucus plugs due to the increased shear stress when n decreases. When the surfactant is present, even larger pressure drop over the plug is needed to drive the mucus plug though the viscosity in the plug tends to decrease. A higher surfactant concentration is achieved along the plug menisci with decreasing n, which causes a higher Marangoni stresses for both front and rear transition region. A shorter but thicker film in the front transition region is found for smaller n, which compresses and amplifies the pressure and shear stress gradients. The existence of surfactant is found to decrease the viscosity of the plug core, therefore soften the mucus plug. Therefore, less force may be needed when surfactant is present for the initial

movement of mucus plugs before the development of thick film in the front transition regions and reaching the steady state. The existence of surfactant is found to increase the magnitude of wall stresses and stress gradients in the front transition region, leading to a potential higher risk of pulmonary epithelial cell damage.

References

1. Carroll, N., et al., *Airway structure and inflammatory cells in fatal attacks of asthma.* European Respiratory Journal, 1996. **9**(4): p. 709-715.
2. James, A.L., et al., *Time to death, airway wall inflammation and remodelling in fatal asthma.* European Respiratory Journal, 2005. **26**(3): p. 429-434.
3. Jensen, H.H., et al., *Potential misclassification of causes of death from COPD.* European Respiratory Journal, 2006. **28**(4): p. 781-785.
4. Shimura, S., et al., *Continuity of airway goblet cells and intraluminal mucus in the airways of patients with bronchial asthma.* European Respiratory Journal, 1996. **9**(7): p. 1395-1401.
5. Clarke, S.W., J.G. Jones, and D.R. Oliver, *Resistance to two-phase gas-liquid flow in airways.* Journal of Applied Physiology, 1970. **29**(4): p. 464-71.
6. Kim, C.S., et al., *Criteria for mucus Transport in the airways by 2-phase gas-liquid flow mechanism.* Journal of Applied Physiology, 1986. **60**(3): p. 901-907.
7. King, M., *Experimental models for studying mucociliary clearance.* European Respiratory Journal, 1998. **11**(1): p. 222-228.
8. King, M., G. Brock, and C. Lundell, *Clearance of mucus by simulated cough.* Journal of Applied Physiology, 1985. **58**: p. 1776-82.
9. King, M. and P.T. Macklem, *Rheological properties of microliter quantities of normal mucus.* Journal of Applied Physiology, 1977. **42**: p. 797-802.
10. King, M., et al., *The Role of Mucus Gel Viscosity, Spinnability, and Adhesive Properties in Clearance by Simulated Cough.* Biorheology, 1989. **26**(4): p. 737-745.
11. Scherer, P.W., *Mucus tranport by cough.* Chest, 1981. **80**(6): p. 830-833.
12. Scherer, P.W. and L. Burtz, *Fluid mechanical experiments relevant to coughing.* Journal of Biomechanics, 1978. **11**: p. 183-187.
13. King, D.M., et al., *Bulk shear viscosities of endogenous and exogenous lung surfactants.* American Journal of Physiology-Lung Cellular and Molecular Physiology, 2002. **282**(2): p. L277-L284.
14. Quraishi, M.S., N.S. Jones, and J. Mason, *The rheology of nasal mucus: a review.* Clinical Otolaryngology, 1998. **23**(5): p. 403-413.
15. Sheehan, J.K., et al., *Physical characterization of a low-charge glycoform of the MUC5B mucin comprising the gel-phase of an asthmatic respiratory mucous plug.* Biochemical Journal, 1999. **338**: p. 507-513.
16. Yeates, D.B., *Mucus rheology*, in *The Lung: Scientific Foundations*, R.G. Crystal and J.B. West, Editors. 1990, Raven Press, Ltd.: New York. p. 197-203.
17. Basser, P.J., T.A. McMahon, and P. Griffith, *The mechanism of mucus clearance in cough.* J. Biomech. Eng., 1989. **111**: p. 288-297.
18. Davis, S.S., *Rheological examination of sputum and saliva and the effect of drugs*, in *Rheology of Biological Systems*, H.L. Gabelnick and M. Litt, Editors. 1973, Charles C. Thomas: Springfield. p. 157-194.
19. Rubin, B.K., O. Ramirez, and M. King, *Mucus rheology and transport in neonatal respiratory-distress syndrome and the effect of surfactant therapy.* Chest, 1992. **101**(4): p. 1080-1085.
20. Banerjee, R., J.R. Bellare, and R.R. Puniyani, *Effect of phospholipid mixtures and surfactant formulations on rheology of polymeric gels, simulating mucus, at shear*

rates experienced in the tracheobronchial tree. Biochemical Engineering Journal, 2001. **7**(3): p. 195-200.
21. Craster, R.V. and O.K. Matar, *Surfactant transport on mucus films.* Journal of Fluid Mechanics, 2000. **425**: p. 235-258.
22. Fujioka, H. and J.B. Grotberg, *Steady Propagation of a Liquid Plug In a 2-dimensional Channel.* J. Biomech. Eng. Transaction of ASME, 2004. **126**(5): p. 567-577.
23. Halpern, D., O.E. Jensen, and J.B. Grotberg, *A theoretical study of surfactant and liquid delivery into the lung.* Journal of Applied Physiology, 1998. **85**(1): p. 333-352.
24. Howell, P.D., S.L. Waters, and J.B. Grotberg, *The propagation of a liquid bolus along a liquid-lined flexible tube.* Journal of Fluid Mechanics, 2000. **406**: p. 309-335.
25. Waters, S.L. and J.B. Grotberg, *The propagation of a surfactant laden liquid plug in a capillary tube.* Physics of Fluids, 2002. **14**(2): p. 471-480.
26. Herschel, W.H. and R. Bulkley, *Uber die viskositat und Elastizitat von Solen.* American Society of Testing Materials, 1923. **26**: p. 621-633.
27. Sherwood, J.D. and D. Durban, *Squeeze-flow of a Herschel-Bulkley fluid.* Journal of Non-Newtonian Fluid Mechanics, 1998. **77**(1-2): p. 115-121.
28. Satpathi, D.K., B.V.R. Kumar, and P. Chandra, *Unsteady-state laminar flow of viscoelastic gel and air in a channel: Application to mucus transport in a cough machine simulating trachea.* Mathematical and Computer Modelling, 2003. **38**(1-2): p. 63-75.
29. Low, H.T., Y.T. Chew, and C.W. Zhou, *Pulmonary airway reopening: effects of non-Newtonian fluid viscosity.* Journal of Biomechanical Engineering, 1997. **119**(3): p. 298-308.
30. Thompson, J.F. and Z.U. Warsi, *Boundary-fitted coordinate system for numerical solution of partial differential equations - a review.* Journal of Computational Physics, 1982. **47**: p. 1-108.
31. Demmel, J.W., et al., *A supernodal approach to sparse partial pivoting.* Siam Journal on Matrix Analysis and Applications, 1999. **20**(3): p. 720-755.
32. Giavedoni, M.D. and F.A. Saita, *The axisymmetric and plane cases of a gas phase steadily displacing a Newtonian liquid - A simultaneous solution of the governing equations.* Physics of Fluids, 1997. **9**(8): p. 2420-2428.
33. Halpern, D. and D.P. Gaver, *Boundary-Element Analysis of the Time-Dependent Motion of a Semiinfinite Bubble in a Channel.* Journal of Computational Physics, 1994. **115**(2): p. 366-375.
34. Borgas, M.S. and J.B. Grotberg, *Monolayer flow on a thin film.* Journal of Fluid Mechanics, 1988. **193**: p. 151-170.
35. Park, C.-W., *In fluence of soluble surfactants on the motion of finite bubble in a capillary tube.* Phys. Fluids A, 1992. **4**(11): p. 2335-2347.
36. Severino, M., M.D. Giavedoni, and F.A. Saita, *A gas phase displacing a liquid with soluble surfactants out of a small conduit: The plane case.* Physics of Fluids, 2003. **15**(10): p. 2961-2972.

CHAPTER 5

MICROFLUIDIC APPLICATIONS – PLUG DYNAMICS IN FLEXIBLE MICROCHANNELS AS A SMALL AIRWAY MODEL

5.1. Introduction

In various pulmonary diseases such as chronic obstructive pulmonary disease (COPD) [1], acute respiratory distress syndrome [2, 3], asthma [4-6] and cystic fibrosis [7, 8], the liquid layer coating the pulmonary airways tends to form a bridge due to the interfacial instabilities because of the deficient or dysfunctional lung surfactant. When a liquid plug forms in the pulmonary airways or alveoli, it blocks the gas exchange pathways. With the inspiration, the liquid plugs are forced to propagate through the airways and finally rupture to reopen the occluding airways [9]. Theoretical studies have suggested that the liquid plug or air bubble propagation during airway reopening process can generate fluid mechanical stresses, i.e. the normal and shear stresses on the wall, beyond the physiological values [10-15], which might cause cell damage and possiblye tissue damages as well.

Experimental studies [16, 17] have demonstrated severe injuries in surfactant-deficient lungs through the excised lungs or *in vivo* animal models. Cell injuries have also been investigated experimentally in Gaver's group [14, 18-20] during airway reopening by propagating the semi-infinite air bubbles through a parallel plate chamber with the walls cultured with airway epithelial cells. They found significant cell damages from the mechanical stresses and proposed that the pressure gradient near the bubble front was responsible for the cellular injury. Huh et al. [21] studied the cellular lung injury from the propagation and rupture of liquid plugs on the human airway epithelial cells in a microengineered airway system. They found that there are more cell injuries in the vicinity of where the plug ruptures and that the crackle sound may correspond to the cellular injury in the lungs.

However, these bench-top experiments are based on rigid channel/chambers. It is well known that the lung is compliant and the pulmonary airways are flexible and the airway flexibility varies with respect to the lung situations. In diseases like emphysema, the tissues or paranchyma in the lungs can be destroyed, which leads to over-compliant lungs; in chronic bronchitis, the airway walls can be thickened and leads to low-compliant lungs. Therefore, understanding the dynamics of plug propagation in flexible channels is essential to knowing the stresses on the lining cells and corresponding cell injuries. In this chapter, the plug propagation is investigated through flexible microchannels with both experiments and numerical simulations, and try to provide the insights on the mechanisms of potential cell injuries at in-vivo situations.

5.2. Experimental Methods

5.2.1 MicroChannel Fabrication

The microfluidic channels were fabricated using soft lithography [22]. Poly(dimethylsiloxane)(PDMS) (Slygard 184; Dow Corning, MI), pre-polymer was mixed with curing agent at a weight ratio of 10:1. The mixture was then cast onto a 4 in. silicon wafer with 100μm thick positive relief patterns of SU-8 50 of microchannels and cured at 60 ºC overnight. The cured PDMS layer was peeled from the silicon wafer. Holes of 2mm diameter were punched through the cured PDMS substrates as reservoirs. To fabricate a very thin membrane of PDMS (thickness ~O(5μm)), PDMS and toluene were mixed at 1:1 mass ratio using a vortex mixer and the resulting mixture was allowed to sit for around 5 minutes before use to remove bubbles. The toluene-diluted PDMS prepolymer was spin-coated on a silanized clean glass cover slide for one and a half minutes (3 s for 500rpm, ramped at 500rpm/s to 1800rpm for 90 s) to generate a thin layer. This thin layer covered glass slide was then cured at 120 ºC for an hour and transferred to a plain PDMS thin membrane with thickness of 7μm, which was similar to the wall thickness of the distal airways in human lungs [23]. The cured thin membrane and channel layer were then sealed against each other using a plasma oxidizer (11005-plasma Prep II, SPI, West Chester, PA) [22]. This assured the entire channel to have the same surface properties and be hydrophilic. PDMS with 10:1 curing ratios has Young's modulus around 0.7MPa and Poisson ratio about 0.5 [24-26]. This is comparable to the connective tissue network in the normal lungs. The elastin in the lungs has Young's

modulus in the order of 0.5-5MPa [27]. The average Young's modulus of a single alveolar wall was estimated to be around 300kPa [28]. PDMS is justified to be used as elastic materials with similar elastic properties as the normal lungs.

The fabricated channel has to be vertically flip 90º so that the thin membrane is shown as a side wall under an inverted microscope. This way the thin membrane deformation due to the pressure drop over the membrane can be well observed under the microscope. A razor blade was used to cut through the sealed structure near one channel wall along the axial direction; PDMS is then used to cure the rough cutting side again with a vertical level so the cured side keeps 90º with the near surfaces. The schematic of microchannel is shown in Fig.5.1a and the cross section of which is shown in Fig. 5.1b. The back of the channel (Height LH and width LW) is sealed with the thin membrane with thickness t, when $P_{ext}>P_{in}$, then membrane will deform inwards, thus from the inverted microscope, we can detect the deformation of the wall from the bottom. The height LH and width LW is roughly 100μm and the thin wall thickness t is roughly 7 μm.

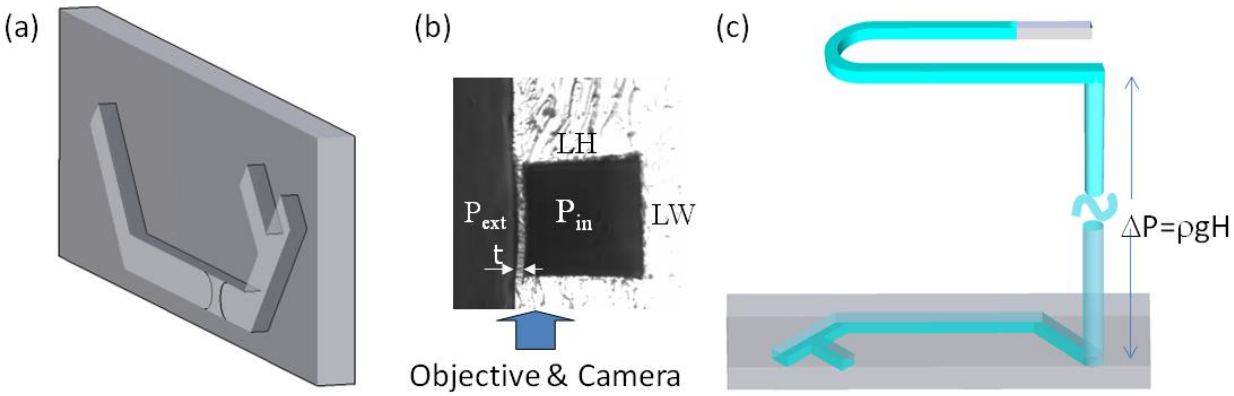

Figure 5.1 (a) Schematic of microchannels sealed with thin membrane with liquid plugs moving in the main channel. (b) the cross section of the microchannel. (c) schematic of compliance measurement (pressure-volume relationship).

5.2.2 Compliance Measurement

In the compliance measurement of the microchannels, two sets of channels were fabricated, one was the replica of PDMS microchannel sealed with a glass slide, and the other was the PDMS microchannel replica sealed with the PDMS thin membrane. De-ionized water with dye was used for compliance measurement. The microchannels were filled with water first, then the outlet is sealed with permanent glue to keep seamless. The inlet was then connected to U-shaped microchannel (PDMS sealed with a glass slide) via

0.8mm id silicone tubing (Fisher Scientific) with water filled, as shown in Fig. 5.1c. As the U-shaped microchannel was higher (lower) than the microchannel, the pressure inside is above (below) than the outside. The thin membrane deforms and water volume increases (decreases) in the target microchannel. Therefore the interface marker in the U channel moves, from which we can calculate the volume changes and pressure changes. The pressure-volume relationship thus reveals the compliance of the target microchannels.

5.2.3 Liquid Materials and Plug Visualization

The liquid material used is the mixture of de-ionized water and fluorescence particles (Duke Scientific) with the diameter 0.5 μm and density 1.05g/cm^3 at concentration around 0.1%. The fluorescent particles can be excited by the blue light at 468nm and emit green light at 508nm. The microchannels were filled with the liquid. The inlet and outlet are connected to reservoirs which were open to the atmosphere. A pair of air bubbles were injected in the liquid through a side channel using a 10μL syringe. The plug propagated with a specified pressure from the gravity pump. A CCD camera (Hamamatsu Orca-100), connected to an inverted fluorescent microscope (TE-300, Nikon, Tokyo, Japan), and SIMPLE PCI software (Compix Inc.) were used to record the plug motion and wall deformation.

5.3. Experimental Results

5.3.1 Channel Compliance

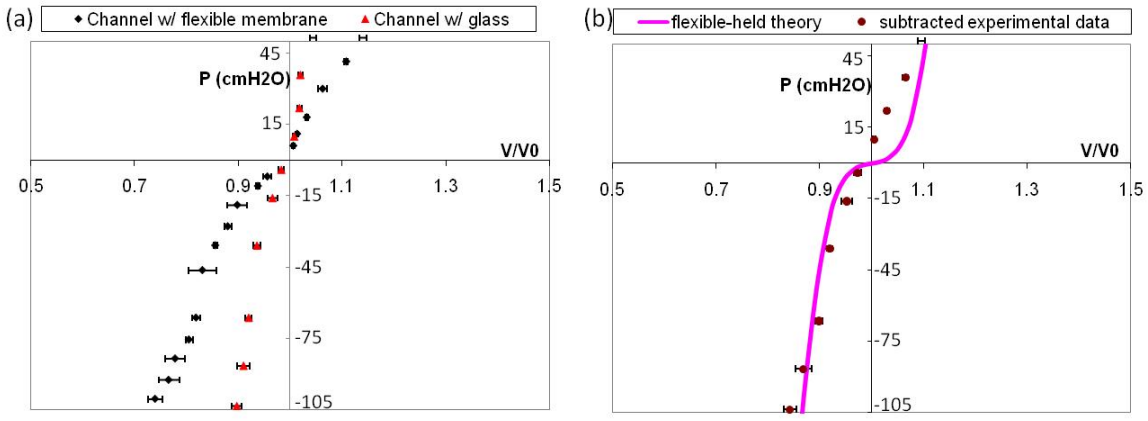

Figure 5.2 (a) pressure P (cmH_2O) vs. the dimensionless volume V/V0 for the microchannels with flexible membrane and with glass slide. The red (black) symbols with error bars in volumes are for the rigid (flexible) channel. (b) P vs. V/V0 from the deformation of the thin membrane by subtracting the two data sets in (a) and compare with the large deflection theory.

Fig. 5.2a shows the pressure –volume measurements for the PDMS microchannel sealed with the PDMS thin membrane, called the flexible channel, and with a glass slide, called the rigid channel, as a control. The red symbols with error bars in volumes are for the rigid channel. The rigid channel shows slight volume increases (decreases) with pressure increases (decreases). This is due to some elasticity of the PDMS polymer materials. The black symbols with error bars in volume represent the flexible channel. With the same pressure, the flexible channel shows a larger change of volume than the rigid channel, which is believed due to the deformation of the thin PDMS membrane. By subtracting these two curves, we can get the pressure-volume relationship just due to the thin flexible PDMS membrane shown as the symbols in Fig.5.2b. When the pressure is positive, the outer pressure is smaller than the inner pressure in the channel. Tthe thin membrane then expands outwards and the channel volume increases. When the pressure is negative, the outer pressure is larger than the inner pressure. The thin membrane is then sucked and deforms inwards and the channel volume decreases. This study is mostly interested in negative pressure region because the plug propagation has shown to result in a large negative pressure when it passes by from Chapter 2 and 4.

A large deflection theory on a clamped thin plate was used to calculate the compliance of our PDMS microchannel from the thin membrane deformation using Von-Karman's equations [29-33]. In a channel with height and width 100μm, length 4cm, the deformation of the thin PDMS membrane with Young's modulus around 0.7MPa and Poisson ratio about 0.5 [24-26], is calculated in the membrane coordinate, as shown in the purple curve of Fig. 5.2b. The results show agreements with our measurements when the pressure is negative. The properties of the PDMS during expansion may be quite different as that during the compression. Since the negative pressure ranges are of interest, the inconsistency of PDMS properties during expansion and compression is not expected to affect our analysis.

The average compliance of the flexible channel is calculated and compared with the airway compliances so the usage of the flexible channel can be justified. The average compliance is defined as $C = \Delta\left(V/V_0\right)/\Delta P$. From Fig. 5.2, we can calculate C to be around 0.003 to 0.006 cmH_2O^{-1}at pressure is at the range of -100 ~ 0 cmH_2O. For the human bronchioles, it was shown that the average in vivo compliance is a bit larger,

~O(0.01) cmH_2O^{-1} at pressure of -40 to 0 cmH_2O [23]. Since our microchannel only has one flexible wall, the compliance of the channel is expected to be reasonable and able to show the deformation properties of the actual human airways.

5.3.2 Wall Deformation from Plug Propagation

The liquid plug is generated in the microchannels by instilling pairs of bubbles from the side channel and the liquid plug propagates driven by the hydrostatic pressure from the gravity pump. With the negative pressure generated by the liquid plug propagation, the wall deformation is observed. As can be seen in Fig. 5.3 a, the upper wall is rigid and the lower wall is the thin flexible membrane. Fig. 5.3 b shows the extracted wall positions regarding to the plug propagation for different plug length and propagation speed. From the large deflection theory, the maximum thin membrane deformation is estimated to be about 12μm with uniform pressure load of $p=10^3 Pa$ on the thin membrane of 100μm wide and 4cm long.

Figure 5.3 The snapshot images under microscopes for the plug propagation in a microchannel with upper wall rigid and lower wall flexible with plug length to be around (a) 2.5 x channel height H (b) 0.55 x channel height.

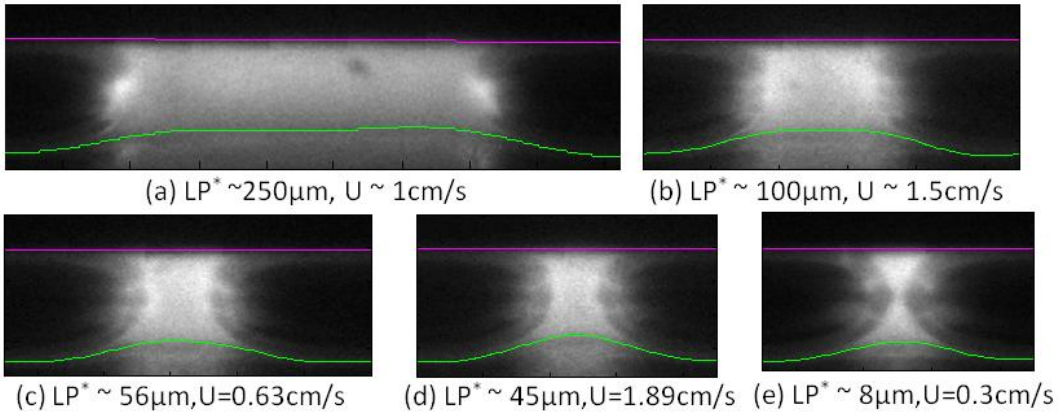

Figure 5.4 The snapshot images with extracted wall positions for different plug length and plug speed. The purple lines represent the top rigid walls and the green lines represent the bottom flexible walls.

Quantitative information was achieved by extracting the wall shapes from the snapshot images at instant plug length and plug speed, as shown in Fig. 5.4. The purple

lines represent the top rigid walls and the green lines represent the bottom flexible walls. The maximum deformation for each case are calculated to be (a) 15.5μm (b) 14μm (c) 12.5μm (d) 15.5μm and (e) 11μm with error of 2 μm. Comparing case (c) and (d), the plug length is very close, however the plug propagates in a larger speed for case (d) and results in a larger deformation. When the speed changes relatively small, the deformation seems to decrease with decreasing the plug length. The average strain on the bottom walls are calculated to be in the range of 0.7%-1.2% for the five cases, which increases with decreasing the plug length. The plug interface is shown to be asymmetric due to the deformed wall compared to that in a rigid channel.

5.4 Theoretical Formulation

5.4.1 Model Description

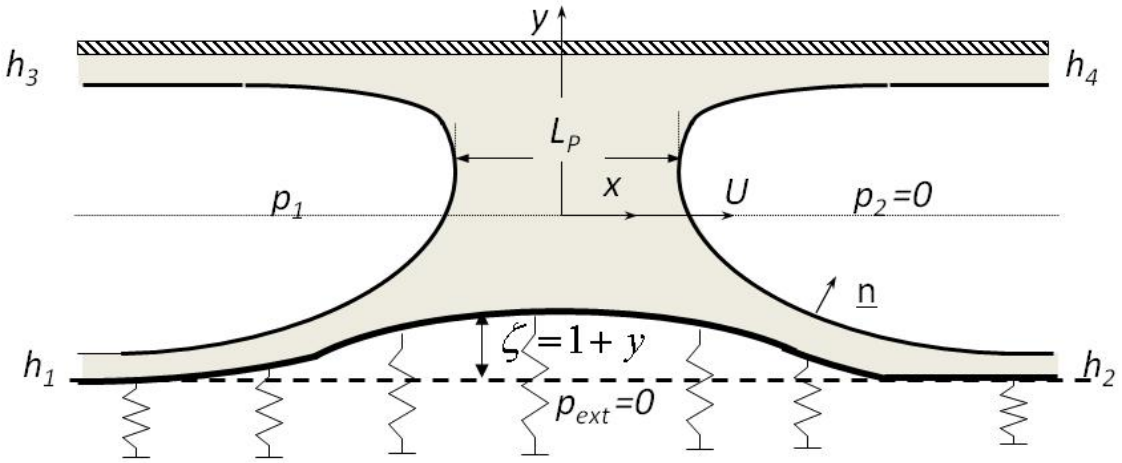

Figure 5.5 Schematic of the model system of a liquid plug driven by pressure drop p_1-p_2 through planar fluid-filled channel with upper wall rigid and lower wall flexible.

The plug propagation through a 2-D channel with lower wall flexible is illustrated in Fig. 5.5. A liquid plug propagates with steady speed U^* relative to the channel, driven by the pressure drop $p_1^* - p_2^*$. The fluid has Newtonian viscosity μ, and constant density ρ. The surface tension σ, is assumed to be uniform. The viscous fluid is modeled in a channel with a rigid upper wall and a membrane-like lower wall with constant longitudinal tension T_L^* and supported by nonlinear springs, the parameters of which are obtained from the experiments. Far ahead of the plug, the channel has a width of $2H^*$, and the springs are unstressed. Far behind the plug, the springs are slightly compressed due to the positive pressure p_1^* and uniform liquid films on each of the channel walls h_1^* at the

lower flexible wall and h_3^* at the top rigid wall. The precursor films along the lower flexible and tip rigid walls are h_2^* and h_4^*.

5.4.2 Governing Equations

The parameters are nondimensionalized as follows. Lengths *(x, y)* are scaled on half channel width H^*, pressure on the viscous force scale $\mu U^*/H^*$, and velocity $\underline{u} = (u, v)$ are scaled on U^*. For steady plug flow in the microchannels corresponding to the experiments, the flow governing equations (Navier-Stokes equations) may be approximated to Stokes flow equations and continuity, which in scaled form are

$$\underline{\nabla} p = \nabla^2 \underline{u}\,, \quad \underline{\nabla} \cdot \underline{u} = 0 \tag{6.1}$$

Along the front and rear menisci, the dimensionless interfacial stress conditions are given by

$$-p\,\underline{n} + (\underline{\nabla}\,\underline{u} + \underline{\nabla}\,\underline{u}^T) \cdot \underline{n} = Ca^{-1} \kappa_{ITF}\,\underline{n} - p_2\,\underline{n} \tag{6.2}$$

in which $\underline{n}$ is the interface inward-facing normal direction; the capillary number $Ca = \mu U^* / \sigma$ represents the ratio of viscous to the capillary stresses and can be considered as a dimensionless plug tip velocity; the interfacial surface curvature $\kappa_{ITF} = \underline{\nabla}_s \cdot \underline{n}$, where $\underline{\nabla}_s = \left(\underline{\underline{I}} - \underline{n}\underline{n}\right) \cdot \underline{\nabla}$ is the surface divergence vector. At both air-liquid interfaces, the kinematic boundary conditions for the steady state are $\underline{u} \cdot \underline{n} = 0$.

The lower flexible wall is assumed to be massless and the springs may slide freely in the x direction so that they always remain vertical. The variations in wall tension from tangential viscous stresses are assumed to be negligible. Therefore the tangential stress boundary condition along the bottom flexible wall is neglected. Under steady state conditions, a moving reference frame is chosen on the plug tip. The lower flexible wall is a membrane and is assumed to move normal to itself in the laboratory frame and tangential to itself in the moving frame. For steady plug propagation at the Stokes flow regime, the effects of membrane damping and inertia are neglected due to the thin flexible wall studied, thus the simplified normal stress at the bottom wall is balanced with the spring forces and wall tension as discussed in [11, 15],

$$T_L \kappa_{LW} - f(\zeta) = -Ca\,\underline{n_w} \cdot \underline{\underline{T}} \cdot \underline{n_w} \tag{6.3}$$

where $T_L = \frac{T_L^*}{\sigma}$ is the dimensionless longitudinal tension on the lower flexible wall, κ_{LW} is the curvature on the lower flexible wall $\kappa_{LW} = \underline{\nabla}_s \cdot \underline{n}_w$, $\zeta(x)=1+y$ is the lower wall deformation with undeformed wall $\zeta(x)=0$, $f(\zeta)$ represents the nonlinear force dependence on the wall deformation ζ,; $f(\zeta)$ is obtained by fitting the pressure-deformation curve of the flexible channels from the P-V measurements discussed earlier. A cubic spring function is obtained with the formula $f(\zeta)=A\zeta^3 + B\zeta$ where A=76.8 and B=0.13. The right hand side of Eqn (6.3) can be calculated from the fluid stresses:

$$\underline{n}_w \cdot \underline{\underline{T}} \cdot \underline{n}_w = -p + \underline{n}_w \cdot (\underline{\nabla}\, \underline{u} + \underline{\nabla}\, \underline{u}^T) \cdot \underline{n}_w \tag{6.4}$$

The normal stress Π_w and shear stress τ_w on the wall from the fluid is defined as follows with the surface tension scale.

$$\begin{aligned} \prod_w &= Ca \cdot \underline{n}_w \cdot \underline{\underline{T}} \cdot \underline{n}_w \\ \tau_w &= Ca \cdot \underline{t}_w \cdot \underline{\underline{T}} \cdot \underline{n}_w \end{aligned} \tag{6.5}$$

5.4.3 Boundary Conditions

In the plug tip frame of reference, the no-slip conditions at the walls are:

$$\underline{u} = \underline{t}_w \tag{6.6}$$

where $\underline{t}_w$ is the tangential vector along the wall and $\underline{t}_w = (-1, 0)$ on the top rigid wall, and $\underline{t}_w = \frac{(-1, -\zeta_x)}{(1+\zeta_x^2)^{1/2}}$ on the bottom flexible wall.

For all the end films, the fully developed conditions are applied for the fluid velocity. At steady state, the mass leaving the front is the same as that coming into the rear at each wall, which is simplified as $h_2 = h_1$ and $h_4 = h_3$. The pressure at the precursor films is equal to the front gas pressure ($p_2=0$) and in the trailing films equals the rear gas pressure p_1 as a part of solution.

5.4.4 Parameter Estimation

In actual pulmonary airways, the airway geometry depends on the generations and the liquid properties depend on the lung status or the instilled liquid properties, as discussed in Chapter 2.2.4. The microchannel investigated in this chapter is justified in Section 5.3.1, based on which the theoretical parameters are chosen. In the experiment,

H^*~ O(100μm), ρ~1g/cm^3, μ~O(0.1P), σ~O(50dyne/cm), the liquid speed is estimated to be O(1cm/s), thus Ca ~O(10^{-3}), Re~O(0.1). The inertia is negligible. The longitudinal tension is assumed to be at the same order with the surface tension.

5.5 Numerical Methods

The curvilinear computational grid was generated in a similar way as discussed in Chapter 2 and 4 from two dimensional Poisson's equation [34]. SIMPLER algorithm [35] is used to solve momentum and pressure equations as well. The detailed procedure is shown in Chapter 2.3. In this study, the wall equation is solved using Newton's method. The wall position is updated semi-steadily and the cubic splines [36] are applied to approximate the wall shape as the function of the arc length.

The wall equation is decretized with finite difference method, and a function is defined:

$$\Psi\left(\underline{\zeta}\right) = -\frac{T_L}{L^3}\left(d_{2e}\zeta_e + d_{2p}\zeta_p + d_{2w}\zeta_w\right) + \frac{f\left(\zeta_p\right)}{L} + F \tag{6.7}$$

where $L = \left(1 + \left(d_{1e}\zeta_e + d_{1p}\zeta_p + d_{1w}\zeta_w\right)^2\right)^{1/2}$ and $F = -Ca\underline{n_w} \cdot \underline{\underline{T}} \cdot \underline{n_w}$.

Using Newton's method, the Newton's Jacobi matrix can be calculated to be

$$J_{newton} = \begin{bmatrix} & 0 & \ddots & \ddots & \ddots & 0 & 0 & & \\ 0 & \cdots & 0 & \dfrac{\partial\Psi}{\partial\zeta_e} & \dfrac{\partial\Psi}{\partial\zeta_p} & \dfrac{\partial\Psi}{\partial\zeta_w} & 0 & \cdots & 0 \\ & & & 0 & \ddots & \ddots & \ddots & 0 & \end{bmatrix} \tag{6.8}$$

At each iteration, after the momentum and pressure equations are solved and the flexible wall shape is updated with $\delta\underline{\zeta}$, which is solved numerically from

$$J_{newton}\delta\underline{\zeta} = f\left(\underline{\zeta}^k\right) \tag{6.9}$$

Thus, the bottom flexible wall is corrected by $\underline{\zeta}^{k+1} = \underline{\zeta}^k - \delta\underline{\zeta}$, and this correction repeats with each iteration after the velocity and pressure fields are achieved and the plug

interfaces are updated until the correction become negligible small, which satisfy: $\max\left(\left\|\underline{\zeta}^{k+1}-\underline{\zeta}^{k}\right\|\right)<10^{-3}$ (k is the iteration step).

5.6 Theoretical Results

Fig. 5.6a shows the streamlines and pressure fields of steady plug propagation in a two-dimensional channel with top wall rigid and bottom wall flexible at Ca=0.01, T_L=1 and LP=1. Two major flow regions are shown again: film flow near the wall from the precursor films to the trailing films, and the plug core recirculatoins. Two stagnation points S2 and S5 at the interface tips separate the upper and lower recirculation. The recirculation center at the lower half domain moves towards the center due to the deformed wall, which locates at y=-0.515 while the upper one is at y=0.617. The stagnation points S1 and S6 separate the wall layer flow and the core recirculation in the lower half domain and they move up towards the center as well, with S1 is at x=0.918, y=-0.722 and S6 at x=-0.981, y=0.73. S3 and S4 separate the film flow from the core flow in the upper half domain with S3 at x=0.917, y=0.85 and S4 at x=-1.083, y=0.848.

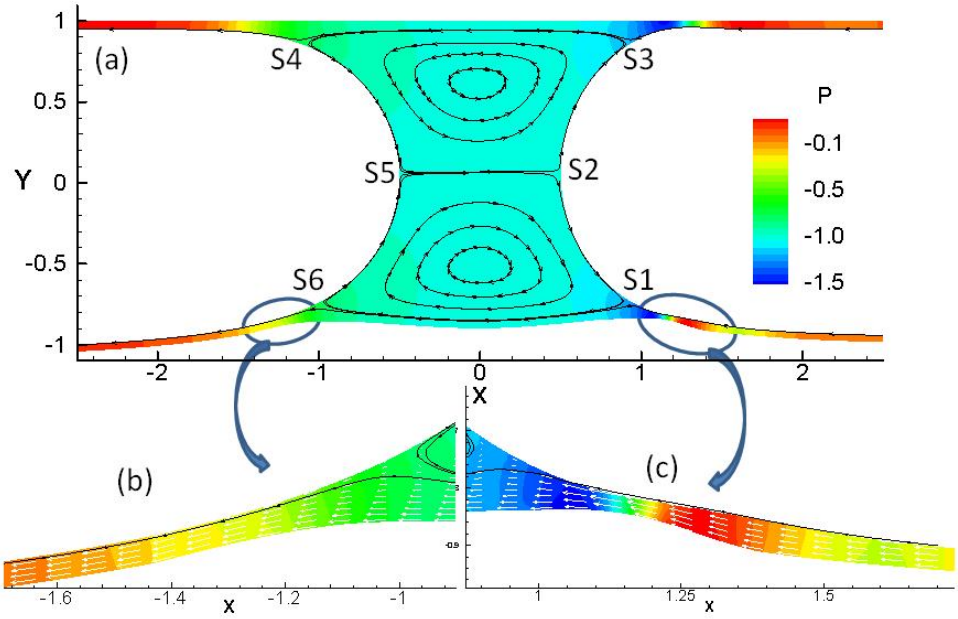

Figure 5.6 (a) The streamlines (black solid lines) and pressure fields (color contour) in a 2-D channel with top wall rigid and bottom wall flexible at Ca =0.01, T_L=1 and LP=1. Zoomed films in the (b) rear and (c) front transition regions near the flexible wall. The white arrows are the velocity vectors. The color coded contour represents the pressure fields and the solid black lines with arrows are streamlines

The capillary wave exists on the front interface near the upper rigid wall where the plug core is connected to the upper precursor film. However, the capillary wave disappears along the front interface near the bottom transition region. The zoomed-out film near the bottom front transition region is shown in Fig.5.6c. The front interface extends monotonically to the far-ahead of film near the bottom wall. In the lower film, however, minimum film thickness still occurs and an oscillation on the film thickness occurs as well due to the non-uniform wall deformation. This result is consistent with Howell et al.[37]. They also found the capillary wave diminished in the front interface in some cases of η; however, the local minimum film thickness is still developed in the front transition region due to the deflection of the wall.

In this parameter set, the bottom wall deformation is largest near the front transition region, which then causes the minimum film thickness to occur. This oscillation on the film thickness results in an oscillation on the fluid pressure: pressure is quite low when the fluid is approaching the thinnest film location from the plug core region and pressure increases when film is expanding. In the rear transition region as shown in Fig. 5.6b, the film thickness decreases monotonically to the far-behind region, so do the wall deformation and rear meniscus. In Fig. 5.6b & c, the velocity vectors are also shown with the white arrows. Fig. 5.6c shows larger speed on the interface than the wall near the thinnest film region, which causes a high negative shear stress but the opposite towards the plug core, i.e. a high positive shear stress region, thus a high shear stress gradient may be achieved and the risk of cell damage on the airways can be increased.

Fig. 5.7a shows the wall normal stress Π_w (solid lines) and its gradient $d(\Pi_w)/ds$ (dash lines) along the wall arc length s on the flexible wall and rigid wall when plug propagates through at Ca=0.01, LP = 1 and Re = 0. s = 0 corresponds to x = 0 and s = x for the rigid wall. The red curves represent the values on the flexible wall, and the blue curves represent that on the rigid wall. The peak magnitude of Π_w has a slight increase on the flexible wall (Π_w=1.567) than a rigid one (Π_w=1.448) and the peak location shifts towards the center on the flexible wall at x=1.09 and peak at x=1.192 for the rigid wall. Π_w has slightly larger magnitudes near the plug core ($\Pi_w \sim$ -1) and the

exposure region of a high negative magnitude on the wall near the plug core is shorter for the flexible than the rigid. This causes a much higher gradient of the normal stress near the transition regions along the flexible wall. The peak normal stress gradient $d(\Pi_w)/ds$ is shown on the front transition region, and its magnitude is shown to be 14.4 on the flexible wall, which is more than double of that on the rigid wall, $d(\Pi_w)/ds$ =6.7. In the front transition region, the local peak magnitude of $d(\Pi_w)/ds$ is ~ 2.3 on the flexible wall is also larger than that on the rigid wall, i.e. $d(\Pi_w)/ds$ ~1.5.

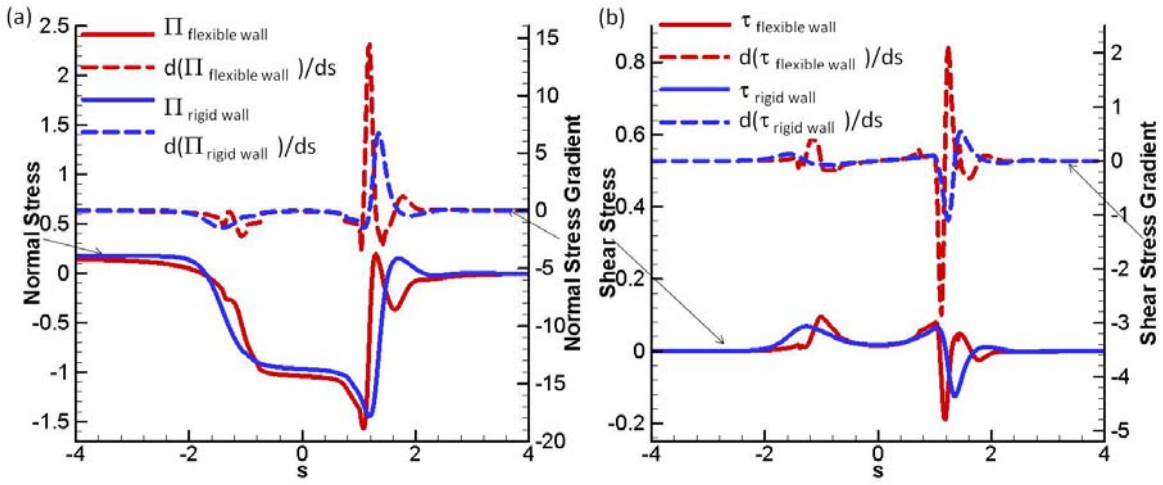

Figure 5.7 (a) The normal stress, normal stress gradient and (b) shear stress, shear stress gradient along the wall arc length s (s=0 corresponds to x=0) at Ca=0.01, LP=1 and Re=0 on the flexible wall and rigid wall. Red colored curves represent those on the bottom flexible wall, while blue curve represents those on a rigid wall.

Fig. 5.7b shows the wall shear stress τ_w (solid lines) and its gradient $d(\tau_w)/ds$ (dash lines) along the wall surface with arc length *s* on the flexible wall and rigid wall when plug propagates through a 2-D channel at Ca=0.01, LP=1 and Re=0. In the plug core region, the wall shear stress is shown to be the similar for both flexible and rigid wall. In both front and rear transition regions, the locations of the peak magnitudes shift towards the center when wall is flexible, and the peak magnitude increases. As shown in Fig. 5.7b, near the rear transition region, the local peak of τ_w is 0.095 at x=-1 on the flexible wall but τ_w =0.068 at x=-1.255 on the rigid wall. In the front transition region, the peak magnitude of τ_w is 0.189 at x=1.19 on the flexible wall. On the rigid wall, the

wall shear stress peak τ_w =0.125 occurs at x=1.36. The flexible wall shear stress shows higher peak value and the peak position shifts towards the center x=0 compared to the rigid wall. The shear stress gradients are a lot larger in the transition regions on the flexible wall than on the rigid wall as well. $d(\tau_w)/ds$ is shown to has a negative peak around -2.85 at x=0.115 and a positive peak around 2.12 at x=1.242 on the flexible wall. While on the rigid wall, the peak magnitude is only around 1.1, which is even less than half of that on the flexible wall. The high peak values and their rapid changes may result in a higher risk of cell damages on the flexible wall than the rigid one. At far end films, the wall shear stress is 0 since the flow is nearly uniform in the film region.

5.7 Discussion

Our computation shows agreements with the experiments on the wall deformation. As the plug propagates through the flexible channel, the negative pressure generated on the wall near the plug core is large enough to deform the flexible wall, which affects the plug flow and wall stresses. The dimensional values of the wall maximal deformation and stress can be estimated from our computation. For LP=1, Ca=0.01 and Re=0, the maximal wall deformation is 0.165, and peak magnitudes of the normal stress and shear stress are -1.5 and -0.19 with the scales of σ/H. The dimensional normal and shear stress peaks are $1.5\text{x}10^4$ and $0.19\text{x}10^4$dyne/cm^2 and the wall maximal deformation is ~8μm. This is close to our experimental measurements of 12.5±2 μm for the maximum deformation and estimation of $1.05 \text{ x } 10^3$Pa for the transmural pressure. This set up can be then used to mimic the actual flexible airways and study the cell injury from plug propagation with the effect of wall flexibility. It should be noted, that the experiments and computation did not take into account many factors such as pulmonary surfactant and stresses from wall stretching during the deformation. The analysis here would limit to the airway system with surfactant dysfunction and the stresses estimated are mainly from the fluid with stresses from wall stretching neglected.

It is commonly known that increasing compliance in the lungs or airway trees helps breathing and relieve the lung injuries. However, the opposite trend is shown locally in current scenario. When the plug forms and blocks the lung airways, the wall flexibility may result in larger injuries due to the larger wall stress imposed. The compliance may help recruiting more alveoli; at the same time, it may worsen the local

cell or tissue injuries due to the increased wall stresses. Normal surfactant function is expected to reduce the surface tension and the peaks of the wall pressure and shear stress, which reduces the potential damages of the epithelial cells lining on the flexible walls.

Airway reopening on the epithelial cells has been studied previously by [18, 20, 21], where the lung epithelial cells were exposed to the propagating semi-infinite bubbles [14, 18, 20] or plugs [21] through rigid channels and severe cell injuries were demonstrated under the fluid stresses during airway reopening. This microfluidic flexible airway system enables us to demonstrate the importance of the wall flexibility in promoting the mechanical tissue injury during airway reopening. This has not been addressed in previous models. Our studies provide new insights into understanding physiological nature of flexible airways on the local cell injuries during airway reopening in many diseases and clinical therapies.

5.8 Conclusions

In this chapter, a microfluidic airway system was used to study the effect of wall flexibility on the plug propagation experimentally and computationally. Flexible microchannels were fabricated with compliance similar to that of the human small airways by incorporating a thin membrane as one channel wall. The local deformation of this thin flexible wall is observed experimentally as the plug propagates through the microchannel. The numerical results agree with the experiments on the wall deformation and predict a higher level of wall stress and stress gradients along the flexible wall comparing to a rigid channel wall. Therefore more deleterious effects are expected on the cells lining in the flexible airways during the reopening plug flows. Current approaches provide a stage to enhance the understanding of pulmonary mechanical forces during the airway reopening process. The results potentially contribute to relieving the lung injuries during the lung diseases and treatments. Future studies will be performed on the responses of cells cultured on the flexible wall during the plug propagations and ruptures.

References

1. Hogg, J.C., et al., *The nature of small-airway obstruction in chronic obstructive pulmonary disease.* New England Journal of Medicine, 2004. **350**(26): p. 2645-2653.
2. Baker, C.S., T.W. Evans, and B.J. Randle, *Damage to surfactant-specific protein in acute respiratory distress syndrome.* Lancet, 1999. **353**(9160): p. 1232-1237.
3. Holm, B.A. and S. Matalon, *Role of pulmonary surfactant in the development and treatment of adult respiratory distress syndrome.* Anesthesia & Analgesia, 1989. **69**(6): p. 805-18.
4. Griese, M., *Pulmonary surfactant in health and human lung diseases: state of the art.* European Respiratory Journal, 1999. **13**(6): p. 1455-1576.
5. Hohlfeld, J., H. Fabel, and H. Hamm, *The role of pulmonary surfactant in obstructive airways disease.* Europ. Resp. J., 1997. **10**(2): p. 482-491.
6. Wright, S.M., et al., *Altered airway surfactant phospholipid composition and reduced lung function in asthma.* Journal of Applied Physiology, 2000. **89**(4): p. 1283-1292.
7. Griese, M., P. Birrer, and A. Demirsoy, *Pulmonary surfactant in cystic fibrosis.* European Respiratory Journal, 1997. **10**(9): p. 1983-1988.
8. Griese, M., et al., *Pulmonary surfactant, lung function, and endobronchial inflammation in cystic fibrosis.* American Journal of Respiratory & Critical Care Medicine, 2004. **170**(9): p. 1000-1005.
9. Grotberg, J.B., *Respiratory fluid mechanics and transport processes.* Annual Review of Biomedical Engineering, 2001. **3**: p. 421-457.
10. Fujioka, H. and J.B. Grotberg, *Steady Propagation of a Liquid Plug In a 2-dimensional Channel.* J. Biomech. Eng. Transaction of ASME, 2004. **126**(5): p. 567-577.
11. Gaver, D.P., et al., *The steady motion of a semi-infinite bubble through a flexible-walled channel.* Journal of Fluid Mechanics, 1996. **319**: p. 25-65.
12. Halpern, D., et al., *Unsteady bubble propagation in a flexible channel: predictions of a viscous stick-slip instability.* Journal of Fluid Mechanics, 2005. **528**: p. 53-86.
13. Heil, M., *Finite Reynolds number effects in the Bretherton problem.* Physics of Fluids, 2001. **13**(9): p. 2517-2521.
14. Jacob, A.M. and D.P. Gaver, *An investigation of the influence of cell topography on epithelial mechanical stresses during pulmonary airway reopening.* Physics of Fluids, 2005. **17**(3).
15. Jensen, O.E., et al., *The steady propagation of a bubble in a flexible-walled channel: Asymptotic and computational models.* Physics of Fluids, 2002. **14**(2): p. 443-457.
16. Muscedere, J.G., et al., *Tidal ventilation at low airway pressures can augment lung injury.* American Journal of Respiratory & Critical Care Medicine, 1994. **149**(5): p. 1327-1334.
17. Taskar, V., et al., *Surfactant dysfunction makes lungs vulnerable to repetitive collapse and reexpansion.* American Journal of Respiratory & Critical Care Medicine, 1997. **155**(1): p. 313-320.

18. Bilek, A.M., K.C. Dee, and D.P. Gaver, *Mechanisms of surface-tension-induced epithelial cell damage in a model of pulmonary airway reopening.* Journal of Applied Physiology, 2003. **94**(2): p. 770-783.
19. Gaver, D.P., et al., *Ventilator-Induced Lung Injury.* eds Dreyfuss D, Sanmon G, Hubmayr RD (Taylor & Francis, New York), 2006: p. 157-203.
20. Kay, S.S., et al., *Pressure gradient, not exposure duration, determines the extent of epithelial cell damage in a model of pulmonary airway reopening.* Journal of Applied Physiology, 2004. **97**(1): p. 269-276.
21. Huh, D., et al., *Acoustically detectable cellular-level lung injury induced by fluid mechanical stresses in microfluidic airway systems.* Proceedings of the National Academy of Sciences of the United States of America, 2007. **104**(48): p. 18886-18891.
22. Duffy, D.C., et al., *Rapid prototyping of microfluidic systems in poly(dimethylsiloxane).* Analytical Chemistry, 1998. **70**(23): p. 4974-4984.
23. Kamm, R.D., *Airway wall mechanics.* Annual Review of Biomedical Engineering, 1999. **1**: p. 47-72.
24. Lotters, J.C., et al., *Polydimethylsiloxane as an elastic material applied in a capacitive accelerometer.* Journal of Micromechanics and Microengineering, 1996. **6**(1): p. 52-54.
25. Lotters, J.C., et al., *Polydimethylsiloxane, a photocurable rubberelastic polymer used as spring material in micromechanical sensors.* Microsystem Technologies, 1997. **3**(2): p. 64-67.
26. Lotters, J.C., et al., *The mechanical properties of the rubber elastic polymer polydimethylsiloxane for sensor applications.* Journal of Micromechanics and Microengineering, 1997. **7**(3): p. 145-147.
27. Silver, F.H., J.W. Freeman, and G.P. Seehra, *Collagen self-assembly and the development of tendon mechanical properties.* Journal of Biomechanics, 2003. **36**(10): p. 1529-1553.
28. Cavalcante, F.S.A., et al., *Mechanical interactions between collagen and proteoglycans: implications for the stability of lung tissue.* Journal of Applied Physiology, 2005. **98**(2): p. 672-679.
29. Imrak, C.E. and I. Gerdemeli, *The problem of isotropic rectangular plate with four clamped edges.* Sadhana-Academy Proceedings in Engineering Sciences, 2007. **32**(3): p. 181-186.
30. Levy, S., *Bending of rectangular plates with large deflections.* T.N. No. 737, National Advisory Committee for Aeronautics, Washington, D.C., 1942a.
31. Timoshenko, S. and S. Woinowsky-krieger, *Large deflections of plates.* Theory of plates and shells. 1959: McGraw-Hill, Tokyo.
32. Wang, C.T., *Nonlinear large-deflection boundary-value problems of rectangular plates.* T.N. No. 1425, National Advisory Committee for Aeronautics, Washington, D.C., 1948.
33. Wang, D.F. and A.I. El-Sheikh, *Large-deflection mathematical analysis of rectangular plates.* Journal of Engineering Mechanics-Asce, 2005. **131**(8): p. 809-821.
34. Thompson, J.F., B.K. Soni, and N.P. Weatherill, *Handbook of Grid Generation.* 1999: CRC Press.

35. Patankar, S.V., *Numerical Heat Transfer and Fluid Flow*. 1980, London: Hemisphere.
36. Press, W.H., et al, *Numerical Recipes in C. 2 ed.* Cambridge University Press, 1992.
37. Howell, P.D., S.L. Waters, and J.B. Grotberg, *The propagation of a liquid bolus along a liquid-lined flexible tube.* Journal of Fluid Mechanics, 2000. **406**: p. 309-335.

CHAPTER 6

CONCLUSIONS

This thesis investigates the transport of liquid plugs through the pulmonary airways in order to understand the fundamental fluid mechanics in many lung diseases and clinical therapies, and to optimize the treatment efficiencies. Analytical, experimental an computational methods are applied to study the fluid mechanics of the following phenomena: liquid delivery into the lung, mucus clearance from the lung, and microfluidic study of the liquid plug propagations in flexible channels.

Many clinical therapies require liquid instillation into the lungs such as surfactant replacement therapy (SRT), liquid ventilation and drug delivery. Studies have shown that the effectiveness of the treatments by liquid delivery may depend on how liquids distribute in the lung. In clinics, physicians tend to turn the patients in different orientations during liquid delivery. Many studies have investigated the plug or semi-infinite bubble propagations in straight channels, but very few studied the liquid distribution from plug propagation and splitting in the lungs. The lungs is composed of branching airways trees, thus understanding liquid delivery through straight tubes and bifurcations will be of great benefit on the liquid transport and lung functions.

The first part of this dissertation studies the fundamental fluid mechanics of the liquid plug propagation through the tubes and bifurcating airway models in order to reveal important system parameters governing the liquid delivery and distribution. When a liquid plug propagates in the straight tube before it reaches the bifurcation, the plug volume shows asymmetry due to the gravity, which predetermines the asymmetric splitting: more liquid enters the gravity-favored branches. This pre-bifurcation symmetry is then studied using computational fluid mechanics method. The effects of gravity (characterized as the Bond number Bo), gravitational orientation α, the plug speed (Ca at

Stokes flow regime, or Re with high inertia), plug volume and the presence of surfactant are assessed on the plug propagation in a two-dimensional channel. When there is no gravity (Bo=0), the flow inside the plug is symmetric and independent on the upper and lower half domains of the plug. When Bo>0 and $\alpha \neq 0$ or π, the fluid is found to flow from the upper precursor films, pass through the plug cores, and finally enter the lower trailing films. The flow recirculations become weaker with the increase of Bo and the resulting number of vortices can be 0, 1 and 2 depending on the flow parameters. When the surfactant is present, the vortices detach from the interfaces and lead to two saddle points inside the plug core. Capillary waves develop in the front transition regions with the amplitude increases with Bo and Re, which results in an increasing magnitude of wall pressure and wall shear stress. Consequently, a higher risk of pulmonary epithelial cell damage occurs on the top wall. The pre-bifurcation asymmetry is quantified by the volume ratio. The results show that the asymmetry is enhanced by increasing Bo but reduced by increasing the plug volume, speed and surfactant. The fluid mass deposited in the trailing films increases with increasing Bo for $\alpha > 2\pi/5$, gravity orientation α, plug length L_P and plug speed. At the same time, it increases with C_0 for small Bo (Bo<0.4) while decreases with C_0 as Bo≥0.4.

The plug splitting behavior is studied experimentally using a bench-top symmetric bifurcation. Liquid plugs are instilled into the parent tube of the bifurcations with a constant flow rate driven by a syringe pump. The effects of gravity and flow rate are studied by varying the roll angle, pitch angles, and different flow speed. The plug splitting behavior is recorded and analyzed, from which the splitting ratio is calculated by dividing the length of the plugs entering the daughter branches. The results show that the splitting ratio increases with increasing flow rate, decreasing Bo and the gravitational orientations (roll and pitch angles). A critical plug speed is found below which the plug did not split and traveled entirely into the lower branch by gravity. The plug splitting behavior is studied in both low Re regime and high Re regime with three different plug materials. The results show that inertia plays a very important role in plug splitting: more homogeneous plug splitting with inertia and larger effects on shorter plug. Downstream plug blockages are introduced to simulate the effect of earlier delivery of liquid during the treatments. The lower daughter blockage counteracts the effect of gravity and results

in a larger splitting ratio, while the upper blockages have the opposite effects. The liquid distribution is more homogeneous with larger volume, faster speed and lower gravitational effects.

These results observed in both experiments and in the theoretical work, can be incorporated into clinical therapies to achieve relatively homogeneous liquid distributions in the lungs. The results suggest that faster flow rate allows the plugs to move more uniformly through the airway trees. The patients may be positioned in specific orientations in order to achieve the liquid delivery to specific target regions. Multiple doses are better for the homogeneous liquid distribution.

In diseases like asthma and chronic bronchitis, mucus plugging may easily form in the pulmonary airways, and block the breathing pathways, threatening the patients' lives. Removing mucus, which has non-Newtonian properties, from the lung is very essential to reduce the life threaten.

The second part of this dissertation computationally studies the mucus plug propagation and clearance from the pulmonary airways. The mucus plug propagation is studied with various shear thinning effects as well as the plug propagation speed and presence of surfactant. The power law model is used for the shear thinning properties of the mucus. It is found that the mucus have a higher shear-thinning effects with decreasing the power law component n, which causes the effective viscosity and shear stress to increase. Thus the trailing film thickness and pressure drop increases. The recirculations in the plug core become smaller and weaker with the decrease of n due to the increased viscosity in the plug core center. Larger driving force is required to drive the mucus plugs due to the increased shear stress when n decreases. As the surfactant is present, even larger pressure drop over the plug is needed for the mucus plug to propagate though the viscosity in the plug tends to decrease. A higher surfactant concentration is achieved along the plug menisci with decreasing n, which causes a higher Marangoni stresses for both front and rear transition region. A shorter but thicker film in the front transition region is found for smaller n, which compresses and amplifies the pressure and shear stress gradients. The presence of surfactant is found to decrease the viscosity of the plug core, thus soften the mucus plug and help the mucus removal from the lung.

Previous studies have reported severe damages on the cell lining on the rigid channel walls during plug propagation. However, no experimental studies have been performed on the plug propagation and induced stresses on the flexible walls, which is happening in the real airways. Very few theoretical or computational studies were performed to predict this behavior either. Therefore, the third part of this dissertation studies the plug propagation in a microfluidic flexible channel with both experiments and computations, mimicking a small airway model. A thin membrane is incorporated into the microchannel to model the physiologic thin airway wall. Pairs of bubbles were injected into the square cross sectional areas to investigate the wall flexibility on plug propagations through a microchannel. The wall deformation is observed from the high negative pressure when plug propagates, causing the plug to become asymmetric. Computations agree with the experiments. Higher stress and stress gradients are predicted on the flexible wall than on the rigid channel wall. More deleterious effects on the lining cells are expected during the reopening plug flows on the flexible airways. This study enhances the current understanding of pulmonary mechanical forces during the airway reopening process in more physiological situations. It potentially contributes to relieving the lung injuries during the lung diseases and treatments.

In a summary, this dissertation describes in depth the fundamental fluid mechanics and transport for physiological situations in the lungs during liquid delivery, mucus clearance and airway reopening in flexible small airways with microfluidic approaches. Fluid mechanics as well as the physiological applications are studied in details for the liquid plug propagation and splitting behavior. The work presented here provides new information for the physical mechanisms on the liquid plug dynamics in pulmonary airways during liquid instillation, removal and airway reopening in micro scales. Further investigation in both experiments and computations can be used to simulate the specific in-vivo situations.